

Structure-Function Relationships of Self-Assembled Fibrillar Gels

Kathleen M. Weigandt

A dissertation

submitted in partial fulfillment of the
requirement for the degree of

Doctor of Philosophy

University of Washington

2012

Reading Committee:

Danilo C. Pozzo, Chair

Daniel T. Schwartz

Nathan J. White

Program Authorized to Offer Degree:

Chemical Engineering

University of Washington

Abstract

Structure-Function Relationships of Self-Assembled Fibrillar Gels

Kathleen M. Weigandt

Chair of the Supervisory Committee:
Assistant Professor Danilo C. Pozzo

Department of Chemical Engineering

Fibrillar gels represent an important class of materials with commercially relevant applications in the cosmetics and pharmaceutical industries and biological significance as the underlying structural component in many soft tissues. In this work we study two distinct fibrillar gels that are different in terms of constituent molecules, solvent, gelation mechanism and mechanical properties. Fibrin is a naturally occurring protein that forms covalently crosslinked hydrogels and is responsible for the strain hardening of blood clots. In contrast, P3HT is a synthetic conjugated polymer that forms a thermoreversible physical gel in organic solvents and is utilized as an active component in organic solar cells. A combination of small angle scattering techniques is used to characterize the morphology of these gels, both the individual fibers and the network structure, over large length scales between 1 nm and 10 μm . Furthermore, the combined rheological and structural characterization of these gels is used to develop relationships between the structural and mechanical properties of these systems. In fibrin gels the structural origin of strain hardening is investigated by directly probing the structure of hydrated gels as they are strained. Additionally, rheoSANS measurements have been utilized to investigate the gelation and dissolution of P3HT gels. By exploring systems with very different mechanical and physical properties we have developed a framework for analysis that can be applied to a variety of fibrillar systems.

TABLE OF CONTENTS

List of Figures	iii
List of Tables	vi
Chapter 1 Mechanical and Structural Properties of Gels.....	1
Introduction.....	1
Gel Rheology	5
Highlights and Objectives.....	9
References.....	13
Chapter 2 Experimental Methods: Small Angle Scattering.....	15
Small Angle Scattering Theory.....	16
General Experimental Methodology.....	20
Data Analysis	30
Summary.....	45
References.....	46
Chapter 3 Fundamental Characterization of Fibrin Structure and Rheology	47
Introduction.....	47
Materials and Methods.....	52
Results.....	54
Discussion.....	65
References.....	72
Chapter 4 <i>In-Situ</i> Neutron Scattering Study of Structural Transitions in Fibrin Networks under Shear Deformation.....	74
Introduction.....	74
Materials and Methods.....	78
Results.....	80
Discussion.....	90
References.....	95
Chapter 5 Alterations in Fibrin Clot Structure and Mechanics Attributed to Specific Oxidation of Methionine Residues in Fibrinogen.....	97
Introduction.....	97
Materials and Methods.....	99
Results.....	104

Discussion	119
References	121
Chapter 6 Structure and Rheology of P3HT Gels	123
Introduction	123
Materials and Methods	129
Results	132
Discussion	146
References	147
Chapter 7 RheoSANS Investigation of the Structural and Mechanical Evolution of P3HT during Gelation and Dissolution	150
Introduction	150
Materials and Method	153
Results	156
Discussion	172
References	174
Chapter 8 Conclusion and Outlook	176
Bibliography	183
Appendix 1 Useful Tables for Scattering Experiments and Analysis	195
Appendix 2 Fibrin Sample Preparation Protocols	197

LIST OF FIGURES

Figure 1.1: Electron Microscopy Images of Fibrin and P3HT.	2
Figure 1.2: Schematic Defining Rheology Parameters.....	6
Figure 1.3: Small Amplitude Oscillatory Rheology	7
Figure 1.4: Linear Viscoelastic Limit.	8
Figure 2.1: X-ray and Neutron Scattering Schematic.....	17
Figure 2.2: SANS Instrument Schematic.....	21
Figure 2.3: USANS and Slit Smearing Schematics.....	22
Figure 2.4: Schematic of rheoSANS apparatus. Figure not to scale.....	26
Figure 2.5: Illustration of scattering planes accessible with shear scattering techniques.	27
Figure 2.6: Schematic of 1-2 shear cell SANS instrumentation. Figure not to scale.	28
Figure 2.7: Schematic of conductivity-SANS experimental set up. Figure not to scale. .	30
Figure 2.8: Example Scattering from a Dispersion of Nanorods.....	32
Figure 2.9: Example Guinier Analysis for a Dispersion of Nanorods.....	34
Figure 2.10: Example Porod Plot for a Dispersion of Nanorods	36
Figure 2.11: Parallelepiped and Excluded Volume Polymer Form Factor.....	43
Figure 2.12: Schematic Defining Orientation in the 2D Cylinder Form Factor.	45
Figure 3.1: Fibrin Structural Features	50
Figure 3.2: Linear Rheology of Fibrin Clots.	55
Figure 3.3: Instantaneous Modulus of Fibrin Gels.	56
Figure 3.4: Reduced Fibrin SANS and USANS Data.....	58
Figure 3.5: Protein Fraction in Fibrin Fibers	60
Figure 3.6: Radius of Fibrin Fibers.....	61
Figure 3.7: Average Number of Protofibrils in the Fiber Cross Section	62
Figure 3.8: Fractal Dimension Correlation Length (L_c) [\circ] of Fibrin Gels.....	63
Figure 3.9: Optical Microscopy of a 1 mg/mL Fibrin Gel.....	64
Figure 3.10: Increasing Fibrillar Protein Concentration Schematic	70

Figure 4.1: Strained Fibrin Gel Reduced 2D SANS Data.	81
Figure 4.2: Determination of Fiber Orientation Distribution.....	82
Figure 4.3: 2D Fit of Aligned Fibrin SANS Data.	85
Figure 4.4: Structural and Mechanical Properties of a Strained Fibrin Gel.....	87
Figure 4.5: Irreversible Deformation of Fibrin Gels.....	88
Figure 4.6: Schematic Description of Fibrin Deformation.	91
Figure 5.1: HOCl Oxidized Fibrinogen Schematic.....	105
Figure 5.2: Circular Dichroism from Oxidized Fibrinogen.	106
Figure 5.3: UV-Vis Spectroscopy of Oxidized Fibrin Gels.....	107
Figure 5.4: Oxidized Fibrinogen SEM.....	109
Figure 5.5: Oxidized Fibrinogen SAXS.....	110
Figure 5.6: Linear Rheology of Oxidized Fibrin	113
Figure 5.7: Concentration Dependent Elastic Modulii in Oxidized Fibrin Gels.	113
Figure 5.8: Instantaneous modulus of Oxidized Fibrin Gels	115
Figure 5.9: Fibrinolysis induced by tPA and Plasminogen.	119
Figure 6.1: Schematic of OPV Heterojunctions.	124
Figure 6.2: Photographs of Solubilized and Gelled P3HT and Schematic of Fiber	125
Figure 6.3: P3HT Images: Soluble, Gel, and Gel Dispersion.....	127
Figure 6.4: Schematic of Evaporation Blockers.	132
Figure 6.5: Rheology: Gelation of P3HT.....	134
Figure 6.6: Modulii as a Function of Frequency for P3HT Gels.....	135
Figure 6.7: Rheology of P3HT Gels in Aromatic Solvents	136
Figure 6.8: P3HT Gelation Kinetics.	138
Figure 6.9: sSTEM of 30 mg/mL P3HT Gel in Toluene	139
Figure 6.10: 30 mg/mL P3HT Gel SANS and USANS Data	141
Figure 6.11: Fitting Results for P3HT SANS Data.	144
Figure 6.12: Soluble to Fiber P3HT Conversion.	144

Figure 6.13: Fractal Dimension from P3HT Gels.....	146
Figure 7.1: Gelation and Dissolution of P3HT Gels in RheoSANS Experiment.	157
Figure 7.2: 30 mg/mL P3HT rheoSANS Data during Gelation.....	159
Figure 7.3: 30 mg/mL P3HT rheoSANS Data during Dissolution.....	160
Figure 7.4: Selected SANS Files Fit with Combined Form Factor.	164
Figure 7.5: P3HT Fiber Structural Parameters from Form Factor Fits.....	166
Figure 7.6: Fiber Scattering and Porod Plot for Specific Surface Area Analysis.....	168
Figure 7.7: Specific Surface Area as a Function of Temperature.....	168
Figure 7.8: P3HT Rheology and Fiber Fraction During Gelation and Dissolution.....	169
Figure 7.9: Early Dissolution for P3HT Gels in Aromatic Solvents.	171
Figure 7.10: Schematic of P3HT Gelation Mechanism.	173

LIST OF TABLES

Table 5.1: Oxidized methionine residues by HOCl	104
Table 6.1: Molecular weight averages for P3HT-L2 batch polymer	145
Table 7.1: Rheology parameters from rheoSANS experiment.	158
Table A1.1 Neutron scattering lengths and cross sections table.....	195
Table A1. 2: Mass density and scattering length density table.....	196

Acknowledgements

I appreciate the advice and encouragement of my advisor, Prof. Danilo Pozzo. His insight, enthusiasm and mentoring have been invaluable. Thank you to my committee members: Prof. John Berg, Prof. Dan Schwartz, Prof. Paul Yager, and Dr. Nathan White for your advice and experience. Thanks are also owed to my groupmates with whom many ideas were borne out of frantic brainstorming sessions. I would specifically like to thank Greg Newbloom for ongoing collaboration on the P3HT organogel work, Jeff Richards as a collaborator on P3HT emulsions work, Kjersta Larson-Smith for joining me in “hot science” days and editing this dissertation, Monica Ospinal-Jimenez for genuine friendship and comic relief, and Pablo de la Iglesia who drives slower than my grandmother even on a scattering trip. I also appreciate the efforts of my many undergraduate research students including Anya Yermakova, Isabel Gunarto and Erica Ellingson.

Thanks are owed to Lionel Porcar for ongoing collaboration on the fibrin small angle scattering research. Thank you also to my collaborators on the oxidized fibrinogen work including Nathan White, Dominic Chung, Yi Wang and Xiaoyun Fu. I also appreciate the helpful conversations and assistance of the instrument scientists at the NIST center for neutron research. I am especially grateful to Jae-Hie Cho for developing the DANSE SansView code for the combined model and Paul Butler for general assistance and helpful conversations related to neutron scattering experiments.

Dedication

To my parents: Cindy and Dale Weigandt.

Chapter 1 Mechanical and Structural Properties of Gels

Introduction

Developing relationships between the mechanical and structural properties of gels is integral for understanding gelatinous biological systems as well as for engineering commercially relevant gel-based products. At the most basic level, a gel is a material that exhibits solid like properties despite being composed primarily of liquid. Solid-like, or elastic, material properties arise from a bicontinuous solid phase network that spans the entire volume of the gel and acts as a scaffold for the surrounding liquid. This network can develop from a wide range of materials including proteins, polymers, small molecules and solid particles of various shapes and sizes.¹⁻⁵ Electron microscopy images of two dried gels, one formed from the protein fibrinogen and a second formed from the conjugated polymer poly(3-hexylthiophene) (P3HT), are found in Figure 1.1. In each of

these cases, the solid phase comprises only a small percentage of the native gel volume at 0.1 w/v% and ~3 vol% respectively, yet the gels are highly elastic.

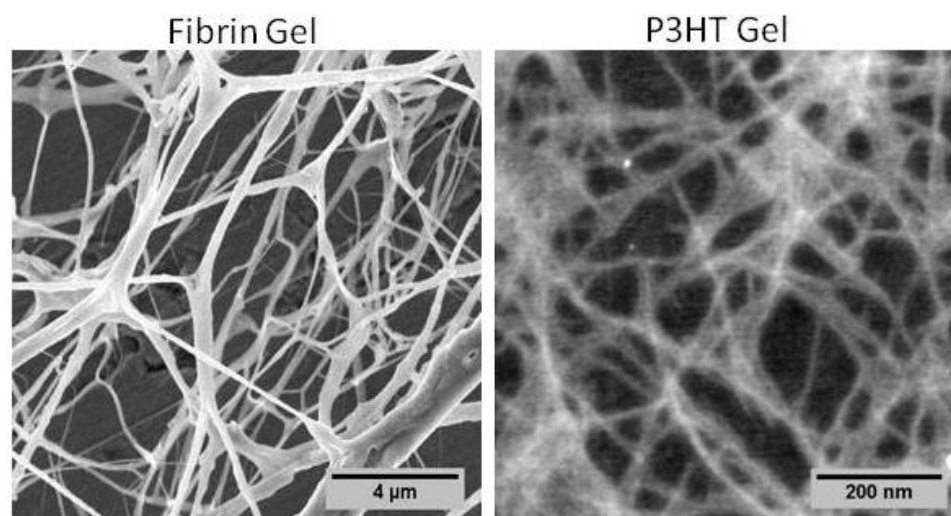


Figure 1.1: Left: Electron microscopy image of a dried 1 mg/mL fibrin hydrogel. Right: sTEM image of a 30 mg/mL P3HT organogel dried from toluene.

The mechanical properties of gelatinous systems are affected by the hierarchical structure of the networks, the mechanical properties of the constituent materials and the interactions that bind these materials together. In fact, gels are often categorized by the nature of the molecular interactions that govern self-assembly and lead to percolation.⁶⁻⁸ The term “chemical gelation” describes the development of permanent networks through the formation of covalent bonds between the individual components of the gel. Chemical gelation is commonly observed in polymer gels, where gelation can be induced during polymerization or by adding a cross-linking agent to pre-existing polymers in solution.^{7,9}

The second broad gelation category is “physical gelation”. In a physical gelation process no permanent chemical bonds are formed. Rather, gelation is driven by weak interactions such as van der Waal’s forces, hydrogen bonding, π - π stacking or hydrophobicity.^{1,7} For protein gels, hydrophobic interactions are particularly relevant. In these gels self-assembly is often driven by the exposure of hydrophobic residues that may

be shielded in the protein's native state are exposed as a response to external stimuli.¹⁰ In another example, π - π stacking leads to fiber formation in small molecule aromatic dyes.¹¹ Physical gels are frequently thermoreversible as the energy barriers required to break the weak physical interactions can be overcome with moderate increases in temperature.^{5, 6, 12, 13}

Some gels do not fit neatly into either category and can be described as combination physical-chemical gels. In particular, fibrin gelation is driven via purely physical mechanisms upon exposure of specific polypeptides in the central domain of the protein.¹⁴ Simultaneous with gelation, the coagulation factor XIIIa covalently ligates adjacent fibrin molecules through the formation of N- ϵ -(γ -glutamyl)lysine isopeptide bonds. The formation of these bonds is not necessary for fibrin gel formation; however, covalent ligation supports enhanced mechanical properties and is physiologically necessary to maintain blood clot stability.

Regardless of the specific gel system or application, understanding and manipulating the mechanical properties of protein gels is of great interest. In food chemistry, establishing relationships between composition and mechanical properties is instrumental in the manipulation of food texture, mouth-feel and consistency.⁸ Similarly, small molecule organogelators are frequently used to gel cosmetically relevant ingredients in order to produce common products such as chapstick.¹⁵ In the medical field, evaluating the mechanical properties of physiological protein gels is a powerful assay for the evaluation of diseases that affect protein gelation and could also aid in the design of hydrogels for tissue scaffolding and surgical glues.^{16, 17} In short, gels are a broad class of

materials with wide ranging properties and are important for various medical and commercial applications.

In this research, we focus on a narrow subclass of gels where the solvent is supported by self-assembled bifurcating fibrillar networks. The fundamental building blocks in fibrillar gels are very diverse. Here, two distinct systems are studied: poly(3-hexylthiophene) (P3HT) organogels and fibrin hydrogels. These systems are different in terms of constituent molecule, solvent type, and gelation mechanism, but they can each form fibrillar gels. The primary objective of this work is to develop relationships between the structural and mechanical properties of these gels.

Fibrin is a naturally occurring protein that forms covalently crosslinked hydrogels via a physical gelation mechanism. Fibrin is the primary structural and mechanical component of blood clots, so understanding the formation and mechanical properties of fibrin gels is extremely important in the medical field. Gelation of fibrin gels is initiated when fibrinopeptides A and B are removed from inactive fibrinogen with activated thrombin.¹⁴ In these gels, the fiber size is dictated by the local solvent composition, protein concentration, and protein heterogeneity.¹⁸⁻²⁰

In contrast, P3HT is a synthetic conjugated polymer that forms a thermoreversible physical gel in organic solvents. P3HT is a commonly used semiconductor in organic electronic devices. We have hypothesized that gelation of P3HT may lead to better devices due to the interconnectivity of the fiber network. P3HT fiber network formation is initiated by altering the solvent to reduce the polymer solubility either through the addition of a second poor solvent or, as in this study, by reducing the solution temperature.^{5, 21} The P3HT molecules self assemble into semi-crystalline P3HT fibers

with π - π stacking thru the long fiber axis. Despite the differences between P3HT and fibrin gels, the underlying fibrillar structure is strikingly similar as illustrated in Figure 1.1.

Though P3HT and fibrin gels are both composed of bifurcating fibrillar networks, the mechanical properties of these materials are extremely different. Fibrin gels, like other biological polymers, have highly non-linear mechanical properties that are critical for physiological function.²² Fibrin gels are highly extensible and stiffen as they are deformed.²³ On the other hand, P3HT gels are relatively weak and yield under very low stresses. P3HT gels are also thermoreversible with significant hysteresis between heating and cooling ramps. To better understand the structural origin of the mechanical properties observed in these systems, small angle scattering and complementary electron microscopy techniques are used to fully characterize the structural properties of these gels. The theory behind small angle scattering and methods for data analysis are discussed in Chapter 2 of this dissertation. The mechanical properties of these gels are measured with shear rheology techniques. The basic theory behind these techniques is described in the following paragraphs.

Gel Rheology

In this study, stress-controlled shear rheometers are used for all rheology measurements. P3HT and fibrin gels were formed *in situ* in one of three basic measurement geometries: the cone and plate, the concentric cylinder, or the parallel plate. Each of these geometries has distinct advantages and disadvantages for specific material systems and measurements. Figure 1.1 illustrates an idealized discrete volume of the gel

bound between the two walls of any of these geometries. The applied shear stress (τ) is equal to F/A where F is the applied shear force and A is the surface area over which the force is applied. The application of shear force will result in some sample deformation or strain. Strain is measured in terms of lateral deformation (Δx) relative to the gap between the two plates (h), such that at 100% strain $\Delta x=h$.

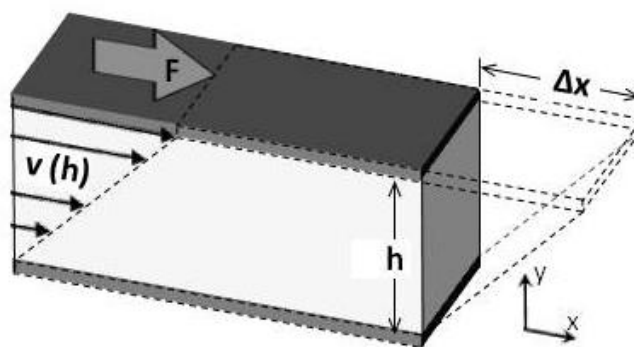


Figure 1.2: Schematic of rheology parameters.

The mechanical properties of a gel are determined from a measurement of the deformation as a function of the applied shear stress. In viscoelastic gels the measured response will reflect both the elasticity of the network and the viscosity of the liquid phase. To measure the equilibrium mechanical properties of a gel, the application of stress must remain non-destructive. Therefore, small amplitude strain oscillations, with strains on the order of 0.01-1%, are typically used to measure the mechanical properties of gels in order to prevent damage to the underlying structure that may occur with larger deformation.

A small amplitude oscillatory strain wave is applied with a constant strain amplitude of γ_0 . The required shear stress to apply the stress wave is measured. These waves will be partially out of phase as illustrated in Figure 1.2. The phase shift reflects the mixed viscous (out of phase) and elastic (in phase) properties of the gel. The elastic

and viscous properties are extracted with Equation 1.1 where the shear stress wave is separated into the sum of the in and out of phase components.

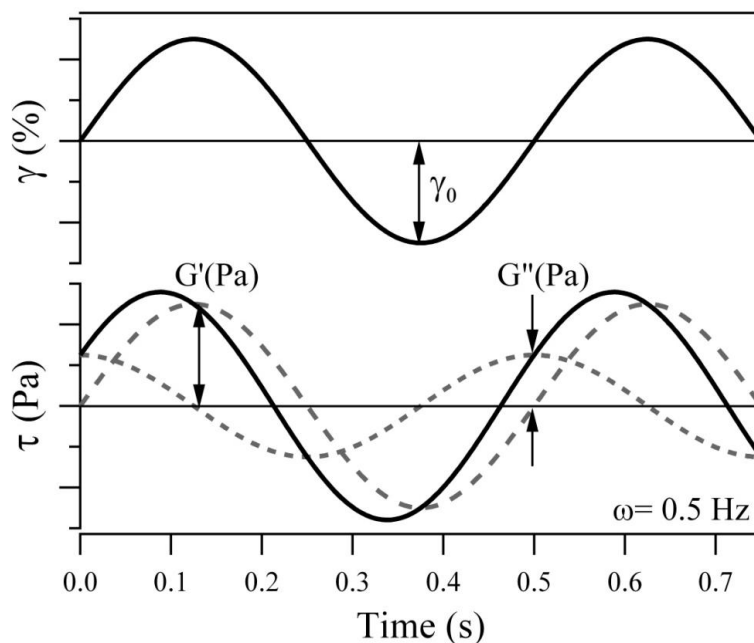


Figure 1.3: Relationship between the applied strain, the stress response and the elastic and viscous moduli in small amplitude shear rheology experiments.

$$\tau(t) = \gamma_0 [G' \sin(\omega t) + G'' \cos(\omega t)] \quad \text{Equation 1.1}$$

In this equation, ω is the angular frequency, t is time, G' is the elastic modulus, and G'' is the viscous modulus. Equation 1.1 is only valid for materials that exhibit linear viscoelasticity. That is, the elastic and viscous moduli must be constant as a function of applied strain. Alternatively, a linear response is characterized by a linear increase in shear stress with respect to the applied strain. Upon reaching some critical strain the gel may weaken or harden with additional deformation. This is termed the linear viscoelastic limit and is illustrated in Figure 1.3. Here a 5 wt% P3HT organogel is probed with oscillatory shear at increasing strain amplitude. At the linear viscoelastic limit, the network begins to break apart and the gel becomes progressively weaker as a function of

increasing strain. In this case, an appropriate strain amplitude for oscillatory shear rheology measurements must be less than 0.5%.

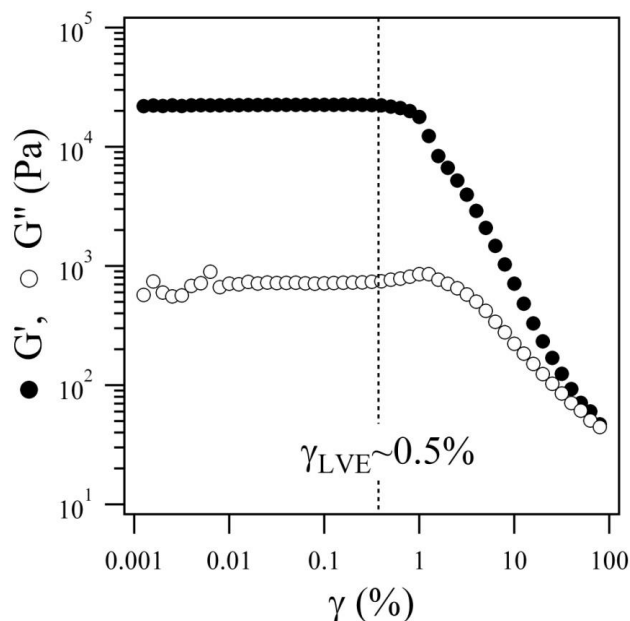


Figure 1.4: Strain dependent viscous and elastic moduli measured from a 5 wt% P3HT gel in xylene.

Strain hardening, another form of non-linear viscoelasticity, is a more unusual property; however, it is relatively common in biopolymer gels.^{22, 24} Gels formed from various proteins including fibrin, actin, collagen and vimentin strain harden at deformations beyond their linear viscoelastic limit. Given that the human body contains nearly 65 wt% water, these protein gels play an important role in forming the structural framework for many tissues, blood clots, and even individual cells. Interestingly, despite the importance of strain-hardening biopolymer gels to human physiology, the exact mechanism for strain hardening in these gels remains an active research area.^{22, 25-28}

Many rheological models exist to relate the time, temperature, concentration, frequency and strain dependent mechanical properties of fibrillar gels to the various structural properties of these materials. Unfortunately it is often very difficult to verify

the validity of these models, as most methods of structural characterization require substantial post gelation modification to remove the liquid component for characterization under high vacuum. Furthermore, simultaneous characterization of mechanical and structural properties is rare, especially for systems where the structural components are too small to be visible with optical microscopy. By directly measuring the bulk structural and mechanical properties of these gels, we are able elucidate the origin of strain hardening in fibrin gels and gain a better understanding of disease-induced clotting disorders. Additionally, we can propose a novel mechanism for the thermoreversible gelation of P3HT.

Highlights and Objectives

In Chapter 2 a brief introduction to the theory of small angle scattering is presented. Here, the focus is on presenting theoretical and technical details critical to the understanding of the structural characterization presented in subsequent chapters. A brief description of the experimental set-up for small angle and ultra small angle neutron scattering is presented. Additional detail and descriptions of three combined techniques have been included. These techniques include rheoSANS, 1-2 plane shear SANS, and conductivity SANS. RheoSANS facilitates the direct, simultaneous measurement of the rheological and structural properties of gels or other complex fluids. Similar to rheoSANS, 1-2 plane shear SANS facilitates the characterization of complex fluids and gels under applied shear stresses, however in this case mechanical measurements are not taken simultaneously. The conductivity-SANS cell was developed by Newbloom et al. to facilitate the simultaneous measurement of electrical and structural properties in

developing P3HT gels. Finally, a detailed description of all scattering analysis techniques utilized in this dissertation, including Guinier, Porod, and model fitting analyses, is included in the third section of Chapter 2.

In Chapter 3, the structural and mechanical properties of coarse fibrin networks formed in D₂O buffers are investigated over a wide range of concentrations (1-40 mg/mL).²³ Small angle neutron scattering (SANS) and ultra small angle neutron scattering (USANS) are used to seamlessly characterize the structure over length scales ranging from 1 nm to several micrometers. Using invariant and Guinier analyses the internal volume fraction of protein within the fiber and the bulk average fiber radius are determined directly. The network properties of fibrin clots are also characterized using a model for fractal structures. The network scale features are shown to be highly dependent on the initial fibrinogen concentration while the average fiber radius is only weakly dependent on this parameter. These results demonstrate the usefulness of combining SANS and USANS as characterization tools for fibrillar gels. The linear viscoelastic modulus of fibrin gels is related to the concentration by a power law equation that is valid over the entire range. In contrast, the non-linear rheology of dense networks is altered from the monotonic strain hardening response that is found at lower concentrations. The results presented in this chapter motivate the shear-deformation SANS study described in Chapter 4.

In Chapter 4 small angle neutron scattering (SANS) is used to decipher the origin of the strain hardening in biopolymer networks by directly measuring the structural response of a fibrin gel to simple shear deformation.²⁹ A special Couette 1-2 plane shear cell is used to systematically probe the structural properties of a fibrin clot over strain

values in the range of $\gamma=1-170\%$. The SANS results indicate that the strain hardening response in 10 mg/mL coarse fibrin gels occurs in two distinct regions having different structural and mechanical signatures that are separated by an intermediate strain softening regime. At low strains ($\gamma < 10\%$) there is a measurable increase in the shear modulus upon the application of shear strain but there are no significant changes to the clot structure. At higher strain values ($\gamma > 30\%$), a second strain-hardening regime is directly correlated to significant fiber alignment. The mean diameter of the fibers determined directly from two-dimensional fits to the anisotropic scattering data is found to decrease monotonically in the high-strain regime. The results suggest that the non-linear mechanical properties of fibrin clots are the result of a reduction of lateral entropic fluctuations at low strains and a transition between bending and stretching at higher strain values.

In Chapter 5 a combination of structural and mechanical characterization is used to examine the effect of fibrinogen oxidation on the formation of fibrin clots.³⁰ We find that treatment with hypochlorous acid preferentially oxidizes specific methionine residues on the alpha, beta and gamma chains of fibrinogen. Oxidation of these residues is shown to impair lateral aggregation of protofibrils leading to the formation of a dense network of thin fibers. Additionally, both the linear and non-linear mechanical properties of oxidized fibrin gels are found to be altered with oxidation. Finally, the structural modifications induced by oxidation delay fibrin lysis via plasminogen and tissue plasminogen activator (tPA). From these results we propose a specific biophysical mechanism for the inhibition of lateral aggregation of protofibrils in the oxidized fibrin gels.

In Chapters 6 and 7 we shift focus from fibrin to bulk P3HT organogels. In Chapter 6, we investigate the mechanical and structural properties of P3HT gels formed in various organic solvents.³¹ As with the fibrin gels, the bulk structural properties are evaluated using small angle neutron scattering (SANS) and ultra small angle neutron scattering (USANS). Using a combined model that accounts for the soluble and fibrillar polymer, the fraction of crystallized P3HT, the fiber cross section and the specific surface area are determined. The fiber shape is found to be relatively independent of the solvent type; however, the rheological properties vary significantly suggesting that the network branching and fiber distribution may be controllable parameters. The results presented in Chapter 6 suggest that gelation of P3HT may be a feasible approach for designing percolated conductive networks for organic electronic devices.

In Chapter 7 the structure and mechanical properties of P3HT in organic solvents are probed with rheoSANS during the sol-gel transitions induced by temperature cycling.³² Additional conductivity-SANS measurements were performed in collaboration with Newbloom et. al. to simultaneously measure conductivity and structural evolution in a separate series of experiments. The structural features of the gel are shown to evolve throughout the gelation and dissolution processes. From these results we have proposed mechanisms for the thermoreversible gelation and dissolution of P3HT gels. Furthermore, these results highlight the importance of controlling the structure of the evolving P3HT gels in order to engineer semiconducting polymer networks for organic photovoltaics.

The work presented in this dissertation has been previously published in the form of several journal articles. The work presented in Chapters 3 and 4 as well as some excerpts and figures from Chapters 2 and 7 are reproduced from the articles *Soft Matter*,

2009, **5**, 4321-4330, *Soft Matter*, 2011, **7**, 9992-10000, and *Soft Matter*, 2012, **8**, 8854-8864 by permission of The Royal Society of Chemistry. The work presented in Chapter 5 is based on a manuscript that has been submitted for review to the Biophysical Journal entitled: "Alterations in Fibrin Clot Structure and Mechanics Attributed to Specific Oxidation of Methionine Residues in Fibrinogen". Finally, some excerpts and figures have been reproduced in part with permission from *Macromolecules*, 2012, **45**, 3452-3462 Copyright 2012, American Chemical Society.

References

1. P. Terech and R. G. Weiss, *Chem. Rev.*, 1997, **97**, 3133-3159.
2. R. Pelton, *Advances in Colloid and Interface Science*, 2000, **85**, 1-33.
3. L. Spanhel and M. A. Anderson, *Journal of the American Chemical Society*, 1991, **113**, 2826-2833.
4. P. A. Janmey, U. Euteneuer, P. Traub and M. Schliwa, *Journal of Cell Biology*, 1991, **113**, 155-160.
5. S. Malik, T. Jana and A. K. Nandi, *Macromolecules*, 2001, **34**, 275-282.
6. P. J. Flory, *Faraday Discussions of the Chemical Society*, 1974, **57**, 7-18.
7. A. Keller, *Faraday Discussions*, 1995, **101**, 1-49.
8. A. Totosaus, J. G. Montejano, J. A. Salazar and I. Guerrero, *International Journal of Food Science & Technology*, 2002, **37**, 589-601.
9. F. Ikkai and E. Adachi, *Macromolecular Rapid Communications*, 2004, **25**, 1514-1517.
10. A. Immaneni and A. J. McHugh, *Biopolymers*, 1998, **45**, 239-246.
11. T. Ishi-i and S. Shinkai, *Supramolecular Dye Chemistry*, 2005, **258**, 119-160.
12. S. B. Ross-Murphy, *Ber. Bunsen-Ges. Phys. Chem. Chem. Phys.*, 1998, **102**, 1534-1539.
13. J. M. Guenet, *Macromol. Symp.*, 2006, **241**, 45-50.
14. R. F. Doolittle, *Annu. Rev. Biochem.*, 1984, **53**, 195-229.
15. M. E. Morales, V. Gallardo, B. Clares, M. B. Garcia and M. A. Ruiz, *Journal of Cosmetic Science*, 2009, **60**, 627-636.
16. S. Basu, C. P. Marini, F. G. Baumann, D. Shirazian, P. Damiani, R. Robertazzi, I. J. Jacobowitz, A. Acinapura and J. N. Cunningham, *Annals of Thoracic Surgery*, 1995, **60**, 1255-1262.
17. M. P. Linnes, B. D. Ratner and C. M. Giachelli, *Biomaterials*, 2007, **28**, 5298-5306.
18. A. H. Henschen-Edman, in *Fibrinogen*, 2001, vol. 936, pp. 580-593.
19. U. Larsson, *Eur. J. Biochem.*, 1988, **174**, 139-144.

20. E. A. Ryan, L. F. Mockros, J. W. Weisel and L. Lorand, *Biophys. J.*, 1999, **77**, 2813-2826.
21. S. Y. Sun, T. Salim, L. H. Wong, Y. L. Foo, F. Boey and Y. M. Lam, *Journal of Materials Chemistry*, 2011, **21**, 377-386.
22. C. Storm, J. J. Pastore, F. C. MacKintosh, T. C. Lubensky and P. A. Janmey, *Nature*, 2005, **435**, 191-194.
23. K. M. Weigandt, D. C. Pozzo and L. Porcar, *Soft Matter*, 2009, **5**, 4321-4330.
24. H. Kang, Q. Wen, P. A. Janmey, J. X. Tang, E. Conti and F. C. MacKintosh, *Journal of Physical Chemistry B*, 2009, **113**, 3799-3805.
25. Y. C. Lin, N. Y. Yao, C. P. Broedersz, H. Herrmann, F. C. MacKintosh and D. A. Weitz, *Physical Review Letters*, 2010, **104**, 4.
26. T. van Dillen, P. R. Onck and E. Van der Giessen, *Journal of the Mechanics and Physics of Solids*, 2008, **56**, 2240-2264.
27. A. E. X. Brown, R. I. Litvinov, D. E. Discher, P. K. Purohit and J. W. Weisel, *Science*, 2009, **325**, 741-744.
28. P. R. Onck, T. Koeman, T. van Dillen and E. van der Giessen, *Physical Review Letters*, 2005, **95**.
29. K. M. Weigandt, L. Porcar and D. C. Pozzo, *Soft Matter*, 2011, **7**, 9992-10000.
30. K. M. Weigandt, N. White, D. Chung, E. Ellingson, Y. Wang, X. Fu and D. C. Pozzo, *Submitted to the Biophysical Journal*, 2012.
31. G. M. Newbloom, K. M. Weigandt and D. C. Pozzo, *Macromolecules*, 2012, **45**, 3452-3462.
32. G. M. Newbloom, K. M. Weigandt and D. C. Pozzo, *Soft Matter*, 2012, **8**, 8854-8864.

Chapter 2

Experimental Methods: Small Angle Scattering

The fibrillar gels examined in this research have distinct multiscale structural features over size scales ranging from the atomic scale to hundreds of microns. This is because fibrillar gels are bulk materials with an underlying bicontinuous structure that spans the entire medium. The fundamental structures in these materials are fibers with lengths on the order of microns, cross-sections on the order of tens or hundreds of nanometers and internal structural features on the order of angstroms or nanometers. There are few techniques that facilitate the simultaneous characterization of bulk structural features of gels spanning orders of magnitude in scale. Furthermore, given the relatively low solids fraction (<5 vol% for all samples) it is highly desirable to characterize samples *in situ* without removing the volatile solvents (i.e. measurement under vacuum). For these reasons small angle scattering (SAS) is the primary analytical technique utilized to characterize the bulk structure of gels in this research.

In this research we have primarily utilized small and ultra-small angle neutron scattering (SANS and USANS), but small angle x-ray or light scattering (SAXS or

SALS) are also occasionally utilized and referred to herein. This chapter introduces the fundamental concepts of small angle scattering that are directly relevant to the research described throughout this dissertation. In the first section, the general theory of small angle scattering is introduced and key differences between neutron, light, and x-ray scattering are explained. In the second section, experimental details relevant to the SANS and USANS experiments performed in this research are described. Several more advanced neutron scattering techniques and experimental set ups that are utilized in this work, including rheoSANS and 1-2 plane shear SANS are also introduced. Finally, in the third section, several strategies for analyzing neutron scattering data are presented including classic relationships such as Porod and Guinier plots as well as 1D and 2D model fitting.

Small Angle Scattering Theory

In static small angle scattering, a highly collimated beam of radiation is directed through a material of interest, in our case fibrillar gels of P3HT or fibrin. When the incident radiation passes through the gel several interactions may occur. First, the radiation may be transmitted through the sample with no interaction at all. A fraction of the radiation will be absorbed and may cause sample activation (neutrons) or heating (x-rays). Finally, some of the incident radiation will interact with the gel and change propagation direction, or scatter. In static small angle scattering we are primarily interested in this last type of interaction, though transmission and absorption are of relevance to experimental design and analysis.

Static small angle scattering experiments are used to measure coherent elastic scattering that arises due to local variations in the sample composition. The main difference between light, x-ray and neutron scattering is in the way the incident radiation interacts with the sample material. In small angle neutron scattering, interaction with the atomic nuclei gives rise to scattering, whereas differences in electron density and index of refraction lead to scattering of x-rays and light respectively. A schematic depicting neutron and x-ray interactions with materials at the atomic scale is depicted in Figure 2.1. The scattering vector q is the difference between the propagation vector of the scattered and incident radiation beams and is related to the scattering angle (θ) and radiation wavelength (λ) by Equation 2.1:

$$q = \frac{4\pi}{\lambda} \cdot \sin\left(\frac{\theta}{2}\right) \quad \text{Equation 2.1}$$

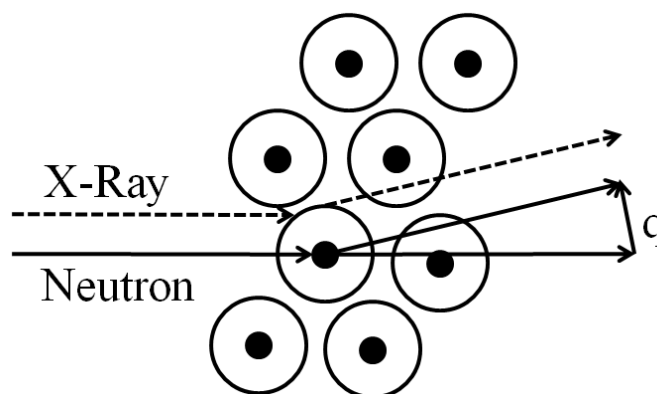


Figure 2.1: Illustration of an x-ray and neutron scattering event. The scattering vector q is also depicted.

The scattering intensity as a function of the scattering vector q is effectively a measurement of the sample structure, where q is inversely related to characteristic distance with $D=2\pi/q$. The size resolution of a scattering experiment is defined by the wavelength of the incident radiation and the accessible scattering angles. Because the

wavelength of light tends to be significantly larger than x-rays or neutrons, light scattering is frequently used to probe larger structural features, whereas x-rays and neutrons are more suitable when studying nanoscale features. The SAXSess x-ray scattering instrument available in the Pozzo lab uses the Cu-K α reflection obtained from an x-ray tube and produces monochromatic x-rays with $\lambda=1.54$ Å. Neutron wavelengths are on the order of 1 to 20 Å and can be tuned for specific experimental requirements. Neutron and x-ray scattering can be used to characterize structural features over very similar size ranges. However, there are several differences between these two techniques that may make one preferable over another depending on the material of interest and experimental constraints.

SAXS experiments are performed either with lab-scale instruments that use x-ray tubes or with x-rays generated at synchrotron sources at national labs. The advantage of visiting a synchrotron source is the ability to design short measurements that yield good statistics because of the high flux produced at these facilities. With neutron scattering, experiments are either performed at a spallation source or a nuclear reactor. Both of these sources require the use of highly specialized facilities. While the neutron flux is substantially lower than x-ray flux at comparable facilities, neutron scattering has several distinct advantages.

The primary advantages of neutron scattering are related to the way in which neutrons interact with most materials. Neutrons only interact with the nucleus of atoms, whereas x-rays interact with the electrons. Electrons statistically occupy a much larger volume and therefore the transmission of x-rays is reduced relative to neutrons. This limits the types of sample cells that can be used in x-ray scattering experiments. Consider

that the glass capillaries used in the x-ray scattering experiments described in this dissertation have 10 μm thick walls. In neutron scattering, the quartz windows used in a typical sample cell are ~ 1 mm thick and only minimally impact the neutron transmission. In fact, some of the neutron scattering experiments described in this research require highly specialized equipment, for example a rheometer, to be placed in the beamline. This is not usually feasible with x-ray scattering.

The intensity of scattered radiation is dependent on the contrast between different phases in the sample material or rather differences in the scattering length density ($\Delta\rho_{SLD}$). The scattering length density of a material probed with x-rays is directly proportional to the local electron density. As the electron density scales with the atomic number, materials from elements widely separated on the periodic table, such as gold particles in water, will have a high scattering contrast. Whereas materials with elements that are near each other on the periodic table tend to have much less contrast as in the case of organic molecules in water. With neutron scattering, the scattering length is not necessarily correlated with atomic number. In fact, different isotopes of the same element can have widely varying scattering length densities. The most useful example of this is hydrogen and deuterium. Isotopic substitution of hydrogen with deuterium can be used to dramatically change the scattering length density of a material without substantially affecting the material properties. For example, the scattering length density of hydrogenated water is $-5.6 \times 10^{-7} \text{ cm}^{-1}$, and the scattering length density of deuterated water is $6.3 \times 10^{-6} \text{ cm}^{-1}$. A list of the scattering lengths and other key properties for each of the elements used in this work is presented in Appendix 1, Table A1. The scattering length density (ρ_{SLD}) can be calculated directly if the composition and density are known

with Equation 2.2, where b_{ci} is the bound coherent scattering length, and v_m is the molecular volume.

$$\rho_{SLD} = \frac{\sum_{i=1}^n b_{c_i}}{v_m} \quad \text{Equation 2.2}$$

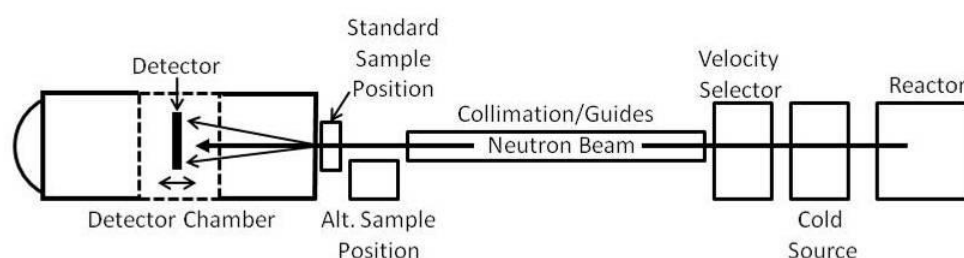
The most obvious benefit of isotopic substitution in neutron scattering experiments is for the optimization of scattering properties in a given system, but it can also be used as an analytical tool. In a three component system, adjusting the scattering length density of the solvent by partial deuteration such that it matches the scattering length density of one of the other components will isolate the scattering from the third component and effectively create a two-component system. To determine the contrast match point or an unknown scattering length density, a technique referred to as contrast variation is used. In this technique, several (~5) solutions with constant analyte volume fraction but varying solvent isotopic composition are prepared. The change in the scattering intensity with solvent deuteration is used to determine the contrast match point or to extract the scattering length density of the unknown material. Contrast variation is used in Chapter 6 to determine the scattering length density of P3HT fibers.

General Experimental Methodology

Small Angle Neutron Scattering

The NG3 and NG7 30 m SANS instruments at the NCNR in Gaithersburg, MD have both been utilized in this work and a general diagram of these instruments is depicted in Figure 2.2.¹ Thermal neutrons ($\lambda = 2.38 \text{ \AA}$) are produced by a 20 MW nuclear reactor and cooled with a liquid hydrogen cold source producing neutrons with

wavelengths between $5 < \lambda < 12 \text{ \AA}$. A velocity selector is used to specify the wavelength and define the spread of neutrons. Generally, larger wavelengths extend the low- q limit at the cost of lower overall neutron flux, which makes longer measurement times necessary. The neutrons are collimated over a 16 m pre-sample flight path with optional guides. As a general rule of thumb, the path length of the collimation optics should be approximately equal to the sample to detector distance. An open air sample area, approximately 1 m in length, contains a sample chamber that holds up to ten samples or an alternate Huber stage that can be used as a platform for various special sample environments. Once the neutrons pass through the sample they enter a 15 m long detector chamber. A single 2D 64 cm square detector with adjustable detector to sample distance is used to measure the scattered neutrons. By utilizing 2-3 detector distances, both SANS instruments measure scattering over a large q -range that spans $0.001 < q < 0.6 \text{ \AA}^{-1}$ and corresponds to length scales between 1 and 400 nm. For the SANS measurements performed in this research, we typically used three configurations to span the entire accessible q -range. Further details about the SANS instrumentation at the NCNR is available in the literature.¹



Figure

2.2: Schematic of SANS Instrument.

Ultra-Small Angle Neutron Scattering

While the SANS instrument accesses length scales as high as 400 nm, gels have larger structural features including fiber length and fractality on the order of many

microns. The perfect crystal diffractometer or ultra small angle neutron scattering instrument (USANS) measures scattering over a q -range between $0.00005 < q < 0.005 \text{ \AA}^{-1}$ expanding the maximum resolvable size to $\sim 20 \text{ \mu m}$.² The USANS is fundamentally different from the SANS in that scattered neutrons are probed at discrete q -values selected by a rotating perfect silicon crystal (220). Figure 2.3 shows a schematic of the NIST USANS instrument. The instrument is located directly off the reactor with a dedicated thermal neutron port (BT5) and utilizes 2.38 \AA neutrons. Additional details about this instrument are available in the literature.²

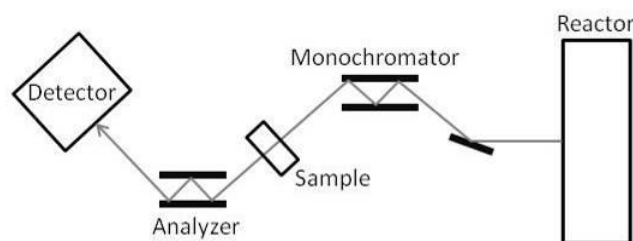


Figure 2.3: Left: Schematic of perfect crystal diffractometer on BT5 thermal neutron beamline at the NCNR. Right: Depiction of slit smearing.

The USANS instrument is invaluable for seamless characterization of fibrillar gels with neutron scattering. However, several limiting factors must be taken into account. First, because the scattering is measured at discrete q -values, 6-12 hours is typically required to measure the scattering for each sample. So, unlike SANS which can be used to measure the structure in evolving samples, USANS measurements can only be performed on samples with structures at equilibrium that are stable over many hours. Additionally, the USANS instrument has a relatively high background so the data from weakly scattering (low concentration) samples may be very noisy, making these materials not well suited to the technique. Finally, the USANS instrument has a rectangular slit

shaped aperture rather than a circular or “pinhole” aperture. The Anton Paar SAXSess also utilizes a line collimation. The resulting data from these instruments is therefore slit-smearred. Despite the additional mathematical complications associated with smearred data, it has a clear advantage of increasing the neutron flux without reducing the q -range (increasing q_{min}). Igor macros developed at NIST are used to mathematically correct for the slit smearred.³

Data Reduction and Absolute Scaling

One of the great advantages of neutron scattering is that it is highly quantitative and sensitive to the concentration, composition, and structure of materials. When the raw data is treated to account for the instrumental background, configuration and total flux, the absolute intensity is directly proportional to the particle volume fraction ($I(q) \propto \phi r$). In this section the corrections and background measurements necessary for data reduction will be described. In this work the NIST Igor based reduction algorithms developed by Steve Kline were utilized for all SANS data corrections.³

To correct raw scattering data, the background scattering from the sample holder, the background noise from the environment (dark noise), and the detector sensitivity must be accounted for. Additionally, the sample area (beam size), thickness, and position with respect to the neutron detector must be known. Finally, the transmission of neutrons through the sample and the total beam flux must also be measured. The total beam flux is measured with an attenuated empty beam transmission measurement. The scattering and transmission are measured for each sample and an empty sample holder. The dark noise is measured by placing a neutron absorbing (boron coated) tile to block the beam while the scattering is measured. The sensitivity of individual pixels on the detector is

determined by measuring the scattering from a piece of poly(methyl methacrylate) (Plexiglas™), which has flat scattering over all q (no structure dependent scattering).

To correct for the dark noise and sample holder scattering, the following equation is utilized:⁴

$$I_s(q) = \frac{I_{s+ec}(q) - I_n}{T_{s+ec}} - \frac{I_{ec}(q) - I_n}{T_{ec}} \quad \text{Equation 2.3}$$

Where I_s is the scattering contribution from the sample alone, I_{s+ec} is the scattering intensity from the combined empty cell and sample, I_{ec} is the scattering contribution from the empty cell alone, I_n is the intensity of the dark noise, T_{s+ec} is the transmission through the sample and empty cell combined, and T_{ec} is the transmission through the empty cell alone. The scattering is scaled to the absolute cross-section ($d\Sigma/d\Omega$) or absolute intensity $I(q)$ with Equation 2.3.⁴

$$I(q) = \frac{d\Sigma}{d\Omega} = \frac{I_s(q)}{I_0(\lambda)T_s d\Delta\Omega} \quad \text{Equation 2.4}$$

In this equation I_0 is the total neutron flux (from the empty beam transmission measurement), T_s is the sample transmission and is equal to T_{s+ec}/T_{ec} , d is the sample thickness and $\Delta\Omega$ is the solid angle over a single detector pixel. For scattering of isotropic samples, the data can be further reduced to a 1D scattering curve as a function of q by taking a radial average about the beam center. For non-isotropic materials, further reduction is situation specific and will be discussed in more detail when applicable in later chapters.

Advanced sample environments

Another advantage to neutron scattering that was mentioned in the general theory section is the relatively high transmission of neutrons through many materials. This enables the design of specialized equipment for use in neutron beam lines beyond the typical sample holder with quartz windows. In order to directly compare the structural and mechanical or other properties of these gels it is often necessary to directly measure these properties simultaneously. In this section, several more advanced neutron scattering experimental techniques are described that allow for measurement of samples under applied shear, combined mechanical-structural measurements and combined electrical-structural measurements.

RheoSANS and 1-2 Plane SANS

Non-linear mechanical properties often arise as a result of underlying structural transitions that can occur in viscoelastic materials under an applied shear stress. There are few experimental techniques that facilitate the characterization of structural transitions under flow. Here we combine neutron scattering with shear rheology or other specialty shear cells to directly link the mechanical and structural properties of fibrillar gels.^{5, 6} In Chapter 7 we describe the results of a RheoSANS experiment that was designed to explore the evolution of mechanical and structural properties during the gelation and dissolution of thermoreversible P3HT organogels. In Chapter 4 we report the use of a specialty 1-2 plane shear cell to detect and quantify fiber alignment in a fully formed fibrin gel as it is deformed to increasing strain amplitude.

For RheoSANS experiments, an Anton Paar MCR 501 rheometer has been equipped with custom designed Couette cells for use in neutron beam-lines at the NCNR

in Gaithersburg, MD.⁶ A schematic of the rheoSANS apparatus is provided in Figure 2.4. Currently, only concentric cylinder geometries are available and require between 5 and 12 mL sample volume. The cup and bob are fabricated from either titanium or quartz because of the limited interaction of these materials with neutrons (see Appendix 1, Table A1 for the absorption cross-section, the incoherent scattering cross-section and other relevant parameters). In a typical rheoSANS experiment, the rheometer is lowered into the beam line and the beam is aligned so that it passes through the sample either radially (1-3 plane) or tangentially (2-3 plane). Temperature is controlled using heated or cooled N₂ that flows between the cup and a secondary quartz container. To prevent evaporation, low viscosity silicon oil is used in the solvent trap as a barrier to prevent evaporation of the organic solvent during heating and cooling cycles over several hours of experiments.

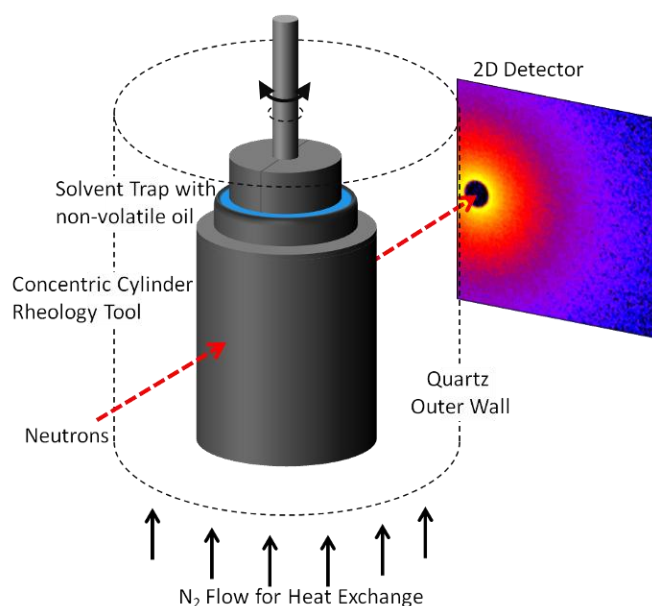


Figure 2.4: Schematic of rheoSANS apparatus. Figure not to scale

As mentioned above, using rheoSANS the structure can be measured in the 1-3 (radial or flow-vorticity) and 2-3 (tangential or shear-vorticity) planes. A third plane, the 1-2 or shear-flow plane also exists, but would require that the neutron beam be directed

vertically through the gap between the concentric cylinders. The scattering from shear aligned systems is dependent on the orientation of the neutron beam relative to the direction of flow. For example, let us consider a small section of a sample located between two parallel slabs as depicted in Figure 2.5. In this case the material of interest is a suspension of isolated nano-rods of some finite length. When the suspension is at rest the cylinders are isotropic and have no orientation. In this case, the scattering through any of the three planes will yield identical information. However, upon the application of shear the rods may align into the direction of flow. The velocity will vary from zero at the stationary wall to the maximum velocity at the moving plate. Therefore the relative alignment of the nanorods will likely depend on their position relative to these two plates.

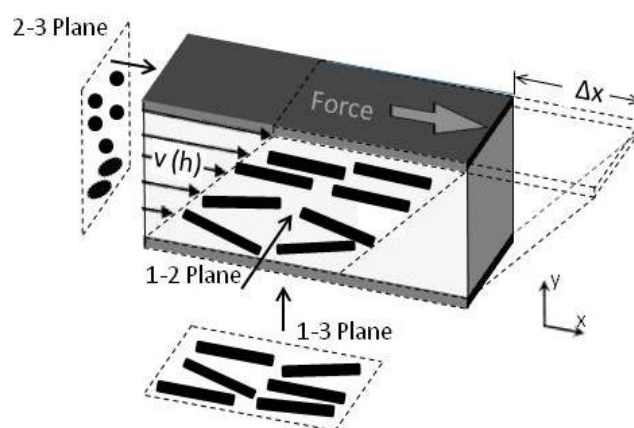


Figure 2.5: Illustration of scattering planes accessible with shear scattering techniques.

A depiction of a possible observed structure through each plane is illustrated in Figure 2.5. In the 2-3 plane, the fibers should be mostly aligned parallel to the direction of the beam and the resulting scattering will reflect the fiber cross-section. Near the stationary plate the cross-section may appear more ellipsoidal due to incomplete alignment of the fibers. Through the 1-3 plane, the fibers will be largely aligned into the direction of flow. Fibers that are near the stationary wall may not be fully aligned,

however there is no way to distinguish the relative position of non-aligned fibers with respect to the shear plane, so the non-oriented fibers will appear to be randomly distributed through the suspension. It is only in the 1-2 plane that fiber alignment can be accurately measured with respect to position between the plates. In this case alignment is observed as it was in the 1-3 plane, but the degree of alignment can be measured as a function distance from the plates.

Because the 1-2 plane is not accessible with a conventional rheometer or shear cell, a special 1-2 plane Couette shear cell was developed and originally used to observe the shear induced phase separation in solutions of wormlike micelles.⁵ A schematic of the 1-2 plane shear cell is provided in Figure 2.6 highlighting the direction of the neutron beam relative to the direction of shear. The 1-2 plane shear cell consists of a 48.7 mm diameter by 5 mm thick rotating disk with a 50 mm diameter outer shell (gap = 1.3 mm).

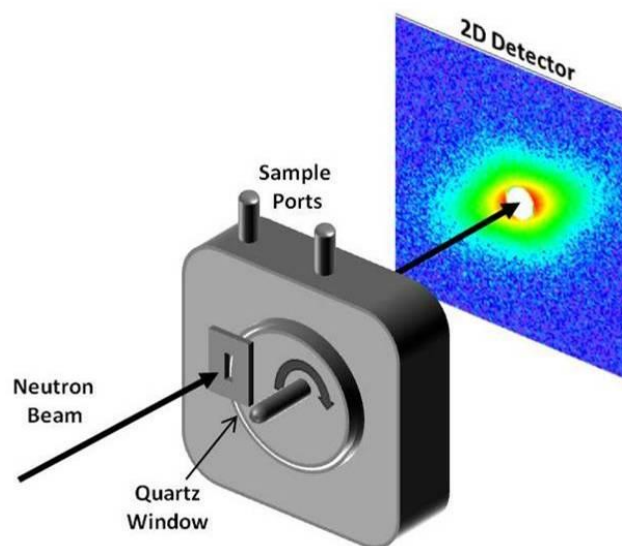


Figure 2.6: Schematic of 1-2 shear cell SANS instrumentation. Figure not to scale.

The instrument is configured with a small rectangular sample aperture (1 mm by 3 mm). Both the disk and the outer wall are composed of aluminum and two quartz windows that

provide high neutron transparency through the sample gap. Additional technical details of the shear cell have been previously described in the literature.⁵

The 1-2 plane shear cell is fundamentally different from the rheometer in that no mechanical measurements are made with this apparatus, so these experiments must be coupled with separate rheology measurements. However, unlike the rheometer, the motor that controls the angular rotation is interchangeable for various applications such that the shear cell can be used to achieve very high shear rates in flow studies, or very precise strain control for fibrin strain hardening experiments.

Several limitations should be considered when planning experiments with the shear cell. First, the 5 mm sample thickness is quite large for neutron scattering experiments and may give rise to multiple scattering effects in strongly scattering samples. Also, the 1×3 mm sample aperture is very small and therefore the neutron flux will be ~40× smaller than what is typically measured in a radial rheoSANS measurements. For this reason the scattering experiments in the 1-2 shear cell may require long measurement times and like the USANS, time dependent sample changes may result in unreliable experiments. However, for samples with reasonable temporal stability, 1-2 plane-SANS experiments can provide detailed structural data for materials under applied shear stresses.

Conductivity SANS

Advanced sample environments are not restricted to shear-cell type apparatus'. Many other types of sample environments exist including pressure cells, furnaces, electrophoresis cells and devices for applying magnetic fields. Our group (Newbloom et al.) has developed a portable, temperature controlled, conductivity-SANS apparatus

(depicted in Figure 2.7).⁷ A standard NIST 2 mm sample holder design is utilized except that a solvent resistant polymer is used to insulate between metal windows facilitating electrical measurements. LCR meter leads are attached near the edges of the conductive metal windows. An aluminum block with two slots for the sample cell and a second temperature reference cell was machined to fit onto a Torrey Pines Peltier plate with an operating temperature range from -10 to 100 °C. In practice the sample cell is aligned into the neutron beam and the scattering experiment is operated independently of the Peltier. Simultaneous temperature, conductivity, and SANS measurements are made throughout the duration of the experiment.

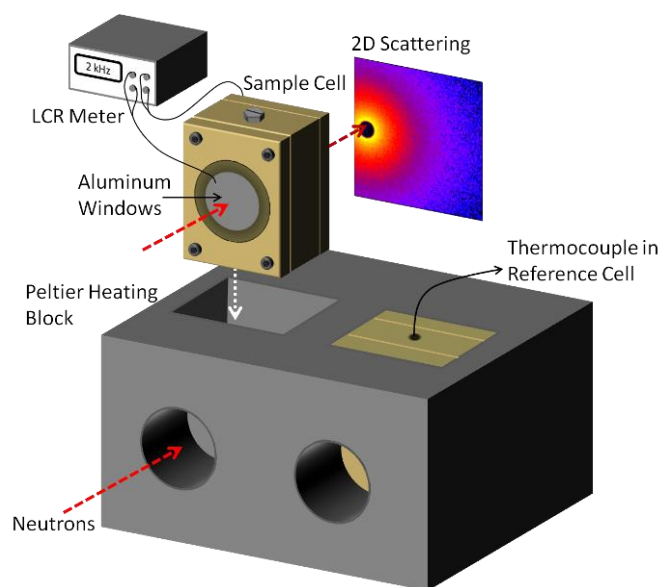


Figure 2.7: Schematic of conductivity-SANS experimental set up. Figure not to scale.

Data Analysis

Once scattering data has been obtained, corrected, and converted into absolute scale, structural information can be determined. Let us consider a typical scattering pattern for nanofibers in dispersion. The 1D scattering intensity from a suspension of

monodisperse titanium rods that are 100 nm long and 10 nm in diameter in deuterated water is plotted as a function of the scattering vector (q) in Figure 2.8 (left). This curve will have a number of characteristic features that are typical of elongated fiber-like structures. At very high- q a series of characteristic peaks that arise from the constructive and destructive interference patterns of the neutrons interacting with the individual particles are observed and are related to the particle size. For structures with a perfectly smooth surface, the intensity will vary as $I \propto q^{-4}$ at high- q , corresponding to length scales that are smaller than the characteristic dimensions of the particles (in this case at $q > 0.05 \text{ \AA}^{-1}$). This region is known as the Porod region. For fibrillar systems, at some intermediate- q there is a gradual reduction of the slope and the intensity will vary as $I \propto q^{-1}$ at intermediate- q . The transition between these slopes is referred to as a Guinier region and in fibrillar systems the onset of the first Guinier region is related to the cross-sectional dimensions of the fiber. At even lower- q , if the fibers are sufficiently short, a second Guinier region occurs where the scattering intensity becomes flat. The onset of this second Guinier region is an indication that the measured q -range is sufficient to probe the length of the fibers.

Particle size monodispersity is often an idealized, but not realistic case. In this research, the fibrillar systems have substantial polydispersity in the cross-sectional dimensions. Even a relatively narrow distribution of particle sizes can dramatically impact the characteristic scattering pattern. In Figure 2.8 (right) the scattering from a dispersion of fibers that are monodisperse in length with $L=100$ nm and polydisperse in radius with an average radius of 5 nm that is characterized by a Schulz distribution with a polydispersity index of 0.2. The polydispersity index, PD, is defined as one standard

deviation over the number average particle radius. The addition of polydispersity to this model nanorod system dramatically changes the scattering pattern. The new scattering pattern is the sum of the scattering that is measured from each particle in the system. In the polydisperse system the characteristic peaks at high- q are no longer measured and instead a steady $I \sim q^4$ Porod slope is measured. Also the transition to both Guinier regions is shifted to lower- q and the intensity as q approaches zero is larger. This is because the scattering from large particles is more intense than for small particles.

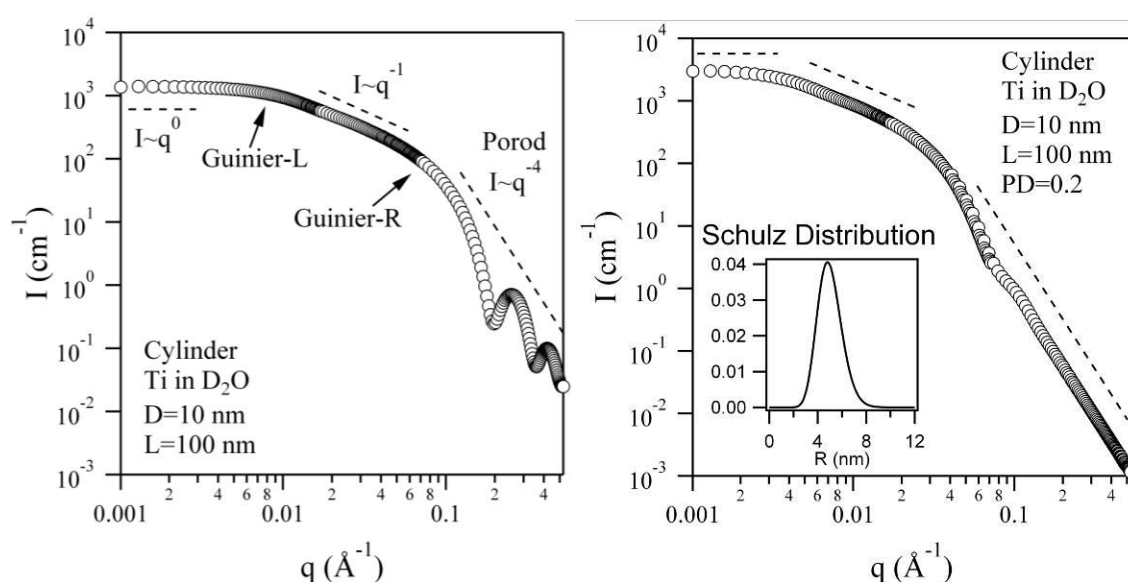


Figure 2.8: Left: Scattering produced from isolated monodisperse titanium cylindrical rods (average 10 nm in diameter and 100 nm long). Right: Scattering from cylinders with polydispersity in the radius with a 0.2 polydispersity index using a Schulz distribution.

There are several different strategies for analyzing scattering data to obtain specific structural parameters. Typically, one of three general approaches is taken. These include direct analysis of the data using standard plots and empirical models, data modeling, or application of inverse Fourier transforms to obtain pair-distance distribution functions. Each of these methods has distinct advantages and disadvantages. We have made extensive use of both the direct analysis methods and the data modeling

approaches. The details for the application of these analyses to fibrillar systems are presented in detail in the following pages.

General Structural Analysis

Guinier Analysis

A Guinier analysis can be used to determine the radius of gyration of particles. The benefit of using this simple method over a model fitting approach is that the radius is obtained directly from the scattering data. Additionally the radius of gyration can be determined without knowing the exact form factor (shape) of the particles. Unfortunately, this technique does not quantify particle polydispersity.

For fibers there are potentially two separate radii of gyration: the cross-sectional radius of gyration (R_{g-x}) and the whole particle radius of gyration (R_g). For a fiber the whole particle radius of gyration is extracted from Equation 2.5.⁴

$$I(q) = I(0) \exp\left(-\frac{q^2 R_g^2}{3}\right) \quad \text{Equation 2.5}$$

R_g is extracted from a linear fit of the scattering data as $q^2 \rightarrow 0$ from the Guinier plot, where $\ln(I)$ is plotted as a function of q^2 as shown in Figure 2.9 (left). With some additional information about the cross-section of the fiber it is possible to extract the length of the fiber. For a cylinder the radius of gyration is related to the length (L) and radius (R) of the average particle by Equation 2.6.⁴

$$R_g^2 = \frac{L^2}{12} + \frac{R^2}{2} \quad \text{Equation 2.6}$$

To determine the absolute length and radius of the cylinder, a second radius of gyration related only to the cross-sectional dimensions (R_{g-x}) must be determined. The cross-sectional radius of gyration is determined from the intermediate Guinier region using Equation 2.7.⁴

$$I(q) = \frac{I(0)}{q} \exp\left(-\frac{q^2 R_{g-x}^2}{2}\right) \quad \text{Equation 2.7}$$

To determine R_{g-x} , a cross sectional Guinier plot is utilized with $\ln(qI)$ plotted as a function of q^2 . From this plot the slope from a linear fit of the scattering data as $q^2 \rightarrow 0$ is extracted and is equal to $-\frac{R_{g-x}^2}{2}$ as shown in Figure 2.9 (right). For a cylinder the average radius is related to R_{g-x} by the relationship described in Equation 2.8:⁴

$$R_{g-x}^2 = \frac{R^2}{2} \quad \text{Equation 2.8}$$

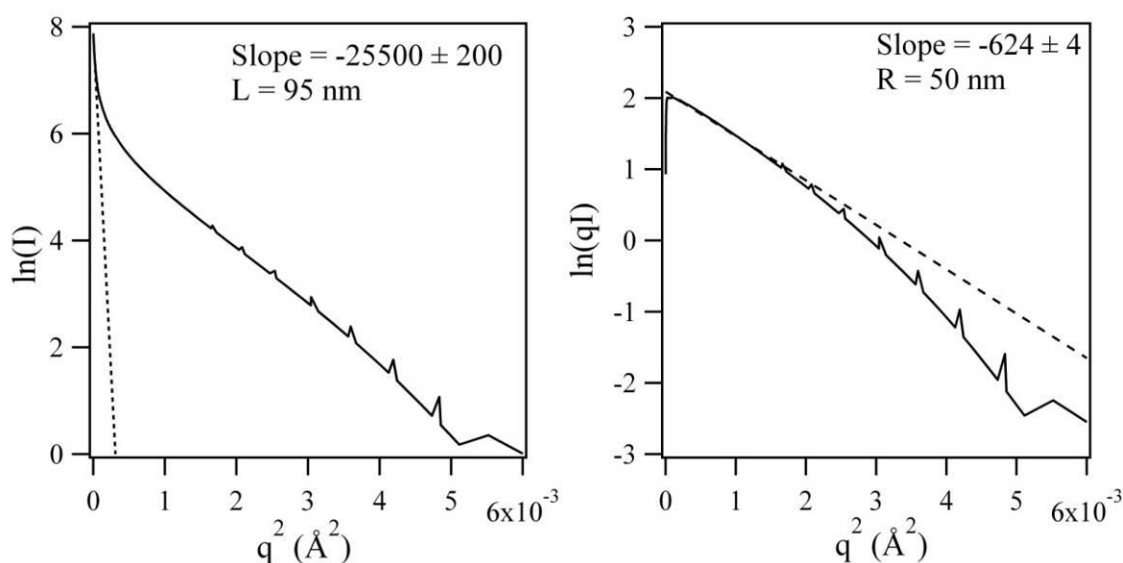


Figure 2.9: Left- Guinier plot and linear fit of titanium rods. Calculated fiber length (95 nm) is within 5% of actual fiber length Right- Cross-sectional Guinier plot and linear fit of titanium rods. Calculated fiber diameter is identical (50 nm) is identical to actual diameter.

The Guinier approach can be used to determine both the length and radius of fibers when scattering is probed to sufficiently low- q , or when the particles are sufficiently short. However, sometimes, especially for long fibers, only the intermediate Guinier regime is resolvable within the accessible q -range. In these cases the cross-sectional Guinier analysis remains a valid approach, but only the cross-sectional dimensions will be resolvable. This is the case for most of the fibrillar gels studied in this research.

Porod Analysis and Specific Surface Area

A Porod analysis can be used to determine the specific surface area (Σ) of fibers in a gel (or more generally the interfacial area in a variety of biphasic materials). Use of the Porod analysis requires that there be a sharp interface between the two phases, yielding the Porod slope ($I \propto q^{-4}$) described above and labeled in Figure 2.8. Here, the specific surface area is determined from the scattering using Equation 2.9.⁸

$$\lim_{q \rightarrow \infty} (I(q)q^4) = 2\pi(\Delta\rho_{SLD})^2 \Sigma \quad \text{Equation 2.9}$$

where Σ is the specific surface area in units of m^{-1} and $\Delta\rho_{SLD}$ is the scattering length density contrast between the fibers and the bulk solvent. The limit of Iq^4 as $q \rightarrow \infty$ is determined by plotting Iq^4 as a function of q as shown for the example polydisperse titanium rods in Figure 2.10. In this plot, the domain over which Iq^4 is independent of q is the Porod region. In this case $\lim_{q \rightarrow \infty} [I(q) \cdot q^4] = 9.04 \times 10^{-5}$. It is important to note that in an analogous plot for monodisperse particles, the higher order peaks will cause oscillations about this horizontal axis.

In this work, the specific surface area is an important parameter for P3HT gels, as increasing interfacial area in organic solar cells should correlate with increased exciton dissociation in these devices. In this case we are interested in maximizing the surface area per gram of polymer. The specific surface area can be converted into more relevant units of m^2/g by utilizing Equation 2.10:⁸

$$S_v = \frac{\Sigma}{\rho_m \phi_f} \quad \text{Equation 2.10}$$

where ρ_m is the mass density of the fibers. If ϕ_f is unknown, it can be determined directly from the scattering data by calculating the invariant.

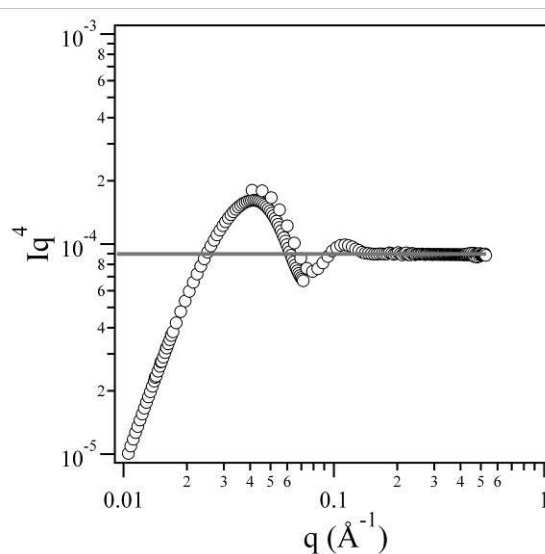


Figure 2.10: Porod plot for a dispersion of polydisperse titanium nanorods.

Invariant Analysis

The volume fraction of fibers in the gel (ϕ_f) is calculated directly from the total invariant (Q). This parameter is frequently known from the sample preparation. Therefore, the invariant tends to be a good consistency check for the accuracy of the integration and the value of the scattering contrast ($\Delta\rho$). For an isotropic two phased

system the scattering invariant relates the angle dependent, absolute scaled, scattering intensity (I) to the particle volume fraction (ϕ_f) and the scattering contrast between the two phases ($\Delta\rho_{SLD}$) with Equation 2.11.⁸

$$Q = \int_0^{\infty} I(q)q^2 dq = 2\pi^2 \phi_f (1 - \phi_f) (\Delta\rho_{SLD})^2 \quad \text{Equation 2.11}$$

The invariant is calculated directly by numerical integration of the scattering data. In this dissertation the invariant has been used to determine the volume fraction of fibers in both the P3HT and fibrin gels.

In the fibrin gels, the scattering data has two distinct and separated Porod regions. The lower- q Porod region reflects the interface between the whole fiber and the surrounding solvent. The high- q Porod region is attributed to the interface between the proteins and solvent within the fiber. Similar double Porod regions are commonly observed in the scattering profiles of porous and granular media. For systems exhibiting clearly distinguishable features on two distinct length scales, an analysis method has been developed to determine both the volume fraction of small pores within the “grain” (larger structures) as well as the volume fraction of the “grains”.⁸ We apply this previously established method of analysis to determine the protein volume fraction (ϕ_{Int}) within the fibrin fibers.

In order to measure ϕ_{Int} , the scattering data must be modified to isolate the intensity that is representative of the sharp interface between the proteins and the solvent within fibers. This requires the elimination of scattering intensity contributions that result from large structural features. This modification can be easily performed because the two

structural features are well separated in length scale. The modified intensity profile (I^*) is dominated by the contributions of the internal fiber structure.

$$I^*(q) = I(q) - I(q_*) \frac{q_*^4}{q^4} \quad \text{Equation 2.12}$$

In Equation 2.12, I is the absolute scattering intensity and $I(q_*)$ is the measured intensity at q_* where q_* is any value in the fiber-solvent or low- q Porod region as defined in Figure 2.8. The above description can also be understood by considering an analogous imaginary sample modification. A scattering profile similar to that of the modified intensity (I^*) would be obtained if it were possible to remove all buffer that lies between the fibers in the network without affecting the structure of the individual fibers. This would leave a compressed layer of protein and water with a porous nanostructure identical to that of the internal structure of the fibers. The invariant of the modified intensity (I^*) can then be used to determine the volume fraction of protein within the fibers (ϕ_{Int}). The invariant of the high- q Porod region (Q^*) is calculated with Equation 2.13:⁸

$$Q^* = \int_0^{\infty} I^* q^2 dq = 2\pi^2 \phi_f (1 - \phi_{Int}) (\Delta\rho_{SLD})^2 \quad \text{Equation 2.13}$$

In practice this analysis can be difficult to apply and a few limitations must be considered. In order to apply this analysis the second, high- q Porod slope must fall within the measured q -range. For the fibrin scattering, the high- q Porod slope occurs in a region of the data with relatively low intensity and is only slightly greater than the incoherent background. Because the scattering and background are of similar intensity, slight error in the background subtraction can lead to significant error in the second invariant

analysis. To ensure that this error is minimized, the background subtraction is made such that the high- q Porod slope is forced to an $I \propto q^4$ dependence. This analysis is very accurate when the concentration is high and the scattering is well above the background.

Model Fitting

While the generalized analysis techniques described above are very useful, it is often possible to extract more detailed information by utilizing a relevant model for the structure of the material and fitting the model directly to the reduced scattering data. The scattering intensity, or differential cross-section, from any two component system can be represented as the product of a form factor ($P(q)$), a structure factor ($S(q)$), and a scaling factor determined by the particle volume fraction and the scattering length density difference between the solvent and the particles (Eq. 2.14).⁸

$$I(q) = \frac{d\Omega}{d\Sigma}(q) = \phi_f (\Delta\rho_{SLD})^2 P(q) \cdot S(q) \quad \text{Equation 2.14}$$

The form factor is determined by the shape of the individual particles in the system and the structure factor is related to correlations between neighboring particles. In general, relatively low fiber volume fractions are used in this work so there is no structure factor at high- q . At low- q , however, the branched interconnected nature of the fibrillar gels must be accounted for. The structure factor at low- q is quantified by the fractal dimension D_f and is the result of the fractal like self-similarity over multiple length scales.

Fractal Dimension

The fractal dimension (D_f) describes the distribution of mass (m) in a material over multiple length scales, $m(x) \sim x^{D_f}$. A fractal dimension of one is expected for 1-D

cylinders, however in fibrillar gels the bifurcated structure and self-similarity gives rise to higher fractal dimensions at low- q . The easiest way to quantify fractal dimension is with a simple power law slope ($I(q) \sim q^{D_f}$). There are cases, though, where this is not an accurate method for determining the fractal dimension. This is particularly true for fibrillar systems with significant polydispersity or where the intermediate and low- q Guinier regions are not well separated as in the case of fibrin gels.

A fractal model based on the work of Teixeira is used to evaluate the network scale structure of the fibrin gels in Chapter 3.⁹ This is primarily reflected by the data collected with the USANS instrument ($q < 3 \times 10^{-3} \text{ \AA}^{-2}$). A least squares fitting algorithm is used to fit the data with the fractal model where the form factor and structure factor are defined in Equations 2.15 and 2.16 respectively.

$$P(q) = V_p^2 \left(\frac{\sin(qR_0) - qR_0 \cos(qR_0)}{3(qR_0)^3} \right)^2 \quad \text{Equation 2.15}$$

$$S(q) = 1 + \frac{\sin[(D_f - 1) \tan^{-1}(q\xi)]}{(qR_0)^{D_f}} \frac{D_f \Gamma(D_f - 1)}{[1 + q^{-2} \xi^{-2}]^{\frac{(D_f - 1)}{2}}} \quad \text{Equation 2.16}$$

In Equation 2.14, ϕ is the volume fraction of the primary spheres, V_p is the volume of the individual spherical particles, $\Delta\rho$ is the contrast between the two phases (fibers and solvent), q is the wave vector. $S(q)$ is the structure factor of the fractal which is defined in Equation 2.15. In this equation, D_f is the fractal dimension, ξ is the correlation length over which the fractal structure persists and R_0 is the radius of the individual spheres.

In order to simplify the analysis, the form factor of spherical subunits is used to construct the fractal network. While this analysis does not specifically apply to a

distribution of cylindrical fibers, it is possible to consider that the fibers themselves are composed of chains of spherical particles. This is a valid assumption at the very low- q values (USANS regime) used for model fitting because in this region the scattering is not sensitive to the shape of the individual building blocks.

Form Factors

In general, the gels studied in this dissertation are of sufficiently low concentration that, aside from the fractal dimension at low- q , the structure factor is equal to one. In this case the data can be modeled simply as the product of the form factor and the scale factor. Unlike the Guinier analysis described above, here we can account for polydispersity by modeling the system with as containing a defined distribution of fiber sizes. In this section, each the form factors that are used to fit data in this dissertation are described. The cylinder model, which is also utilized in this work, is defined in the section on 2D scattering analysis.

P3HT fibers are modeled with a parallelepiped form factor in Chapters 6 and 7. The parallelepiped form factor was derived by Mittelbach and Porod in 1961 and is described by Equation 2.17:¹⁰

$$P(q, a, b, c) = \frac{2}{\pi} \int_0^{\pi/2} \int_0^{\pi/2} \left[\frac{\sin(qa \sin \alpha \cos \beta)}{qa \sin \alpha \cos \beta} \frac{\sin(qb \sin \alpha \sin \beta)}{qb \sin \alpha \sin \beta} \frac{\sin(qc \cos \alpha)}{qc \cos \alpha} \right]^2 \sin \alpha d\alpha d\beta$$

Equation 2.17

In this equation, a , b and c are the fibrillar height, width and length, respectively. The random orientation distribution of parallelepipeds is accounted for by integrating over angles α and β .

The P3HT system is not well modeled by the parallelepiped model alone because a fraction of the polymer remains soluble even after gelation is complete. Soluble P3HT is modeled with a polymer chain with excluded volume form factor. The polymer excluded volume model was derived by Benoit in 1957 and is described by Equation 2.18: ¹¹

$$P(q) = 2 \int_0^1 dx(1-x) \exp \left[-\frac{q^2 a^2}{6} n^{2\nu} x^{2\nu} \right] \quad \text{Equation 2.18}$$

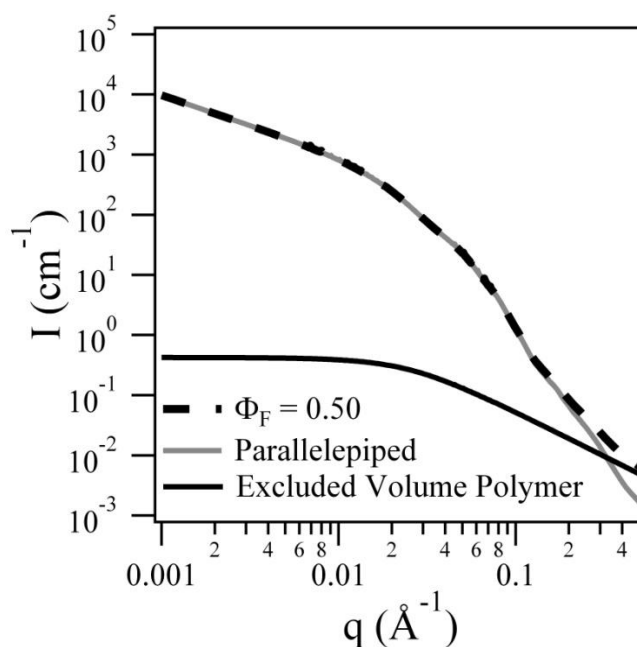
In this equation a is the statistical segment length, n is the degree of polymerization, and ν is related to the polymer chain conformation.

For systems with more than two components, modeling the data with a single form factor is not sufficient. In one sense P3HT gels are a two component system in that they are a mixture of polymer and solvent; however, the polymer exists in two distinct phases. The fibrillar polymer is well described by the parallelepiped form factor, but the soluble polymer is best described by the polymer excluded volume model. Even in fully evolved P3HT gels these two phases coexist making the gel effectively a three component system. The scattering from the various components are additive and a simple mass balance, defined in Equation 2.19 can be utilized to account for P3HT in fibrillar and soluble form.

$$I(q) = \phi_{P3HT} \Phi_F (\Delta\rho)^2 P_{PP}(q) + \phi_{P3HT} (1 - \Phi_F) (\Delta\rho)^2 P_{PEXV}(q) \quad \text{Equation 2.19}$$

In this equation P_{PP} is the parallelepiped form factor, P_{PEXV} is the polymer excluded volume form factor, ϕ_{P3HT} is the total volume fraction of P3HT the solution and Φ_F is the fraction of total P3HT that is in fibrillar form. By carefully constraining the experimental system, most of the parameters in the combined parallelepiped and excluded volume

polymer model are constrained so that only the fiber cross-sectional dimensions (a and b) and Φ_F are varied to fit the data. An example of this combined form factor for a model system composed of 30 mg/mL P3HT in D-p-xylene where $\Phi_F = 0.5$ is plotted in Figure 2.11 with the constituent polymer and fiber models. It is only at high- q that the excluded volume polymer model is significant. When the fiber conversion is lower, the inclusion of the excluded volume polymer model is even more important to obtaining a good fit to the experimental data.



2.11: Combined parallelepiped and excluded volume polymer model for P3HT gels

2D Form Factor Analysis

As described above, for randomly oriented objects, the scattering intensity is radially averaged and fit with a one-dimensional form factor, $P(q)$. For aligned, or partially aligned objects, the scattering intensity, $I(q)$, is anisotropic and is related not only the dimensions of the object, but also to the average particle orientation. However, in such a case, the traditional methods of analysis such as fitting to an analytical one-

dimensional form factor or the use of a cross-sectional Guinier analysis for the determination of fiber radius are no longer valid. Therefore, a two-dimensional model is necessary to quantify the structure (orientation and dimension) of anisotropic fibers. This approach is challenging and computationally expensive but, as we will demonstrate, it can provide valuable structural information that is often inaccessible through other techniques.

Here, the absolute intensity $I(\mathbf{q})$ at each detector pixel of the two-dimensional scattering profiles for each strain is fit with the 2D cylinder form factor, $P(\mathbf{q})$, using SansView:^{12, 13}

$$I(\mathbf{q}) = \phi_f \pi R^2 L (\Delta\rho)^2 P(\mathbf{q}) + bkg \quad \text{Equation 2.20}$$

where \mathbf{q} is the scattering vector, ϕ_f is the volume fraction of fibers, R and L are the radius and length of the fibers respectively, $\Delta\rho$ is the scattering length density contrast term, and bkg is the incoherent background. $P(\mathbf{q})$ accounts for the distribution of fiber orientations by averaging the cylinder form factor over the different angular distributions relative to the neutron beam. The generalized form factor for a distribution of oriented cylinders is defined by Equations 2.21 and 2.22:

$$P(\mathbf{q}) = \int_0^{2\pi} d\eta \int_0^\pi p(\theta, \eta) P_0(\mathbf{q}, \alpha) \sin \theta d\theta \quad \text{Equation 2.21}$$

$$P_0(q, \alpha) = \left(\frac{2 \sin(\mathbf{q}L \cos \alpha/2)}{\mathbf{q}L \cos \alpha/2} \frac{J_1(\mathbf{q}r \sin \alpha)}{\mathbf{q}r \sin \alpha} \right)^2 \quad \text{Equation 2.22}$$

where $p(\theta, \eta)$ is the probability distribution for the orientation of the fiber over which the oriented cylinder form factor, $P_o(\mathbf{q}, \alpha)$, is averaged, α is the angle between the fiber axis and the scattering vector \mathbf{q} , and J_1 is a first order Bessel function. The probability distribution for the orientation of the fibers is defined in terms of η , the orientation distribution in a plane parallel to the detector, and θ , the orientation distribution relative to the incident beam as illustrated in Figures 2.12. For the experiment presented in Chapter 4, the fibers are distributed isotropically with respect to θ , but anisotropically with respect to η . The determination of the orientation distribution will be discussed in Chapter 4.

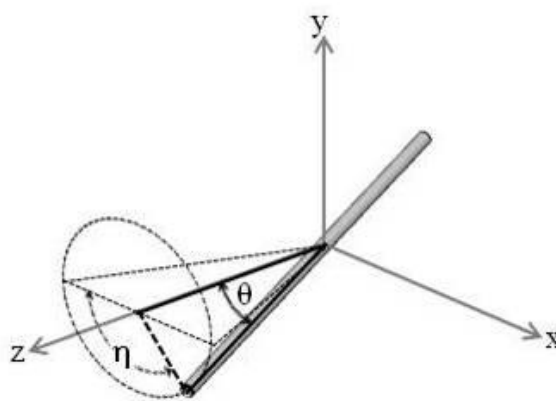


Figure 2.12: Definition of the angles θ and η of the oriented cylinder with respect to the incident beam (z-axis) and the detector plane (x-y plane).

Summary

Small angle scattering is a powerful technique for characterizing the multiscale structure of complex fluids and materials. Unlike other nanostructure characterization methods like scanning and transmission electron microscopy, small angle scattering facilitates measurements of liquid and gel materials in a variety of environments. In this dissertation we utilize a combination of small and ultra-small angle scattering to probe

the structure of fibrillar gels formed *in situ*. Taking advantage of the high transmission of neutrons through various materials, several specialized neutron scattering cells have been utilized in this work including a rheometer, a 1-2 plane shear cell, and a dielectric cell. These combined measurements are used to establish direct relationships between the structure, mechanical properties, and sometimes electrical properties of fibrillar gels.

References

1. C. J. Glinka, J. G. Barker, B. Hammouda, S. Krueger, J. J. Moyer and W. J. Orts, *Journal of Applied Crystallography*, 1998, **31**, 430-445.
2. J. G. Barker, C. J. Glinka, J. J. Moyer, M. H. Kim, A. R. Drews and M. Agamalian, *Journal of Applied Crystallography*, 2005, **38**, 1004-1011.
3. S. Kline, *Journal of Applied Crystallography*, 2006, **39**, 895-900.
4. Hammouda, B. 2011. Probing Nanoscale Structures - The SANS Toolbox.
5. M. W. Liberatore, F. Nettesheim, N. J. Wagner and L. Porcar, *Physical Review E*, 2006, **73**.
6. L. Porcar, D. Pozzo, G. Langenbacher, J. Moyer and P. D. Butler, *Rev. Sci. Instrum.*, 2011, **82**, 7.
7. G. M. Newbloom, K. M. Weigandt and D. C. Pozzo, *Macromolecules*, 2012, **45**, 3452-3462.
8. O. Spalla, *Neutrons, X-rays, and Light: Scattering Applied to Soft Condensed Matter*, Elsevier, Amsterdam, 2002.
9. J. Teixeira, *J. Appl. Crystallogr.*, 1988, **21**, 781-785.
10. P. a. P. Mittelbach, G., *Acta Phys. Austriaca*, 1961, **14**, 185-211.
11. H. Benoit, *Comptes Rendus*, 1957, **245**, 2244-2247.
12. A. Guinier and G. Fournet, *Small-angle scattering of X-rays*, Wiley, 1955.
13. <http://danse.chem.utk.edu/sansview.html>.

Chapter 3

Fundamental Characterization of Fibrin Structure and Rheology

Introduction

Biopolymer networks have unique mechanical properties, such as high elasticity and reversible strain hardening, which are distinct from those of most synthetic polymer networks. These properties are related to the unique structure of the network, the fibers and the proteins within the fibers.¹⁻³ Fibrin is a frequently studied model biopolymer system that is responsible for the formation of blood clots upon traumatic injury.⁴ The importance of this protein is twofold. First, the formation of thrombus in-vivo is of critical importance to prevent excessive blood loss upon injury. However, improper coagulation in the body also causes medical problems by preventing normal blood flow. This leads to cases of heart attack and stroke.⁵ Second, fibrin networks also show significant promise as a novel scaffolding material for growing functional tissues.⁶ In this application, fibrin clots are unique because they are inherently biocompatible,

biodegradable, and present the mechanical properties that are necessary to promote tissue formation. For these and many other important reasons, fibrin has been extensively studied since its discovery in the late 19th century.⁴ However, despite its obvious importance, the structural features of fibrin gels have been difficult to characterize in samples that are maintained in their native hydrated state. In addition, previous research focusing primarily on various microscopy techniques has been unable to thoroughly characterize fibrin gels over a large range of protein concentration and over a broad range of length scales.^{2, 7, 8} In this chapter, small angle neutron scattering and rheology are used to characterize the bulk structural and mechanical properties of coarse fibrin clots formed in D₂O saline solutions over a broad range of fibrinogen concentrations (1-40 mg/mL). Using a combination of small angle neutron scattering (SANS) and ultra small angle neutron scattering (USANS) the bulk structural features of unperturbed fibrin are seamlessly characterized over a large range of length scales between 1 and 15,000 nm.

Like many other biopolymers, fibrin is considered as a semiflexible polymer because its persistence length is of the same order of magnitude as the contour length, or in this case more appropriately the distance between the network junctions.³ This semiflexible polymer network structure is believed to be the origin of some of the unique rheological properties of fibrin.⁹ It is essential to have an extensive rheological characterization of these biopolymers to fully understand the physiological behavior of these materials. Many biopolymers such as actin, collagen, and fibrin show unique linear and non-linear rheological properties.⁹ For example, under low levels of deformation or strain, the elasticity of fibrin clots is characterized by a constant elastic modulus.

However, upon application of larger levels of strain, these biopolymers stiffen and undergo a phenomenon known as strain hardening.^{9, 10}

Several models and theories have been developed in an effort to understand the cause of this unique mechanical behavior.^{9, 10} At very low strains, when the semiflexible networks present a constant elastic modulus, the stiffness of the gel is related to the initial concentration of proteins with a power law relationship.³ The power law exponent is related to the nature of the interaction between the fibers. For a network of fibers the elastic modulus is predicted to have a stronger dependence ($G \sim C^{2.5}$) on the protein concentration compared to the case where the fibers are just entangled ($G \sim C^{2.2}$). In addition, models to describe the structural origin of the non-linear strain hardening response in these biopolymer gels are currently being debated and several alternative theories have been postulated.^{9, 10} We believe that SANS and USANS in combination with rheology may provide valuable information to develop these theories and relate the structural and mechanical properties of fibrin and other biopolymer networks.

Figure 3.1 shows a schematic of the three-dimensional structure of a coarse fibrin network over all relevant length scales. Fibrinogen, which is found naturally in the blood stream, is converted to fibrin by the enzyme thrombin. This enzyme is released locally near the region of trauma as the last factor in the coagulation cascade.⁴ Fibrin then self assembles into a half staggered linear array of protein molecules that is called a protofibril. Several protofibrils may also aggregate radially and form what are referred to as coarse fibers.^{11, 12} The total extent of lateral aggregation is controlled by the solvent properties including the ionic strength, pH and the isotopic composition of water.^{2, 12, 13} Fibrin fibers have a low internal protein volume fraction (ϕ_{int}) with estimates of about 80

percent of the total fiber space being occupied by water.^{4, 14, 15} The fiber's internal protein fraction has been previously estimated by evaluating the turbidity of fibrin samples¹⁴ and also by optically matching the index of refraction of clots containing very low fibrin concentrations.¹⁵ In this chapter, we describe a new method based on neutron scattering to directly and accurately obtain this information from fibrin clots that are formed over a much wider range of protein concentrations. This method determines the internal porosity of the fibers from the angular dependence of the scattering intensity $I(q)$.

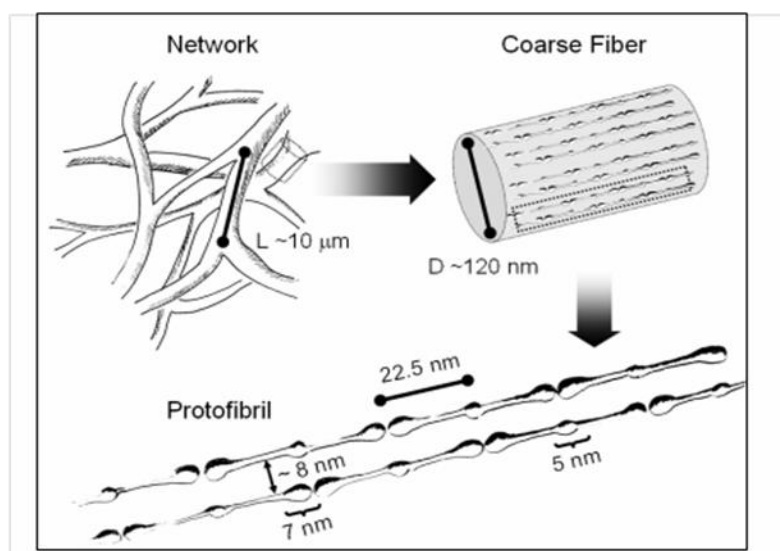


Figure 3.1: Schematic of fibrin features at different scales ranging from 1 nm-10 μm .

Structural and mechanical characterization of fibrin clots formed from solutions of fibrinogen at concentrations up to 10 mg/mL have been previously reported in the literature.^{2, 16} The normal range of fibrinogen concentration in the blood stream typically varies between 2 and 4 mg/mL, which are included in the previously characterized range. Electron microscopy has been commonly utilized to determine the basic structural properties fibrin gels. This technique has demonstrated that upon the addition of thrombin, fibrin forms a bifurcating network of cylindrical fibers with no visible dangling

ends.² While this is extremely valuable insight, the properties of the hydrated gel cannot be easily evaluated with electron microscopy. Optical techniques such as confocal microscopy, which do not require sample processing, have also been utilized to this end.⁷ However, optical techniques are limited not only by the minimum length scale of the fibrinogen features that can be characterized, but also by the opacity of the gels formed from higher concentrations of protein. More importantly, it has likely that the concentration of fibrin in a thrombus that is formed in-vivo is much higher than has been characterized in previous work.¹⁷

Small angle scattering techniques are ideally suited to characterize the bulk structural properties of clots formed at much higher concentration and in their native hydrated state. Furthermore, we use deuterated solvents to promote the lateral growth of fibers within the clots. The use of D₂O improves the resolution of the structural characterization due to the significant difference in the scattering length density between the hydrogen in the protein and the deuterium in the solvent.¹³ The complex structural features of fibrin clots also motivate the need for a rigorous approach to seamlessly characterize the hydrated structure of fibrin clots over a wide range of length and concentration scales. Neutron scattering is ideally suited for this because of the wide range of length scales that can be characterized with the same technique. In this study, the SANS technique provides information about the internal structure and the radial dimension of the fibers, while the USANS technique is used to characterize larger features including the fractal dimension of the network (D_f) and the correlation length (ξ) over which the fractal structure persists. Both techniques are performed on the exact same samples.

Materials and Methods

Sample preparation

Human alpha thrombin and fibrinogen solutions depleted of any plasminogen and von Willebrand factor are purchased from Enzyme Research Laboratories (South Bend, IN). Deuterated water containing 99.9% D₂O is obtained from Cambridge Isotope Laboratories (Andover, MA). The fibrinogen is dialyzed against a deuterated buffer composed of 0.5 M NaCl, 0.05 M Tris, and 99.9% D₂O with a pD of 7.4 in regenerated cellulose dialysis tubing over 12 hours. The composition of the buffer is selected to maximize the stability of the proteins while also promoting the formation of coarse fibers containing several protofibrils.¹³ Dialysis is performed until the final stock solution contains at least 98% deuterated water. The fibrinogen stock solutions in D₂O buffer are separated into aliquots and stored at -80 °C. Prior to final sample preparation, the protein solutions are thawed, diluted and filtered through a 0.45 syringe filter to remove any protein aggregates or dust. The final fibrinogen concentration is then determined from the absorbance at 280 nm using a UV-Vis spectrophotometer and an extinction coefficient of 1.6 mL/mg.¹⁴ Trace amounts of the protein Factor XIII are known to be present in the initial fibrinogen solution. This protein, when activated with calcium, promotes the formation of ϵ -(γ -glutamyl)lysine isopeptide bonds between adjoining protein monomers in fibrin fibers.¹⁸ To ensure the activation of the factor XIII protein, CaCl₂ is added to the filtered protein solution to a final concentration of 2.5 mM Ca⁺². Prior to polymerization, the fibrinogen solutions are also degassed under a -30 mmHg vacuum for 40 minutes. Degassing the sample is necessary to prevent the nucleation of microbubbles. The scattering contribution of bubbles at low angles can overcome the fibrin signal and render

the USANS data analysis unworkable. To initiate coagulation, 0.16 NIH units of thrombin per milliliter of the total solution is added to each fibrinogen sample just prior to loading it into the SANS cells or the rheometer. The thrombin concentration is sufficiently low to allow proper loading of samples into the rheometer and the neutron scattering cells before the polymerization begins to occur. After initiation, the gel is allowed to form in the sample holders over a period of 10 hours prior to testing.

Rheology

Rheological data is obtained with an Anton Paar MCR 301 stress controlled rheometer using a cone and plate geometry with a 2.5 cm diameter and a 1° angle. During polymerization, the samples are subjected to 0.1% strain oscillations at a frequency of 1 Hz for 10 hours in order to track the development of the clot and to ensure that the gel formation has reached completion. This is determined by reaching a plateau in both the elastic (G') and viscous (G'') moduli. A strain of 0.1% is found to be appropriate to track the gelation process while also being sufficiently small to prevent the alteration of the rheology and structure of the final gel. After complete polymerization, the linear moduli of the gel (G' and G'') are measured with a frequency sweep (0.0001 and 100 Hz) at a fixed strain of 1%. Subsequently, the instantaneous (non-linear) modulus of the gel is probed by performing a steady stress ramp and holding steady for one minute intervals at each stress level. The strain is measured just prior to each step in applied stress. In order to verify that the measured mechanical properties are not related to interfacial slip, the rheology is measured with various instrument configurations and surface materials. Additionally, step stress tests are also tracked as a function of time to ensure that the

samples do not experience any creep, slip or yielding during the application of the stress. None of these effects are found to occur in these samples.

Neutron Scattering

Small angle neutron scattering (SANS) and ultra small angle neutron scattering (USANS) measurements are performed on the same samples at the Center for Neutron Research at NIST in Gaithersburg, Maryland. SANS measurements are performed on the NG3 30 meter instrument.¹⁹ Measurements are made at three detector distances of 1.3, 7 and 13.2 meters to cover a broad q -range (0.002 to 0.3 \AA^{-1}) using neutron wavelengths of 5 \AA and 8.4 \AA . All of the SANS data are corrected for background and sample cell scattering, and is placed on an absolute scale by measuring the direct beam flux.²⁰ USANS measurements are performed on the BT5 perfect crystal diffractometer extending the measured q -range down to $4 \times 10^{-5} \text{ \AA}^{-1}$.²¹ Data is reduced and desmeared using the NIST Igor based software.²⁰

Results

Rheology

Fibrin gels were mechanically characterized to determine the variations in the moduli as a function of fibrinogen concentration. At low strain, fibrin gels exhibit linear viscoelasticity and the modulus of the gel is independent of strain. The storage modulus of the gel was characterized within the linear viscoelastic limit at 1% strain over a frequency range bounded by 0.0001 and 100 Hz. Figure 3.2 shows the storage and loss modulus as a function of frequency as well as the storage modulus at 1 Hz as a function

of fibrinogen concentration. The modulus increases slightly with increasing frequency but it is relatively constant overall. Also, the storage modulus is consistently greater than the loss modulus, which indicates that the material is a gel over the entire probed frequency range. The modulus dependence on fibrinogen concentration is well fit by a power law equation with $G' \sim C^{2.22}$. This is almost identical to the expected dependence for solutions of entangled semi-flexible fibers ($G' \sim C^{2.20}$) but it is lower than the prediction for crosslinked networks ($G' \sim C^{2.5}$).³

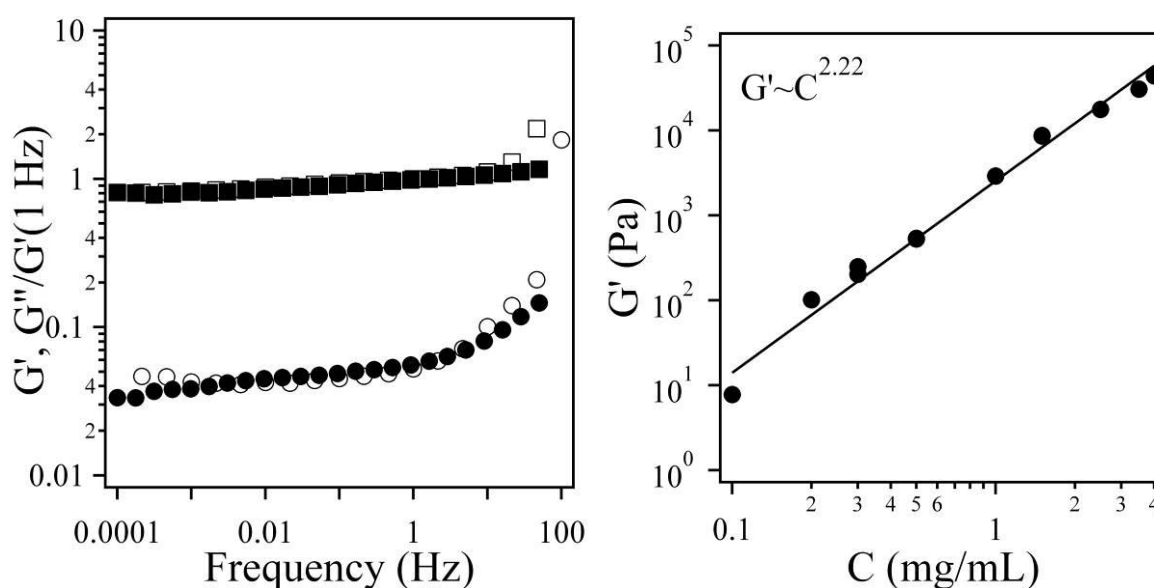


Figure 3.2: Rheology of fibrin clots within the linear viscoelastic limit. Left: The frequency dependence of modulus of 2 [G' (\square), G'' (\circ)] and 25 [G' (\blacksquare), G'' (\bullet)] mg/mL fibrin clots normalized by $G'(1 \text{ Hz})$. Right: Storage modulus (G') of ligated fibrin clots formed from fibrinogen of varying concentration (1-40 mg/mL) and fit with a power law equation.

It is also well known that fibrin gels exhibit non-linear behavior with increasing strain. More specifically fibrin gels are strain hardening. A slow stress ramp was used to characterize the non-linear rheology of fibrin as a function of strain. Figure 3.3 shows the instantaneous modulus ($G_{\text{Inst}} = d\gamma/d\sigma$) as a function of strain. It is evident that the non-linear rheology of the fibrin gel is highly dependent on the initial fibrinogen

concentration. At a concentration of 3 mg/mL, the fibrin gel begins to harden at about 3% strain and the gel modulus increases gradually until the gel begins to break giving rise to a steep decrease above 150% strain. The 5 mg/mL fibrin gel behaves similarly, but the rate of the modulus increase becomes weaker between 10 and 40% strain. At higher concentrations, as represented by the 10 mg/mL data in Figure 3.3, a new region of strain-softening appears between 10 and 30% strain before the samples begin to stiffen

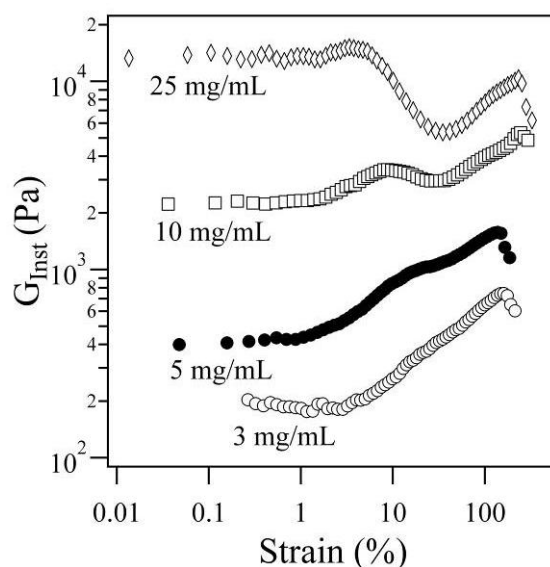


Figure 3.3: Instantaneous modulus (G_{Inst}) plotted versus strain for four fibrin samples of increasing concentration.

again. Finally, in fibrin gels containing much larger concentrations of fibrinogen (≥ 25 mg/mL) the modulus of the gel does not increase at 3% strain as previously observed. Instead, these samples show a steep reduction in the modulus at about 6% strain before the modulus begins to increase again at 30% strain. In this later range, the behavior matches the high strain behavior of the lower concentration samples. To the best of our knowledge, this complex rheological behavior at high fibrin concentrations has not been reported previously.

Neutron Scattering

The scattering data (SANS and USANS) for each sample are fully reduced, corrected for instrumental resolution (desmeared) and combined into a single scattering profile. The data covers an extremely broad range of q -values between 0.00004 and 0.3 \AA^{-1} that can be associated with features of sizes ranging roughly between 1 and 15,000 nm. Figure 3.4 shows the combined USANS and SANS scattering profiles for 3, 10 and 30 mg/mL fibrin gels normalized to the concentration of the samples. Identical structures, normalized in this way, should show overlapping scattering profiles. The data shown in Figure 3.4 is representative of all other scattering profiles that were collected for fibrin samples in the range of 1 to 40 mg/mL.

The changes in the scattering profiles in Figure 3.4 can be associated with the structural features of the fibrin network that are highlighted in Figure 3.1. At high- q ($> 0.01 \text{\AA}^{-1}$) there are two distinct plateaus in the intensity profile that correspond to the internal structure of the individual fibers. At intermediate- q ($0.001 < q < 0.01 \text{\AA}^{-1}$) the SANS data is mostly characterizing the structure of the fibers. The slope transition that occurs at 0.002\AA^{-1} is related to the average radius of the cylindrical fibers. Finally, at very low- q , in the USANS regime, the scattering is dominated by the structure of the network. In this region, the data can be used to determine the fractal dimension of the network, which is primarily dependent on the intensity slope in a log-log representation. In this q -region, a plateau can also be observed for the highest sample concentrations. This is characteristic of an inhomogeneous fibrin distribution over these larger scales. This feature also allows for the determination of a correlation length that is characteristic of the fractal structure. However, the plateau is only observed in the USANS region of

samples with the higher concentrations ($C > 10$ mg/mL). At lower fibrin concentrations, the low- q plateau occurs at length scales that are larger than the resolution limit of the USANS instrument.

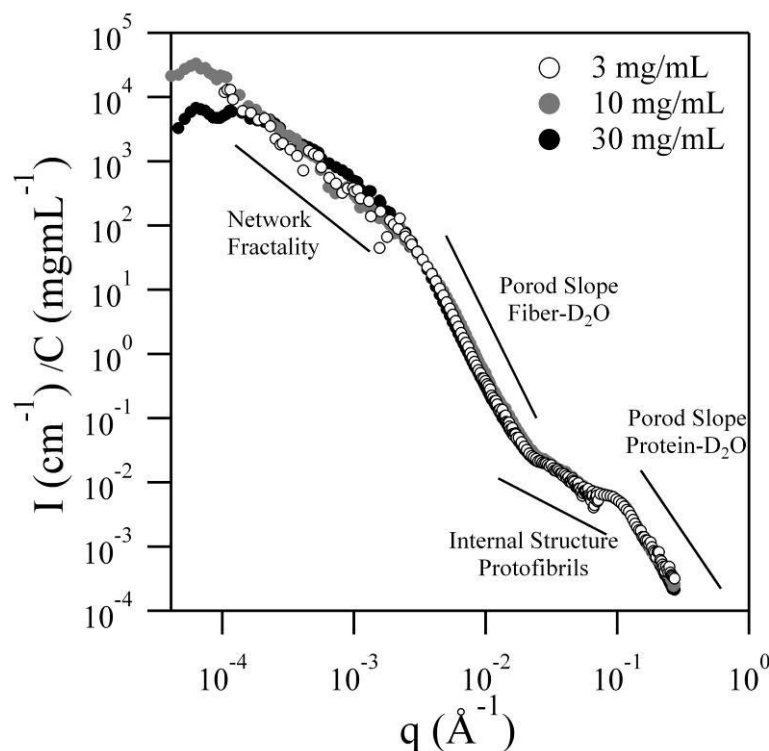


Figure 3.4: Combined SANS and desmeared USANS scattering profiles for fibrin gels formed from different concentrations of fibrinogen (3 mg/mL, 10 mg/mL, and 30 mg/mL) with intensity (cm^{-1}) normalized by concentration (mg mL^{-1}).

It is clear in Figure 3.4 that the most significant change in the scattering intensity occur in the very low- q range (USANS) corresponding to the network structure. All other features of the scattering profile remain relatively unchanged with increasing fibrinogen concentration. The low- q scattering of the 3 mg/mL fibrin curve does not have a low- q plateau in the measurable q -range. In contrast, the curves of both the 10 and 30 mg/mL samples present a plateau that shifts to higher- q as the concentration increases. In addition to the low- q variation, there are also slight variations in the scattering curves in the higher- q regions that are difficult to appreciate in the log-log representation. While

visual inspection of the curves permits a qualitative assessment of possible structural differences, careful quantitative analyses of the scattering data can provide detailed structural information. We perform a substantial analysis of the data using general model-independent analyses without having to make a priori assumptions of specific structural models that could lead to uncertainty in the results. Using a simple Guinier and Porod analysis, an effective cylinder radius and the internal protein volume fraction of the fibers can be determined directly.

Internal Structure

For all samples, the scattering profiles contain two easily distinguishable Porod regions. The low- q Porod region is a result of the interface between the coarse fibers and the solvent that fills the pores of the network. On the other hand, the high- q Porod region is caused by the sharp interface that exists between the individual proteins and the solvent that fills the gaps within each individual fiber. In Chapter 2, a double invariant analysis for determining the volume fraction of the protein within the fiber is described.²² We apply this previously established method of analysis to determine the protein volume fraction (ϕ_{int}) inside fibrin fibers and the overall protein volume fraction in gels that are formed over a broad range of concentrations.

The scattering contrast is determined from the scattering length density (SLD) of the deuterated solvent and the fibrinogen proteins. The SLD of the solvent was calculated to be $6.3 \times 10^{-6} \text{ \AA}^{-2}$ using the known atomic composition and the measured density. The SLD of fibrinogen in D₂O buffer at pD 7.4 was measured experimentally as $3.17 \times 10^{-6} \text{ \AA}^{-2}$ using the contrast variation technique described in Chapter 2. The total volume fraction of fibrinogen in the gel (ϕ_{Fib}) is calculated from the total invariant Q and Equation 2.11.

This parameter is also known from the sample preparation. Therefore, this process represents a good consistency check for the accuracy of the integration and the value of the scattering contrast ($\Delta\rho$). The calculated value of ϕ_{Fib} was found to be on average within 10% of the known value from the sample preparation.

The internal protein fraction (ϕ_{Int}), calculated from this invariant analysis, is plotted as a function of fibrinogen concentration in Figure 3.5. The internal protein fraction in the fibers increased steadily with concentration and the relationship was well fit with a power law function. Interestingly, the values are even lower than the previous estimates of about 20% protein.^{4, 14}

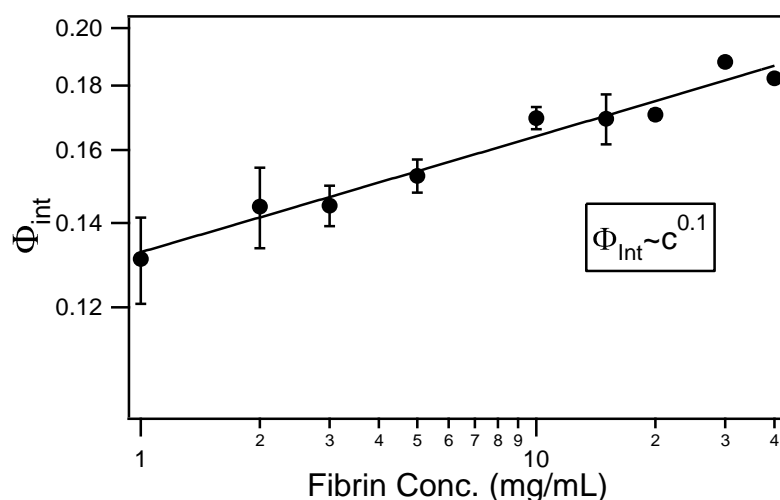


Figure 3.5: Internal volume fraction of fibrin fibers from multilevel invariant analysis. The error was determined from the uncertainty of the Invariant

Fiber Structure

A Guinier fit on the fiber cross-section was performed at the turn over between the low- q region and the first Porod region to determine the average radius of the fibrin fibers. The average radius is plotted versus the initial fibrinogen concentration in Figure 3.6. From the figure it is apparent that the radius varies very little with concentration.

However, careful inspection shows that there is a slight decrease in the radius with increasing fibrinogen concentration between 2 and 20 mg/mL. In contrast, at the higher concentration (30 and 40 mg/mL) the radius of the fibers was slightly larger than at the lower concentrations.

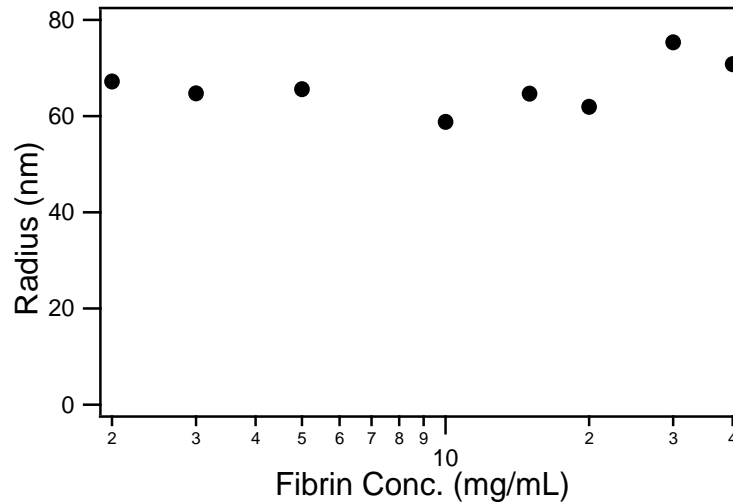


Figure 3.6: Radius of fibrin fibers determined from a Guinier analysis. The error, as determined from the Guinier fit is masked by the data markers.

From the values of ϕ_{int} and R , it is also possible to calculate the average number of protofibrils (N_P) in the radial cross-section of a coarse fibrin fiber. This is calculated using Equation 3.1:

$$N_P = \frac{\mu_{Fiber}}{\mu_P} = \frac{\phi_{int} \rho_m R^2}{\mu_P} \quad \text{Equation 3.1}$$

In this equation, N_P is the average number of protofibrils in a radial cross section of the fiber, ρ_m is the mass density of individual fibrinogen proteins (1.4 g/mL), R is the average fiber radius obtained from the Guinier analysis, and μ_P is the mass length ratio of a single protofibril.²³ The mass to length ratio of a single protofibril is assumed to be constant and is calculated by considering the half-staggered structure of fibrin and the known repeat

distance of 22.5 nm ($\mu_p = 340 \text{ kDa}/22.5 \text{ nm}$). We find that the average number of protofibrils changes negligibly for gels formed from initial fibrinogen concentrations of 20 mg/mL or less, Figure 3.7.

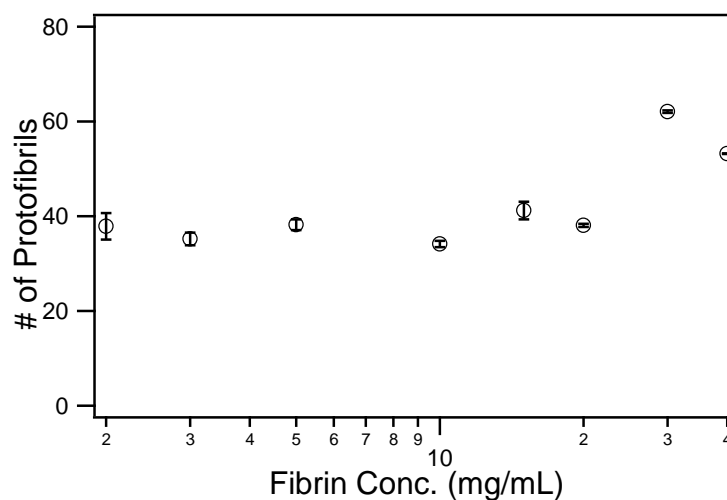


Figure 3.7: Average number of protofibrils per cross-sectional area as calculated from the mass to length ratio of the fibers and protofibrils.

Network Structure

The power law fit in the low- q region deviates from -1, indicating that the data cannot be modeled as discrete rigid cylinders. It is expected that both the flexibility of the fibers (form factor) and the network structure (structure factor) will have a significant contribution to the scattering data at low- q . However, coarse fibrin clots (thick) such as those studied in this work are composed of large and rigid fibers. Therefore, changes in the low- q scattering relate primarily to the network structure.

A fractal model based on the work of Teixeira and described in Chapter 2 was used to evaluate the network scale structure of the fibrin gel. This is primarily reflected by the data collected with the USANS instrument ($q < 3 \times 10^{-3} \text{ \AA}^{-2}$).²⁴ A least squares fitting algorithm is used to fit the data with the fractal model described by Equations

2.14, 2.15, and 2.16. The incoherent background was subtracted from the data prior to analysis and was fixed at zero for all models. The scattering length densities for the protein and the solvent were the same as used in the invariant analysis. The radius of the spheres, R_0 , was set equal to the radius of the cylinders calculated from the Guinier analysis. Thus only ξ , D_f , and ϕ were varied until χ^2 was minimized. While this analysis does not specifically apply to a distribution of cylindrical fibers, it is possible to consider that the fibers themselves are composed of chains of spherical particles. This is a valid assumption at the very low- q values (USANS regime) used for model fitting because in this region the scattering is not sensitive to the shape of the individual building blocks.

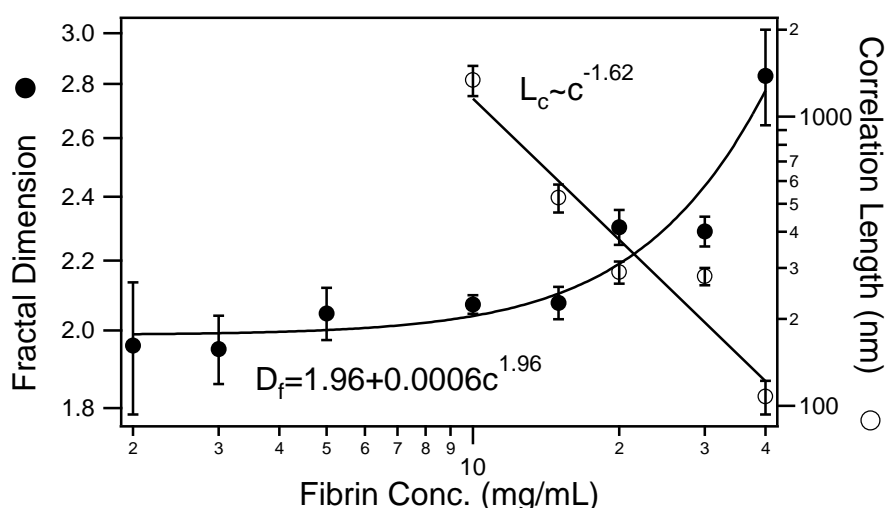


Figure 3.8: Fractal Dimension (D_f) [●] and correlation length (L_c) [○] of fibrin fibers determined by fitting the USANS scattering profile with the Teixeira fractal model.

Figure 3.8 shows that the fractal dimension (D_f) was relatively constant for gels containing up to 15 mg/mL protein. At these concentrations, the fractal dimension reached a value of two that is reasonable for networked systems.²⁵ At higher concentrations this value increased steadily according to a power law relationship. At 40 mg/mL the fractal dimension approaches a value of three which indicates the existence of regions of densely packed fibers in the gel.

The correlation length (ξ), which describes the finite domain over which the fractal dimension is valid, decreased consistently with increasing concentration. At high concentrations, the correlation length of the fractal structure becomes shorter and approaches the diameter of the fibers. The relationship between fibrinogen concentration and fractal correlation length is well approximated by a power law relationship. This relationship was extrapolated to estimate the correlation length of lower concentration fibrin gels. Assuming that this power-law trend persists at lower concentrations, the fractal correlation length of a 1 mg/mL fibrin gel is estimated to be about 49 μm . At these low concentrations fibrin gels can be imaged optically. Figure 3.9 shows a digital image of a 1 mg/mL fibrin gel taken from an inverted optical microscope using a 40X objective.

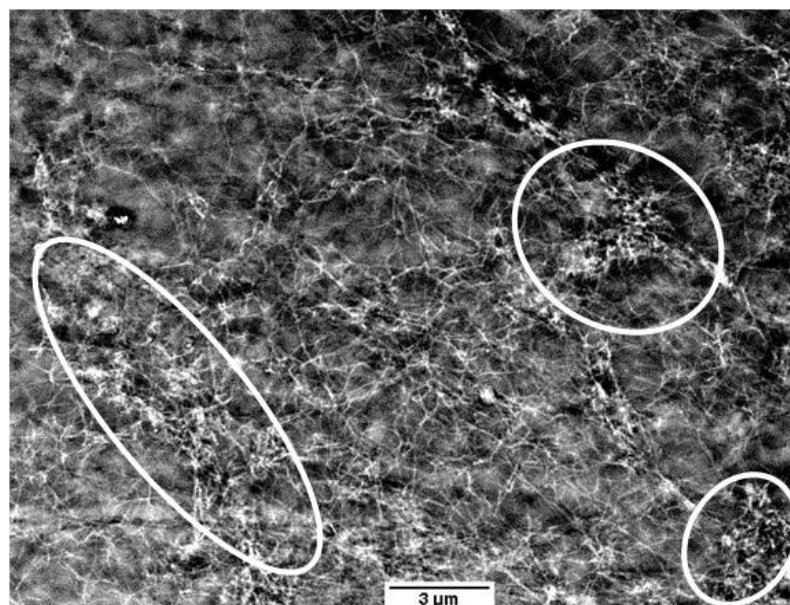


Figure 3.9: Optical microscopy image of a 1 mg/mL fibrin gel. Circled regions indicate higher density pockets of fibrin.

It is clear that the protein is distributed inhomogeneously throughout the gel, with regions of high fiber density separated by less dense regions. The separation between the discrete high concentration pockets is roughly of the same order of magnitude as the extrapolated

correlation length. The correlation length determined from the fractal model is not directly related to the mesh size of the network. Therefore, it cannot be related to the linear modulus as described by Macintosh et. al.³

Both the increasing fractal dimension and the decreasing correlation length indicate that, as the fibrin concentration increases, the network becomes denser and has more closely spaced high density pockets. In gels formed from the highest concentration protein solutions, the fractal correlation length is approaching the same order of magnitude as the fiber diameter. This suggests that the polymerization kinetics and protein and aggregate mobility may be significantly altered in higher concentration solutions during formation of the gel. The kinetic changes associated with increased protein concentration are likely responsible for the severe change in fractal dimension. This is also likely a reason for the significant change in the structure of the individual fibers at concentrations above 20 mg/mL. At this point there is little space in the gel for new fibers to form. Therefore, it may become more favorable for existing fibers to grow into larger structures than for new smaller fibers to form.

Discussion

Rheology

In the past, rheological measurements have shown that fibrin gels are strain-hardening like many other biopolymer networks. Most of these studies have found that, when the fibrin gel is strained, the storage modulus starts to increase sharply in the region between 1 and 10 % strain.^{9, 16} These studies have motivated a significant amount of work aimed at deciphering the origin of this unique mechanical response. However, most

of previous work has focused on the rheological properties of fibrin clots formed from initial fibrinogen concentrations of less than 5 mg/mL fibrinogen. In this study, the structure and rheology of fibrin formed over a broad range of initial fibrinogen concentrations were characterized. From Figure 3.3 it is clear that the non-linear rheological response with increasing strain is highly dependent on the fibrin concentration. For fibrin formed at the lower concentrations, the instantaneous modulus of the fiber became steadily stiffer with increasing strain. This was consistent with all of the results of previous work.^{9, 16, 26} However, significant inconsistencies with the strain hardening behavior were observed in fibrin gels formed from higher concentrations of fibrinogen. When these gels were strained to about 10% strain an unknown support in the gel significantly weakened and the gel began to soften. This response continued until it was strained to about 30% where it began to harden again.

This result must be considered within the context of the two theories that have been proposed to describe the strain hardening in fibrin gels. The theory proposed by Storm and colleagues postulates that the reversible strain hardening behavior of semi-flexible biopolymer networks is caused by an entropic response that is related directly to the persistence length of the fibers.⁹ These fibers will become fully extended when enough force is applied to remove them from their thermodynamically stable flexible state. The response of all the individual fibers then results in the macroscopic non-linear rheology of the network. Onck and colleagues propose an alternative theory where the thermodynamic undulations of the fiber are not the primary cause of strain hardening. Instead, these authors suggest that the reorientation of fibers and subsequent bending and stretching of fiber segments is the primary cause of the non-linear rheological response.¹⁰

It should be pointed out that these two theories are not mutually exclusive and that it is possible that both factors contribute in some extent to the strain-hardening response. Still, neither model predicts the strain softening that is observed at higher concentrations in this study. This intermediate strain softening could also be caused by damage to the internal structure of the proteins.

Theories have also been developed to correlate the linear rheological properties of semiflexible polymer networks to the structural features of these materials.^{3, 9} For a network of semiflexible fibers, such as fibrin, it is expected that the elastic modulus of the gel will increase with monomer concentration by a power of $C^{2.5}$. We used rheological measurements to compare the coarse fibrin clots with this prediction. Previous studies have reported a power law dependence with the exponent ranging between 1.66 and 2.1 for fibrin clots formed in H₂O buffers.^{2, 27} The power law relationship for coarse fibrin clots formed in D₂O had an exponent of about 2.26 in the range of fibrinogen concentrations between 1-40 mg/mL (Figure 3.2). This falls between the theoretical prediction and the measured values found previously for fine clots.³ It is also important to note that this power-law dependence is found to be valid throughout the whole expanded concentration range.

Structure Characterization

The structural properties of the individual fibers are also found to change with concentration. In previous studies the fiber radius and internal composition were measured primarily with optical and scanning electron microscopy.^{2, 15} Unfortunately, both of these techniques have limitations that make it difficult to characterize high concentration samples in their natural hydrated state. In addition, previous studies have

only focused on characterizing fibrin gels formed from solutions containing fibrinogen at concentrations typically observed in human plasma, 2-4 mg/mL. This work expands upon the previous research by increasing the studied range to an upper fibrinogen concentration of 40 mg/mL. The expanded concentration range is now physiologically relevant as it has been previously reported that fully formed thrombi can contain high fibrin concentrations.¹⁷ Neutron scattering was successfully used to characterize the bulk structural properties of these fibrin gels over the entire expanded concentration range. Some of the parameters that are directly extractable from the neutron scattering intensity curve include the average fiber radius (R) and the internal volume fraction of protein in the fibers (ϕ_{Int}). Previous studies also suggested that the internal volume fraction of fibrin in a fiber formed in H₂O ranges between 20 and 30 percent by volume.²⁸ The ease with which the volume fraction can be determined directly from the scattering curve makes this method preferable over previously used methods such as matching the index of refraction.¹⁵ This method should also be useful in the determination of ϕ_{Int} of other biopolymer systems. Furthermore, the volume fraction of protein in coarse fibrin fibers in this study ranged between 10 and 20 percent by volume which was substantially smaller than the values reported previously for fibers formed in H₂O solvents. The reduction in protein content in the fibers when compared with the literature values may be explained by one of two theories. Either the interaction between the fibers and the solvent in D₂O and H₂O are sufficiently different to cause the shift in solid density or this method of determining internal volume fraction is of a different accuracy than previous methods. Further study is necessary to determine how monomer concentration affects the internal structure of fibers formed in H₂O based buffers. The presented analysis should be easily

extended to x-ray scattering data (SAXS) which is more appropriate to characterize fibrin and other biopolymers formed in H₂O media.

The internal volume fraction was found to increase over the whole range of concentrations. Two possible causes for the systematic increase in internal protein volume fraction have been considered and illustrated in Figure 3.10. It is possible that, at higher concentrations, the individual proteins pack closer together within the fiber. This contraction would lead to a slight decrease in fiber radius and an increase in the protein volume fraction. Another theory is that, as the fibrinogen concentration increases, there is more available free protein to correct potential defects such as vacancies in the internal structure of the fibers. This would also result in an increased internal fiber protein fraction. The characterization of internal protein fraction as a function of concentration over such large range of monomer concentration is unique to this work. The ability to characterize the structural features of the network and individual fiber is important as it relates to the stability and break up of fibrin clots. Several studies have been published relating variations in the mass-length ratio of fibrin fibers to disease states.²⁹⁻³¹ It has been shown that a lower mass-length ratio, which corresponds to thin fibers, is related to reduced clot permeability and an increased risk of myocardial infarction.³¹ Furthermore, it stands to reason that the packing density of the protofibril units within the fibers may impact the clot break up even though this has not been explicitly considered in these studies.

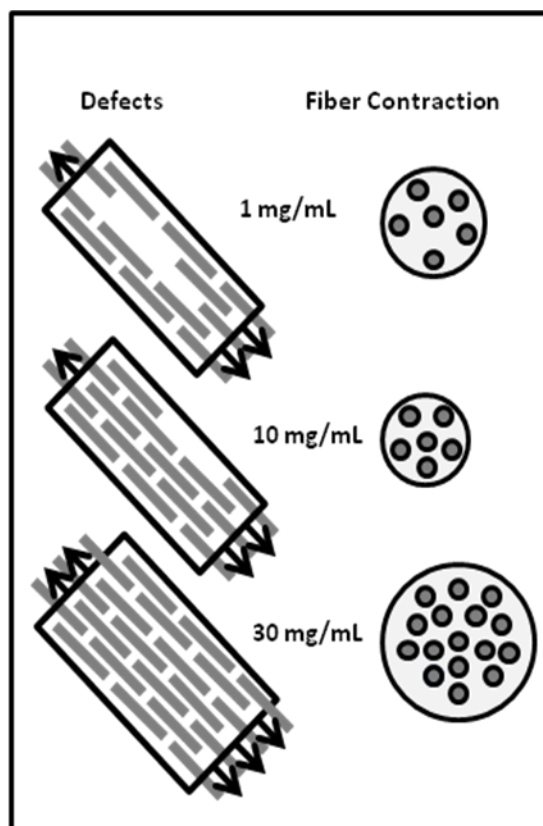


Figure 3.10: Illustration of two theories postulated for systematic increase in internal protein fraction. Left: Higher fibrinogen to thrombin ratio leads to fewer defects in higher concentration fibers. Right: Contraction of proteins within fiber leading to higher volume fraction with increased concentration.

Our work also shows that there was little variation in the average radius of fibers formed from fibrinogen monomer solutions with concentrations less than 20 mg/mL. Though the radius was approximately 65 nm it only decreased slightly with concentration over that range. The average number of protofibrils (mass-length ratio) in a fiber cross section was also found to be nearly constant at 40 protofibrils over this range. This suggests that the increase in internal protein fraction (Figure 3.5) was offset by the slight decrease in fiber radius (Figure 3.6). However when fibrin concentration was greater than 20 mg/mL the average radius of the fibers increased sharply to 70 nm and the average number of protofibrils also increased to about 55 nm. This change in fibrin structure

corresponded to concentrations at which the correlation length, extracted from the fractal model fit, began to approach the fiber diameter. Initially, as the concentration of the protein increased, the density of the fibrin network also increased but the distribution of fiber size remained constant. However, at even larger concentrations, the network is so dense that the fiber structure was altered favoring the formation of thicker fibers. This is also corroborated by the increasing fractal dimension and decreasing correlation length obtained from the fractal model. At the highest concentrations examined, 30 and 40 mg/mL fibrin, the correlation length is approaching the magnitude of the average fiber diameter. This suggests that the increased fiber size and protein content is a direct result of fiber crowding.

It must be clearly stated that the results presented in this work are specific to fibrin formed in buffer with deuterated water. Deuterated water was used in order to drive the formation of coarse fibers and to enhance contrast between the solvent and fibrin in the clot. The differences in fibrin clot conformation caused by using a buffer with D₂O are similar to changes caused by differences in buffer pH or salt concentration. In addition, the enhanced contrast allows both SANS and USANS experiments to be performed on the same samples so that the complete structure of the clots could be seamlessly characterized over length scales ranging from of 1 and 15,000 nm. This study is unprecedented in that all relevant length scales are characterized simultaneously and correlated to the rheological behavior of the materials. While it is also possible to use neutron scattering to characterize fibrin formed in an H₂O solvent, the contrast is much smaller and this makes USANS experiments unfeasible. X-ray scattering techniques such

as SAXS and USAXS are more appropriate methods to characterize fibers formed in water.

References

1. J. P. Collet, H. Shuman, R. E. Ledger, S. T. Lee and J. W. Weisel, *Proc. Natl. Acad. Sci. U. S. A.*, 2005, **102**, 9133-9137.
2. E. A. Ryan, L. F. Mockros, J. W. Weisel and L. Lorand, *Biophys. J.*, 1999, **77**, 2813-2826.
3. F. C. Mackintosh, J. Kas and P. A. Janmey, *Phys. Rev. Lett.*, 1995, **75**, 4425-4428.
4. R. F. Doolittle, *Annu. Rev. Biochem.*, 1984, **53**, 195-229.
5. J. W. Weisel, *Biophys. J.*, 1986, **50**, 1079-1093.
6. M. P. Linnes, B. D. Ratner and C. M. Giachelli, *Biomaterials*, 2007, **28**, 5298-5306.
7. A. Hartmann, P. Boukamp and P. Friedl, *Blood Cells Molecules and Diseases*, 2006, **36**, 191-193.
8. O. V. Gorkun, Y. I. Veklich, L. V. Medved, A. H. Henschen and J. W. Weisel, *Biochemistry*, 1994, **33**, 6986-6997.
9. C. Storm, J. J. Pastore, F. C. MacKintosh, T. C. Lubensky and P. A. Janmey, *Nature*, 2005, **435**, 191-194.
10. P. R. Onck, T. Koeman, T. van Dillen and E. van der Giessen, *Phys. Rev. Lett.*, 2005, **95**, 4.
11. J. W. Weisel, *Biophys. Chem.*, 2004, **112**, 267-276.
12. Z. Yang, I. Mochalkin and R. F. Doolittle, *Proc. Natl. Acad. Sci. U. S. A.*, 2000, **97**, 14156-14161.
13. U. Larsson, *Eur. J. Biochem.*, 1988, **174**, 139-144.
14. M. E. Carr and J. Hermans, *Macromolecules*, 1978, **11**, 46-50.
15. W. A. Voter, C. Lucaveche and H. P. Erickson, *Biopolymers*, 1986, **25**, 2375-2384.
16. J. V. Shah and P. A. Janmey, *Rheologica Acta*, 1997, **36**, 262-268.
17. S. Anand and S. L. Diamond, *Circulation*, 1996, **94**, 763-774.
18. J. J. Pisano, Finlayso.Js and M. P. Peyton, *Science*, 1968, **160**, 892-&.
19. C. J. Glinka, J. G. Barker, B. Hammouda, S. Krueger, J. J. Moyer and W. J. Orts, *J. Appl. Crystallogr.*, 1998, **31**, 430-445.
20. S. R. Kline, *J. Appl. Crystallogr.*, 2006, **39**, 895-900.
21. J. G. Barker, C. J. Glinka, J. J. Moyer, M. H. Kim, A. R. Drews and M. Agamalian, *J. Appl. Crystallogr.*, 2005, **38**, 1004-1011.
22. O. Spalla, *Neutrons, X-rays, and Light: Scattering Applied to Soft Condensed Matter*, Elsevier, Amsterdam, 2002.
23. S. Shulman, *Journal of the American Chemical Society*, 1953, **75**, 5846-5852.
24. J. Teixeira, *J. Appl. Crystallogr.*, 1988, **21**, 781-785.
25. M. A. De Spirito, G; Papi, M; , *Journal of Applied Crystallography*, 2003, **36**, 636-.

26. Q. Wen, A. Basu, J. P. Winer, A. Yodh and P. A. Janmey, *New Journal of Physics*, 2007, **9**.
27. P. A. Janmey, U. Euteneuer, P. Traub and M. Schliwa, *Journal of Cell Biology*, 1991, **113**, 155-160.
28. M. Guthold, W. Liu, B. Stephens, S. T. Lord, R. R. Hantgan, D. A. Erie, R. M. Taylor and R. Superfine, *Biophys. J.*, 2004, **87**, 4226-4236.
29. M. E. Carr, R. M. Dent and S. L. Carr, *Journal of Laboratory and Clinical Medicine*, 1996, **128**, 83-88.
30. J. P. Collet, Z. Mishal, C. Lesty, M. Mirshahi, J. Peynet, A. Baumelou, A. Bensman, J. Soria and C. Soria, *Thrombosis and Haemostasis*, 1999, **82**, 1482-1489.
31. K. Fatah, A. Silveira, P. Tornvall, F. Karpe, M. Blomback and A. Hamsten, *Thrombosis and Haemostasis*, 1996, **76**, 535-540.

Chapter 4

***In-Situ* Neutron Scattering Study of Structural Transitions in**

Fibrin Networks under Shear Deformation

Introduction

Fibrin gels are highly elastic and exhibit strain dependent non-linear mechanical properties that are unlike those of most synthetic polymer gels. Even at very small protein concentrations (<1 mg/mL), the fibrin network is very elastic and can effectively support haemostasis at the injury site. It is well accepted that the high elasticity and strain-hardening properties of fibrin are related to the structure of the individual proteins, the fibers, and the network.¹⁻⁴ However, the origin of strain-hardening in fibrin and other biopolymers is still not fully resolved and experimental evidence directly linking structural transitions to mechanical properties could provide especially valuable information.^{1, 5, 6}

In Chapter 3, it was shown that the linear and non-linear mechanical properties of fibrin gels are highly dependent on deformation and on fibrin concentration.⁷ It was also demonstrated that neutron scattering is an important tool for the characterization of fully hydrated fibrin gels over multiple relevant length scales (1-10,000 nm). This analysis yielded detailed information about the fibers, their internal structure and the network structure of the gel. The purpose of the current study is to further utilize neutron scattering as a tool to characterize the structure of a fully hydrated fibrin gel *in-situ* as it undergoes various degrees of shear deformation. The experimental results of this study are also discussed with respect to recent theoretical models that relate mechanical properties to changes in the gel and the fiber structure.^{3, 8-13} Numerous studies on fibrin mechanics have been reported throughout the literature.^{1-3, 10, 14-16} It is only recently, however, that fibrin gels have been characterized in their fully hydrated state over a wide range of concentrations that also extend to values that are relevant to the composition of excised blood clots *in-vivo* (>20 mg/mL).^{7, 17}

While the microstructure of fibrin gels is largely agreed upon, the origin of strain hardening is still under debate. In the past decade, several theories have emerged to describe the strain stiffening response of biopolymers and to relate this response to the structural features and transitions that occur upon deformation.^{9, 10, 18, 19} One important model, emerging from the semiflexible nature of many natural biopolymers, proposes that a reduction of the conformational entropy in individual stretched fibers leads to an increase of the modulus of the gel upon the application of strain.^{9, 10, 18} On the other hand, an alternative theory for the origin of the strain hardening is based on finite element simulations of discrete fiber networks.^{9, 19} This model postulates that reduced lateral

fluctuations cannot solely explain the high level of strain-hardening that is observed in biopolymer gels including fibrin. It is instead suggested that biopolymer networks undergo strain-hardening primarily as a result of non-affine network rearrangements that govern a transition from the bending of the fibers at crosslinks and bifurcations to the tensile stretching deformation of fibers.^{9, 19}

Several groups have also sought to expand upon these explanations, or to define the applicability of either model to specific systems.^{2, 3, 11, 18, 20-22} Kang et. al. suggest that gels containing coarse fibers are too rigid to undergo entropic strain-hardening and that there is no strain-hardening prior to the alignment of fibers as detected via birefringence.¹¹ Recent work from Brown et. al. accounted for the high extensibility of fibrin by providing experimental evidence (electron microscopy) that the fibers not only align as they are deformed, but also that the individual proteins unfold.^{3, 4} Unfolding leads to a measurable reduction in the radius of the protofibril bundle and in the expulsion of water from the individual fibers and the gel as a whole. The authors postulate that this structural transition is also key to the unique mechanical behavior of fibrin.

Several other studies link the unfolding of alpha helices within individual protein fibers to their high extensibility and complex mechanical properties.^{23, 24} The individual fibers are described as having multiple mechanical regimes with a linear response at low deformation that is followed by subsequent softening and then stiffening of the fiber. The softening regime is explained as the unfolding of the alpha helix followed by stiffening as the helix extends to its contour length prior to mechanical failure. Piechocka et. al. suggest that the extensibility of the fibers results from a reduction in the conformational

entropy of the flexible polypeptide chains that facilitate the formation of crosslinks between adjoining protofibrils.² This model (loose bundle model) assumes that strain-hardening is purely entropic, but that there is a reduction in lateral fluctuations at both network and inner-fiber scales over two separate strain stiffening regimes.² Additionally, very recent work suggests that the extension of the unfolded α C chain between adjoining protofibrils accounts for the high extensibility of strained fibrin gels.²⁵

In this chapter, *in-situ* neutron scattering experiments under controlled strain deformations are used to evaluate morphological transitions that occur in fibrin during strain hardening. Through the use of a special Couette shear cell, it is possible to characterize the structure of a clot while finite strains are applied. The shear cell is also unique in that it allows for probing of the deformed sample along the plane defined by the direction of shear strain and the direction of the deformation gradient (a.k.a. 1-2 shear plane).²⁶ With this cell, the deformation of the network and fiber alignment are directly observed and quantified. The advantages of performing a neutron scattering study are numerous. First, high protein concentrations (> 10 mg/mL) can be used and the resulting data represents a bulk average throughout the sample. In contrast, many optical and microscopic techniques do not penetrate the entire depth of the sample and/or are sometimes restricted to low protein concentrations due to the high turbidity of clots with coarse fibers. Second, by measuring the structure of the strained fibrin *in-situ*, we eliminate artifacts that could result from post processing and drying, as well as ensure experimental continuity because measurements at increasing values of strain are obtained from the same gel.

Materials and Methods

Sample Preparation

Human fibrinogen, depleted of plasminogen and von-Willebrand Factor, and human alpha thrombin are purchased from Enzyme Research Laboratories (South Bend, IN). Before use, the fibrinogen is dialyzed over 12 hours into a buffer composed of 0.5 mM NaCl, 0.05 mM Tris, 2.5 mM CaCl₂ with a pD of 7.4 in D₂O. Several dialysis steps are performed until the resulting protein solution has an isotopic composition of at least 98% deuterium. The presence of calcium ions is necessary to activate the enzyme factor XIII that promotes the formation of covalent crosslinks between proteins in the fibers.²⁷ Before polymerization, the fibrinogen solutions are also degassed under vacuum to prevent the formation of microscopic air bubbles that can affect the scattering signal. Just prior to loading, thrombin is added to the sample at a concentration of 0.16 NIH units per mL and fibrin formation is initiated. All samples are run at a concentration of 10 mg/mL of fibrinogen.

Neutron Scattering

For small angle neutron scattering (SANS), the sample is loaded into a special Couette shear cell that is able to probe the structure of samples under simple shear deformation along the 1-2 shear plane. The technical details of the shear cell are briefly described in Chapter 2 and have been previously detailed in the literature.²⁶ In order to form a fully established clot, the samples are allowed to gel for 10 hours prior to mechanical deformation. All neutron scattering experiments are conducted on the NG3 beam line at the NIST Center for Neutron Research in Gaithersburg, MD. For this

specific experiment, the instrument is configured with a rectangular sample aperture (1 mm by 3 mm), 8 Å neutron wavelength and a sample to detector distance of 14 m such that the scattering vector, q , is probed between 0.0024 and 0.027 Å⁻¹. The sample is sequentially strained to increasing magnitudes by rotating the central shaft of the shear cell (bob). During the scattering experiment, the sample is held at the specified rotation angle while the scattered neutrons are measured. It is determined that a count time of thirty minutes is required to obtain proper statistics with this instrument configuration. The two-dimensional scattering data is reduced to an absolute scale using the standard NIST Igor procedures.²⁸ A schematic of the shear cell is shown in Figure 2.6 highlights the direction of the direct beam with respect to the deformation direction.

Rheology

An Anton Paar MCR 301 stress controlled rheometer with a 25 mm cone and plate configuration and a 1° cone angle is used for all rheological measurements. Fibrin gelation is tracked with small amplitude (0.1% strain) oscillations at a frequency of 1 Hz. Strain of this amplitude is well within the linear viscoelastic limit ($\gamma_{LVE} \sim 1\%$) and will not affect the formation of the gel. A 10 hour gelation period is necessary to ensure that the extent of crosslinking is consistent between samples and with our previous work so that the properties of the gels are directly comparable.⁷ After the gelation period, a fine step-stress ramp is utilized holding each stress for one minute to determine the instantaneous modulus. The strain that is used for the calculation of the modulus is the value measured at the end of each step. Still, it is noted that the covalent crosslinks that occur due to the presence of factor XIIIa prevent any creep from occurring. To ensure that the sample is not slipping, shear stress ramps are conducted with parallel plate and concentric cylinder

geometries and the strain is also monitored as a function of time. The mechanical properties of the gel are independent of configuration and are free of any slip-induced artifacts.

Results

In Chapter 3 we reported that the non-linear rheology of fibrin gels is highly dependent on both the gel deformation and the initial fibrinogen concentration.⁷ In this chapter we focus on the structural and mechanical characterization of 10 mg/mL fibrin gels. These gels have a very distinct rheological signature: they harden, soften and then harden again at increasing levels of deformation.⁷ To elucidate the origin of the complex, non-linear mechanical properties of these gels it is necessary to characterize *in-situ* the structural properties of a fibrin gel as it is deformed. To this end, small angle neutron scattering is used to directly quantify the structural changes that occur as a fully formed fibrin gel is strained.

The two-dimensional scattering plots corresponding to various values of applied shear strain are presented in Figure 4.1. In the limit of low strain ($< 30\%$) the scattering data are isotropic indicating that the fibers in the network are randomly oriented. A quantitative analysis of the scattering signal of the unstrained fibrin is found to be in agreement, in terms of the average fiber diameter and the internal fiber structure, with previously reported SANS and USANS measurements.⁷ At higher values of strain ($\gamma > 30\%$), the onset of anisotropy in the 2D scattering profiles is characteristic of fiber alignment occurring within the gel. The extent of anisotropy in the scattering is observed

to increase with the strain level and the mean fiber alignment direction is also found to be at a finite angle with respect to the shear direction with almost no strain dependence.

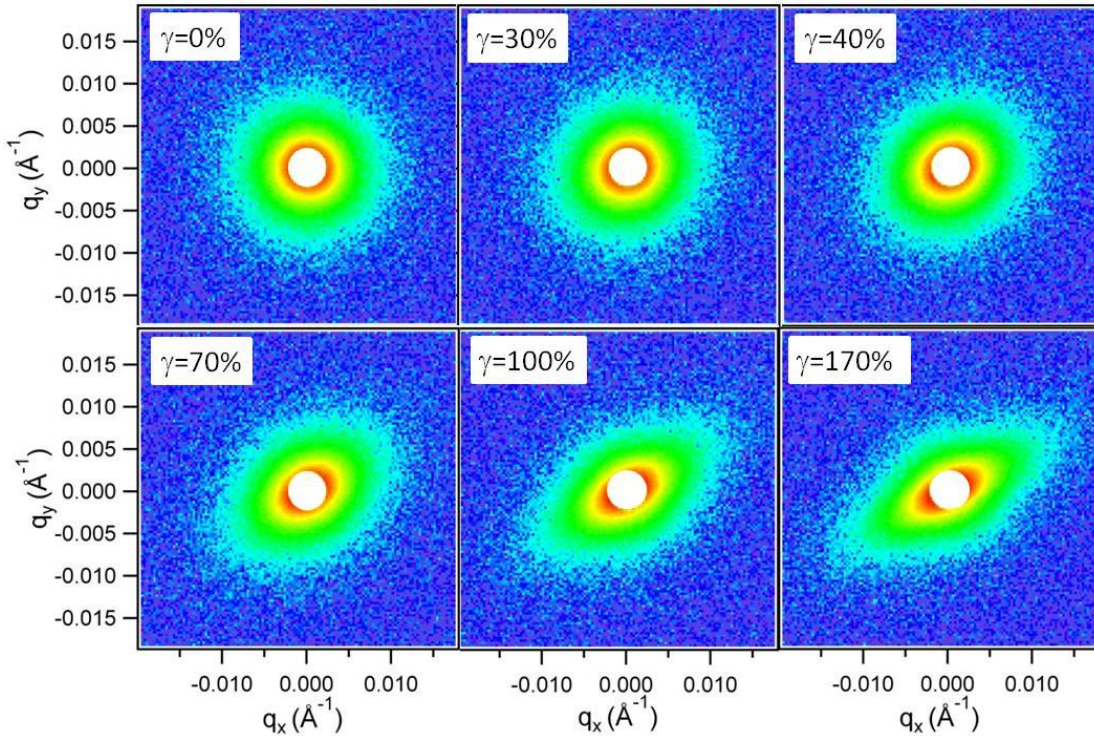


Figure 4.1: Reduced two-dimensional neutron scattering data at various strains highlighting the evolution of fibrin structure with increasing strain.

In order to quantitatively identify the onset of fiber alignment, an annular average intensity is calculated from the 2D scattering data at each strain as a function of the azimuthal angle, $I(\eta)$. This average is performed over a narrow q -range ($0.0045 < q < 0.0054 \text{ \AA}^{-1}$) corresponding to the lowest accessible scattering angles in order to probe the largest possible dimension of the fibers. The annular averages of the scattering intensity at five different strains are shown in Figure 4.2 (left). This plot shows that the intensity is only slightly anisotropic at low strains but becomes increasingly anisotropic at strain values greater than $\gamma = 30\%$.

The mean angle of the fiber alignment (η_0), as illustrated in Figure 4.2 (right), corresponds to the minimum of the scattering intensity as a function of the azimuthal angle and it is directly obtained from the annular average. However, η_0 only becomes meaningful above $\gamma = 30\%$ strain when anisotropy is clearly detectable in the scattering pattern and the angle can be determined with sufficient certainty. The mean fiber orientation angle $\eta_0(\gamma)$ is 34° for γ between 30 and 50%. Above $\gamma = 50\%$, η_0 steadily becomes smaller with increasing strain. Interestingly, the direction of alignment varies only weakly as a function of strain. The difference between the orientation angle when the fibers first begin to align ($\approx 30\%$) and at maximum alignment ($\approx 170\%$) is just 6° .

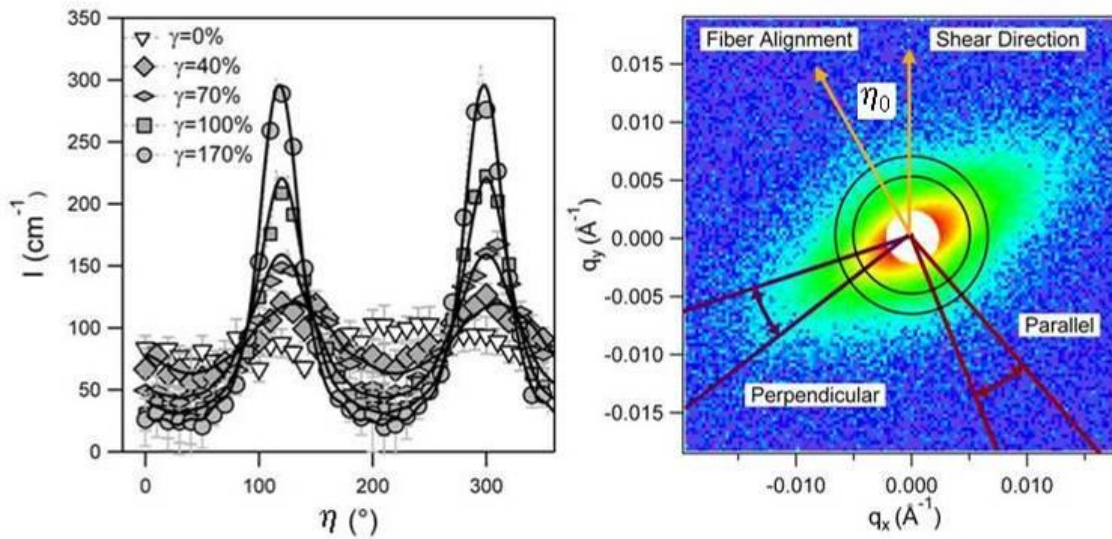


Figure 4.2: Left: Annular intensity averages of 2D scattering profiles for 10 mg/mL fibrin. Lines correspond to the Legendre expansion fits (Equation 4.1). Right: Schematic illustrating the definition of, the annulus over which $I(\eta)$ is calculated, and sectors parallel and perpendicular to the direction of fiber alignment on a scattering plot for a gel strained to 170%. Shear direction refers to the direction of applied strain and corresponds to $\eta=0^\circ$.

In order to further quantify the alignment of the fibers it is necessary to define an orientation distribution function, $F(q, \eta)$. The azimuthally averaged scattering curves are

best fit by a Legendre series expansion, Equation 4.1, as in the paper by Burger et al.²⁹ Due to the nature of even Legendre polynomials, it is necessary to apply a phase shift such that the maximum intensity of $I(\eta^*)$ occurs at $\eta^*=0$.

$$F(q, \eta^*) = \sum_{n=0}^{\infty} a_n P_{2n}(\cos \eta^*) \quad \text{Equation 4.1}$$

where $\eta^* = \eta - \eta_0 + \pi/2$, the values, a_n , are fitting coefficients and the functions, P_{2n} , are even Legendre polynomials. We use the first eight terms of the series to fit all of the angular distributions. The resulting fits for several examples are plotted as solid lines in Figure 4.2 (left).

From $F(q, \eta)$ we determine Hermans' orientation parameter (\bar{P}_2) as a function of strain.^{29, 30} \bar{P}_2 is used to quantify the degree of fiber alignment in the gel and is directly related to the a_1 coefficient from the Legendre expansion.²⁹

$$\bar{P}_2 = \frac{a_1}{5} \quad \text{Equation 4.2}$$

The value of this orientation parameter will vary between zero for random fiber distribution and one for perfectly aligned fibers. The orientation parameter is calculated for all measured strains. It is found to increase from zero when the gel is unstrained to a maximum value of ~0.35 at the peak strain ($\gamma = 170\%$).

The diameter (D) of the fiber is also determined from the scattering data by fitting to a polydisperse cylinder model (Equations 2.20-2.22) as described in Chapter 2. Most of the parameters in these equations can be explicitly defined and held fixed so that only the radius and the scattering length density of the fiber are varied as the model is fit to the data. The scattering length density of the deuterated buffer is calculated based on its

density and composition and found to be $6.3 \times 10^{-6} \text{ \AA}^{-2}$. From Chapter 3 we also know that fibers are only ~19% protein by volume in a 10 mg/mL fibrin gel. The scattering length density of fibrinogen is $3.17 \times 10^{-6} \text{ \AA}^{-2}$, so it follows that the scattering length density of the unstrained fiber is $5.7 \times 10^{-6} \text{ \AA}^{-2}$. The scattering length density of the fibers is allowed to vary over a narrow range from 5.65×10^{-6} to $5.75 \times 10^{-6} \text{ \AA}^{-2}$ to account for small shifts in the scattering intensity that may result from changes in the fiber composition (e.g. fiber dehydration) during deformation.

The volume fraction of fibers in the gel is calculated based on the total protein concentration in the sample (10 mg/mL) and the composition of the fiber. The volume fraction of fibers is found to be 0.037 and is held fixed for all fits. The incoherent scattering background is dependent only on sample composition (not morphology) and is therefore invariable as a function of strain. The background is determined from the flat high- q scattering and is found to be 0.3 cm^{-1} . The mean fiber length is fixed to a large value for all fits (15,000 \AA), which is much larger than the maximum length that can be resolved with this instrument configuration. Therefore, this parameter does not significantly affect the scattering model in this q -region and any variation as a function of strain is indeterminable. Polydispersity factors are also used in fitting to account for the size distributions in fiber radii and length that are expected to occur in the clot. The distribution is defined by a Gaussian function where the polydispersity factor is simply the ratio of one standard deviation to the mean radius. The polydispersity factors for radius and length are held fixed at 0.4 for all fits.

The reduced two-dimensional data and the two-dimensional model fits are shown in Figure 4.3 for three characteristic strains. We also compute and show one-dimensional

scattering curves using radial averages for isotropic profiles and sector-averages for anisotropic profiles. For aligned samples under strain, the sector averages are taken parallel and perpendicular to the fiber alignment direction η_0 using a sector width of 10° .

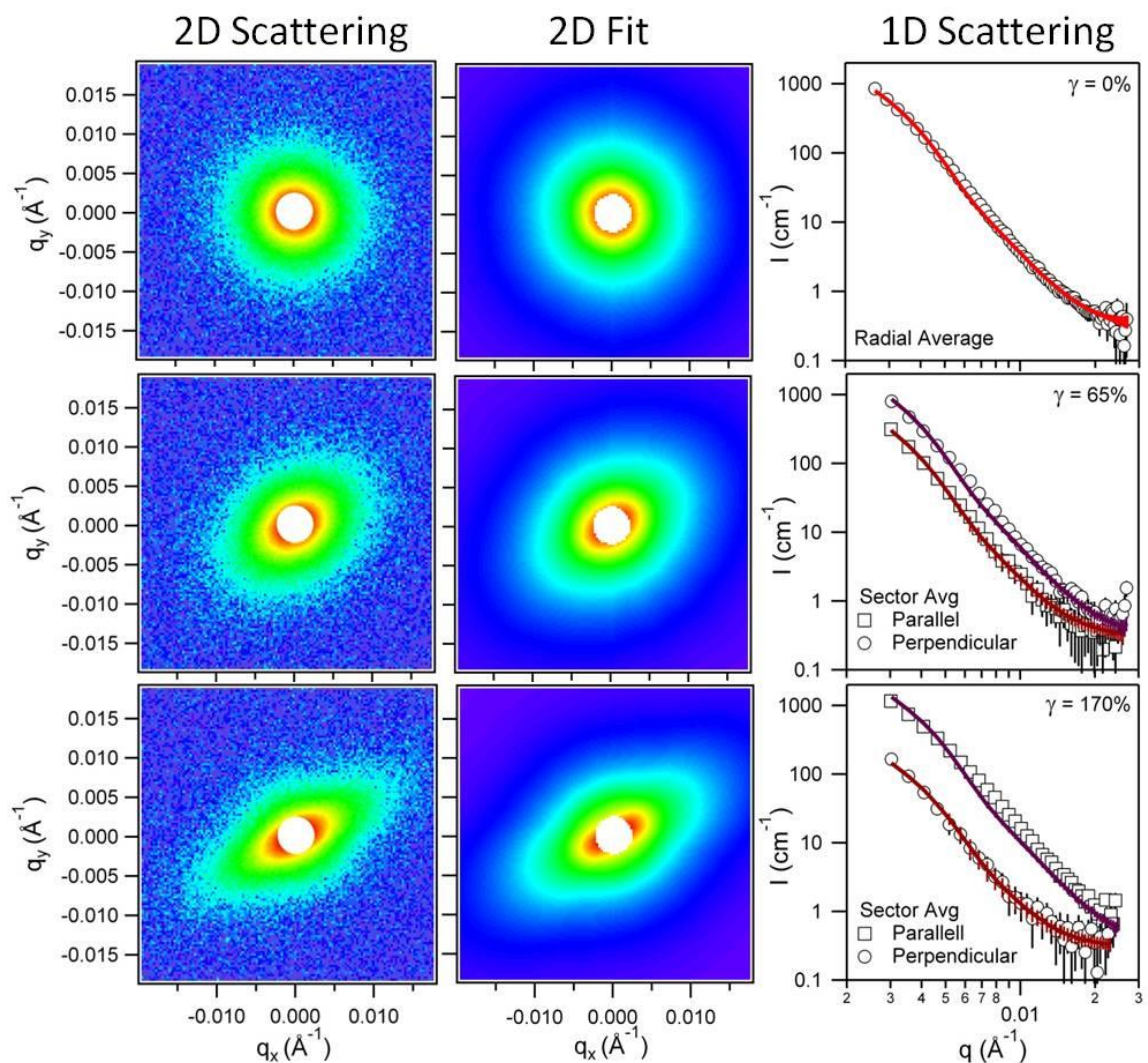


Figure 4.3: Two-dimensional scattering data (left), two-dimensional model fits (center), and one-dimensional scattering and fits (right) in the form of sector averages parallel and perpendicular to η_0 for aligned samples or the radial average for the isotropic sample.

The quality of the fits is very good considering that every pixel in the detector is being taken into account during fitting. There is a very close match between the one-dimensional scattering curves of the data and the model. The scattering length density of

the fiber, which had been allowed to vary during fitting, did not change significantly (<1%) as a function of strain. For the unstrained fibrin clot, we measure a mean diameter of 87 nm that is significantly lower than the values reported in Chapter 3. This is because polydispersity in the diameter was accounted for in the 2D model fitting but not in the simple Guinier analysis that was used in Chapter 3. The cross-sectional Guinier analysis that is used in the previous chapter yields a larger diameter because the scattering signal at low angles is more sensitive to the larger fibers. However, when the same cross-sectional Guinier analysis is applied to the unstrained fibrin sample in this study, the resulting diameter is nearly identical to the previously reported value of $D \sim 120$ nm.⁷ Therefore, the structure of the sample has not changed and is comparable to that reported in our previous work. From the fits, we determine that the diameter remains constant until the onset of fiber alignment. At that point, it decreases steadily from 87 nm to 75 nm (14% shrinkage) at the maximum measured strain ($\gamma = 170\%$).

Using identical sample compositions and polymerization conditions, the instantaneous gel modulus (G_{Inst}) is also determined by taking the derivative of the stress as a function of the strain ($d\sigma/d\gamma$) in a separate rheological experiment. The stress and strain are experimentally determined from an applied shear stress ramp using a cone and plate geometry in a stress-controlled rheometer. The modulus is plotted in Figure 4.4 as a function of strain. Several key mechanical transitions occur as the gel is strained to $\gamma \sim 30\%$. Even in the low-strain region ($\gamma < 10\%$), the sample undergoes a significant amount of strain-hardening. In this domain, the modulus increases steadily from a rest value of $G_{Inst} = 2,300$ Pa to a local maximum of $G_{Inst} = 3,400$ Pa at $\gamma = 10\%$. Interestingly, between $\gamma = 10$ and 30% the modulus decreases again to a local minimum of $G_{Inst} = 3,000$

Pa. The scattering data reveals that the average fiber diameter remains relatively unchanged throughout this entire region and that there is no significant fiber alignment (Figure 4.4). However, beyond this critical point ($\gamma \sim 30\%$), the average fiber diameter starts to decrease steadily with increasing strain and the fibers begin to align substantially. Note that there is still a clear but small increase in the order parameter at strains less than $\gamma = 30\%$, but the increase in the order parameter occurs much faster once this critical strain has been reached. Finally, a second onset of strain-hardening occurs beyond this critical deformation and there is a clear correlation between the onsets of fiber alignment, fiber shrinkage, and strain-hardening. The results presented herein are

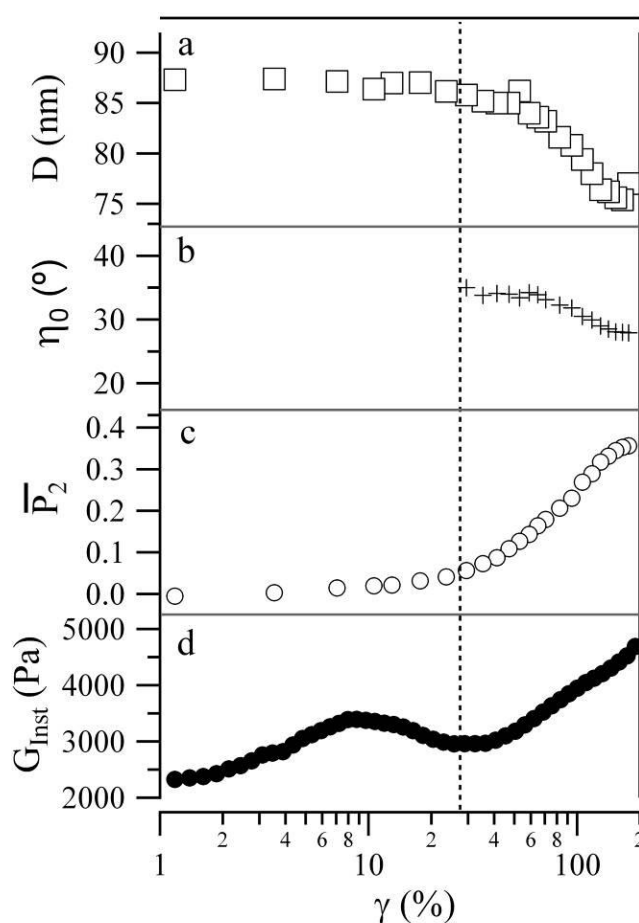


Figure 4.4: Fiber diameter (a), fiber alignment angle (b), Herman orientation parameter (c) and instantaneous modulus (d) as a function of applied strain.

characteristic of 10 mg/mL fibrin gels prepared as detailed in the methods section, with almost no variation in the shape of the instantaneous modulus curve; however, there is slight variation in the magnitude of the instantaneous modulus ($\pm\sim 15\%$) between samples that is expected as a result of sample inhomogeneity. The instantaneous modulus of two gels plotted in Figure 4.5 demonstrates the reproducibility of the reported rheological behavior.

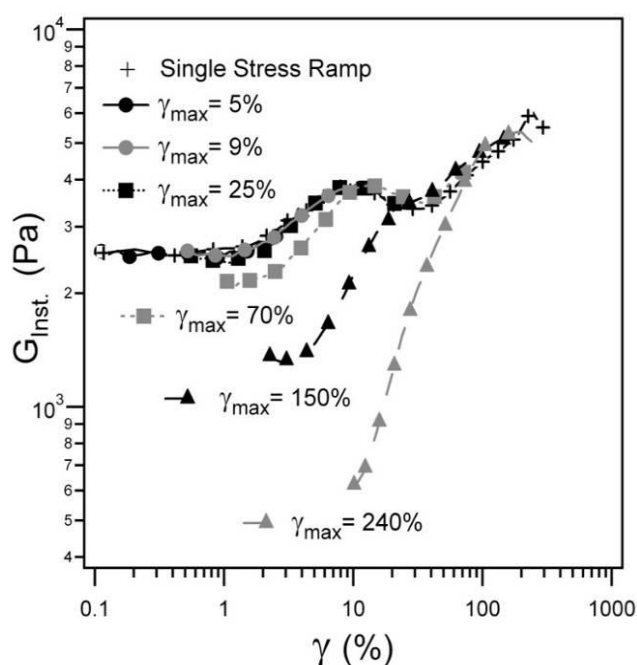


Figure 4.5: Instantaneous moduli (G_{Inst}) of a 10 mg/mL fibrin gel obtained from sequential shear stress ramps with increasing maximum strain γ_{max} values (\bullet 5%, \circ 9%, \blacksquare 25%, \square 70%, \blacktriangle 150%) until the gel is broken (\blacktriangle). The instantaneous modulus of a second gel (+), using a single stress ramp until failure, is also shown for comparison.

At this point, the SANS results cannot fully explain the strain dependent behavior of fibrin gels at strains lower than $\gamma = 30\%$ because there are no measurable changes in the scattering patterns and no structural transitions can be perceived. Still, the instantaneous modulus of a 10 mg/mL gel shows significant strain dependence between $\gamma = 1$ and 30%. In this region the sample shows a strain-hardening response that is followed

by strain-softening. An additional rheological experiment is also performed to further elucidate the nature of the structural changes that occur at low strains ($\gamma < 30\%$). This experiment is based on an examination of the mechanical reversibility of a fibrin gel after sequential strain profiles that are carried out to increasing values of the maximum strain. Several maximum strain values (γ_{max}) are selected corresponding to the regions where key features are observed in the instantaneous modulus curve ($G_{Inst}(\gamma)$). The gels are gradually strained to each limiting value before the deformation is reversed and the process is repeated to a larger strain level. The instantaneous moduli calculated from the stress-strain ramps for these experiments are plotted in Figure 4.5.

The instantaneous modulus curves for a gel that is sequentially strained to $\gamma_{max} = 5, 9$ and 25% overlap perfectly. However, on the subsequent strain ramp the instantaneous modulus no longer agrees with the previous cycles measurement at low strain, indicating that the gel was irreversibly damaged during the strain ramp to $\gamma_{max} = 25\%$. Therefore, the limit of reversible deformation must lie between $\gamma = 9$ and 25% . This is beyond the first strain-hardening regime and suggests that it is only within this region that the deformation is completely reversible. The onset of irreversible deformation must be close to the strain softening and second strain-hardening region of the gel. As the peak strain (γ_{max}) increases, the rheology deviates significantly more from the initial test. This indicates that the gel is experiencing ongoing degradation as it is strained to larger and larger levels.

Discussion

Low Strain Regime ($\gamma < 10\%$)

Fibrin gels have a linear response to deformation only at very small strains ($\gamma < 1\%$). At strains greater than 1% the gel begins to exhibit a non-linear mechanical response that is indicated by an increasing modulus. For moderately low deformation, from $1\% < \gamma < 10\%$, the gel can be best described as weakly strain-hardening. That is, the modulus of the gel increases steadily with increasing strain. Furthermore, in the limit of low strains, the deformation of a fibrin gel is fully reversible as shown in Figure 4.5. This suggests that no permanent structural damage is done to the gel when it is strained to relatively low magnitudes. Despite the nearly 50% increase in modulus between $\gamma = 1\%$ and $\gamma = 10\%$, the neutron scattering signal remains unchanged at strains of this magnitude. This demonstrates that key structural features of the gel, including fiber diameter and alignment, remain unchanged throughout the first strain-hardening regime. The structure of the gel at low strain is described schematically in Figure 4.6.

Of the major theories postulated for explaining strain-hardening in biopolymer gels, it is clear that the bending and stretching model originally proposed by Onck et.al. requires significant deformation and alignment of fibers.¹⁹ The absence of alignment in the low strain regime indicates that the bending and stretching model is not an accurate representation of strain-hardening in this gel under small deformation. Conversely, strain-hardening as a result of a reduction in fiber thermal fluctuations will not necessarily have a signature that is detectable with small angle neutron scattering. The absence of structural changes corresponding to the first strain-hardening regime suggests that the

entropic model is likely the more applicable model for explaining the strain-hardening that is observed in coarse fibrin gels under small deformation. Therefore, even in relatively coarse fibrin gels, fiber flexibility cannot be fully neglected. A recent report suggests that entropic elasticity can also occur within individual fibers as a result of lateral fluctuations of the polypeptide chains that facilitate crosslink formation.² Additionally, the sensitivity of scattering techniques is biased toward larger structures, and the reported average radius reflects a distribution of fiber sizes that includes small fibers, which are expected to undergo entropic lateral fluctuations.

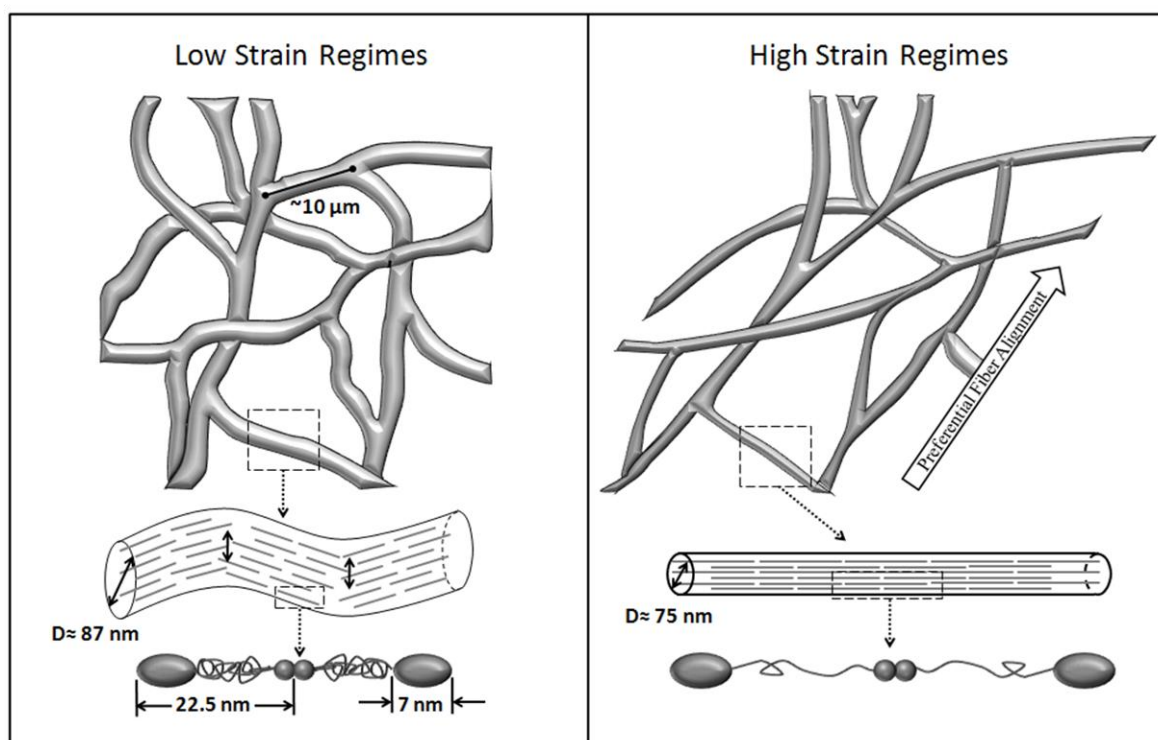


Figure 4.6: Schematic description of the various regions that describe the strain-hardening response of fibrin under different levels of deformation.

Intermediate Strain Regime ($\gamma = 10\text{-}30\%$)

At intermediate strains ($\gamma = 10\text{-}30\%$) there is a strain-softening regime that separates the two distinct strain-hardening domains. This does not seem to correspond to any significant structural change detectable with neutron scattering over the probed q -range. However, this region does correspond very well with the onset of irreversible deformation (Figure 4.5). The fibrin gel is first damaged as it is strained to $\gamma_{max}=25\%$, as evidenced by a reduction in the initial instantaneous modulus measured during subsequent deformation cycles. The onset of irreversible deformation, therefore, occurs between 10 and 25% strain. The separation of two strain-hardening regimes by a plateau in the gel modulus was recently reported in the literature.^{2, 7} In Chapter 3, we noted that increasing the concentration of fibrin in the gel gradually leads to the development of the strain-softening regime that is also observed in the 10 mg/mL gel used in this work.⁷ The plateau observed in experiments with 8 mg/mL fibrin samples by other groups is also consistent with this transition.² However, they report that the fibrin gel exhibits fully reversible rheology. In contrast, our results indicate that, in a 10 mg/mL coarse fibrin gel, the deformation is irreversible when the gel is strained beyond the intermediate plateau. In another recent report it was stated that the individual proteins must begin to unfold before the gel is strained above $\gamma = 15\%$ in order to account for the high extensibility of the fibrin gel.³ This transition is also consistent with the onset of irreversible deformation observed in our study. We expect that the onset of protein unfolding will induce a transition from fully reversible deformation to irreversible deformation as the unfolding of the proteins could irreversibly damage the internal structure of the fibers and

protofibrils. Furthermore, several researchers have linked the uncoiling of alpha helices to the softening and subsequent stiffening of individual protein based fibers.^{23, 24}

To the best of our knowledge none of the previously discussed models is able to predict the intermediate strain-softening behavior that is observed in fibrin gels at high concentrations. Interestingly, a reversible stress-softening response in actin gels was also recently reported.²² It is postulated that buckling of fibers under compression can lead to a reduction in the number of load-bearing fibers and in an overall reduction in the gel stiffness. This is another plausible mechanism to explain the intermediate strain-softening of fibrin, so further exploration is necessary to fully confirm the origin of this feature.

High Strain Regime ($\gamma > 30\%$)

It has been previously suggested that fibrin gels consisting of coarse stiff fibers are better represented by the bending and stretching model.¹¹ Neutron scattering, as used in this study, is especially suited for testing the validity of models where strain-hardening results from a transition between fiber bending and stretching regimes because they require significant network reorganization. These structural transitions would necessarily result in the alignment of fibrin fibers towards the direction of the applied strain. The progressive alignment of the fibers manifests itself in the neutron scattering measurement as the development of anisotropy, yielding radially-asymmetric scattering patterns. It is evident from Figures 4.1-4.4 that the fibers do align “macroscopically”, as predicted, but only after a threshold strain of $\gamma \sim 30\%$ has been reached. This corresponds well with the onset of the second strain-hardening regime and with the reduction in the average fiber diameter that is shown in Figure 4.4.

Recently, it was demonstrated that the application of sufficient stress to coarse fibrin fibers can lead to protein unfolding and the extension of the length of the individual proteins in the fibers.³ Furthermore, the exposure of hydrophobic residues results in additional bundling of the extended regions and in a net reduction of the average fiber diameter. Our study clearly demonstrates a reduction in fiber diameter that can be attributed to protofibril bundling and also shows that the threshold for bundling occurs simultaneously with the onset of fiber alignment and with the second onset of strain-hardening. The observed fiber alignment and shrinkage is consistent with earlier results.³ It was previously reported that the fibers begin to align under extensional deformation prior to $\gamma = 50\%$.³ In the same study the overall reduction in the fiber diameter that is reported varied from 185 nm at rest, to 74 nm at the maximum deformation before failure ($\gamma \approx 270\%$). This represents a 250% decrease in fiber diameter upon stretching. In our study, the fibers undergo gradual reduction from 87 to 75 nm that represents a much smaller change of $\sim 14\%$ with respect to the original diameter. The differences in the extent of shrinkage could be partially attributed to a smaller degree of deformation since our study was limited to strains below 200%. This difference could also result from structural changes that are caused by variation in the buffer composition, or changes in the extent of covalent ligation via Factor XIIIa. The structural changes that occur in the high strain regime are also illustrated in Figure 4.6.

The 10 mg/mL coarse fibrin gels examined in this study have two separate strain-hardening regimes, with distinct structural signatures, that are clearly separated by an intermediate reduction of the modulus. These results demonstrate that these gels cannot be solely described with either of the two primary theories for strain-hardening. At low

deformations, these gels likely undergo strain-hardening due to a reduction in lateral thermal fluctuations (entropic elasticity).¹⁰ In addition, at larger deformations, the same gels will strain-harden due to a transition from bending-dominated to stretching-dominated mechanical responses.¹⁹ It has also been suggested that, in polydisperse gels containing both fine and coarse fibers, the smaller fibers can exhibit entropic strain-hardening while the response of large fibers is described by bending and stretching models.¹¹ We propose that it is also possible that both theories are applicable at different levels of deformation. For example, the straightening of individual fibers would likely precede any bending and stretching response. It must be noted that the two models for strain-hardening are not mutually exclusive because they originate from different physical effects.

References

1. J. P. Collet, H. Shuman, R. E. Ledger, S. T. Lee and J. W. Weisel, *Proc. Natl. Acad. Sci. U. S. A.*, 2005, **102**, 9133-9137.
2. I. K. Piechocka, R. G. Bacabac, M. Potters, F. C. MacKintosh and G. H. Koenderink, *Biophys. J.*, 2010, **98**, 2281-2289.
3. A. E. X. Brown, R. I. Litvinov, D. E. Discher, P. K. Purohit and J. W. Weisel, *Science*, 2009, **325**, 741-744.
4. A. E. X. Brown, R. I. Litvinov, D. E. Discher and J. W. Weisel, *Biophysical Society*, 2007, pp. 524A-524A.
5. F. C. Mackintosh, J. Kas and P. A. Janmey, *Phys. Rev. Lett.*, 1995, **75**, 4425-4428.
6. E. A. Ryan, L. F. Mockros, J. W. Weisel and L. Lorand, *Biophysical Journal*, 1999, **77**, 2813-2826.
7. K. M. Weigandt, D. C. Pozzo and L. Porcar, *Soft Matter*, 2009, **5**, 4321-4330.
8. P. R. Onck, T. Koeman, T. van Dillen and E. van der Giessen, *Phys. Rev. Lett.*, 2005, **95**.
9. T. van Dillen, P. R. Onck and E. Van der Giessen, *Journal of the Mechanics and Physics of Solids*, 2008, **56**, 2240-2264.
10. C. Storm, J. J. Pastore, F. C. MacKintosh, T. C. Lubensky and P. A. Janmey, *Nature*, 2005, **435**, 191-194.
11. H. Kang, Q. Wen, P. A. Janmey, J. X. Tang, E. Conti and F. C. MacKintosh, *Journal of Physical Chemistry B*, 2009, **113**, 3799-3805.

12. D. C. Lin, J. F. Douglas and F. Horkay, *Soft Matter*, 2010, **6**, 3548-3561.
13. A. V. Dobrynin and J. M. Y. Carrillo, *Macromolecules*, 2011, **44**, 140-146.
14. C. P. Broedersz, K. E. Kasza, L. M. Jawerth, S. Munster, D. A. Weitz and F. C. MacKintosh, *Soft Matter*, 2010, **6**, 4120-4127.
15. M. Guthold, W. Liu, E. A. Sparks, L. M. Jawerth, L. Peng, M. Falvo, R. Superfine, R. R. Hantgan and S. T. Lord, *Cell Biochemistry and Biophysics*, 2007, **49**, 165-181.
16. W. Liu, R. Hantgan, J. Mullin, S. Lord, R. Superfine, R. Taylor and M. Guthold, *Biophys. J.*, 2004, **86**, 477A-477A.
17. S. Anand and S. L. Diamond, *Circulation*, 1996, **94**, 763-774.
18. Q. Wen, A. Basu, J. P. Winer, A. Yodh and P. A. Janmey, *New Journal of Physics*, 2007, **9**.
19. P. R. Onck, T. Koeman, T. van Dillen and E. van der Giessen, *Phys. Rev. Lett.*, 2005, **95**, 4.
20. N. E. Hudson, J. R. Houser, E. T. O'Brien, R. M. Taylor, R. Superfine, S. T. Lord and M. R. Falvo, *Biophys. J.*, 2010, **98**, 1632-1640.
21. K. A. Erk, K. J. Henderson and K. R. Shull, *Biomacromolecules*, 2010, **11**, 1358-1363.
22. O. Chaudhuri, S. H. Parekh and D. A. Fletcher, *Nature*, 2007, **445**, 295-298.
23. Z. Qin, L. Kreplak and M. J. Buehler, *PLoS One*, 2009, **4**, 14.
24. A. Miserez, S. ScottWasko, C. F. Carpenter and J. H. Waite, *Nature Materials*, 2009, **8**, 910-916.
25. J. R. Houser, N. E. Hudson, L. F. Ping, T. O'Brien, R. Superfine, S. T. Lord and M. R. Falvo, *Biophysical Journal*, 2010, **99**, 3038-3047.
26. M. W. Liberatore, F. Nettesheim, N. J. Wagner and L. Porcar, *Physical Review E*, 2006, **73**, 4.
27. J. J. Pisano, Finlayso.Js and M. P. Peyton, *Science*, 1968, **160**, 892-&.
28. S. R. Kline, *Journal of Applied Crystallography*, 2006, **39**, 895-900.
29. C. Burger, B. S. Hsiao and B. Chu, *Polymer Reviews*, 2010, **50**, 91-111.
30. J. J. Hermans, P. H. Hermans, D. Vermaas and A. Weidinger, *Recl. Trav. Chim. Pays-Bas-J. Roy. Neth. Chem. Soc.*, 1946, **65**, 427-447.

Chapter 5

Alterations in Fibrin Clot Structure and Mechanics Attributed to Specific Oxidation of Methionine Residues in Fibrinogen

Introduction

Fibrinogen is a 340 kDa plasma protein and the precursor to fibrin, which is the primary structural component of blood clots and critical to haemostasis after injury.¹ In healthy individuals fibrinogen is present in blood at concentrations of 2-4 mg/mL. Upon injury a series of biochemical processes occur that result in the local release and activation of thrombin. This enzyme cleaves two short peptide sequences, fibrinopeptides A and B, from fibrinogen and converts it to fibrin. The removal of these polypeptides exposes binding sites and drives the self-assembly of fibrin molecules into a half-staggered two-stranded array termed a protofibril. Fibrinogen has two α C domains that normally self-associate with the central domain of the monomer. Upon conversion to fibrin, the α C domains dissociate and are thought to play a role in the lateral aggregation

of protofibrils leading to the formation of coarse fibers.^{2, 3} However, the extent of lateral aggregation is also affected by solution conditions and by modifications to the fibrinogen monomer.^{2, 3}

Many disease states are associated with abnormal fibrin clot structure. Blood clots formed in thrombotic diseases such as, ischemic stroke, diabetes, and renal impairment tend to have thin fibrin fibers, reduced clot porosity, and delayed fibrinolysis relative to healthy patients.⁴⁻⁶ However, the mechanisms underlying these structural changes during disease remain unknown. Heterogeneous fibrin clot formation can be the result of genetic or biochemical modifications that may occur during protein formation or subsequently during circulation. Known modifications to fibrinogen include degradation of the carboxy terminal groups of the αA and γ chains, glycation of lysine residues in diabetes patients and partial oxidation of methionine residues, each of which can impact polymerization.⁷ By gaining a better understanding of the impact of molecular changes associated with disease-induced coagulopathies, it may be possible to develop medical intervention strategies that prevent complications related to altered coagulation.

Fibrinogen is more susceptible to oxidation than most other plasma proteins and several coagulation factors, including fibrinogen, are sensitive to hypochlorite oxidation.^{8, 9} Hypochlorous acid is generated *in vivo* locally at sites of injury, infection or inflammation as part of the natural immune response.¹⁰ Neutrophils, a type of white blood cell, produce high local concentrations of hypochlorous acid *in vivo* through the reaction of hydrogen peroxide and Cl^- via the enzyme myeloperoxidase.¹¹ Hypochlorous acid oxidizes methionine to form methionine sulphoxide with a high 2nd order rate constant (k) of $3.8 \times 10^7 M^{-1} s^{-1}$ so that this reaction occurs preferentially over the oxidation

of most other amino acids.¹² Methionine oxidation by hypochlorous acid has been shown to inhibit important regulatory coagulation proteins including activated protein C and thrombomodulin.^{13, 14} In these cases the deactivation of these proteins has been traced to the oxidation of individual methionine residues. In fibrinogen, oxidation with hypochlorous acid has been shown to reduce lateral aggregation and to trigger altered lysis behavior in fibrin clots.¹⁵ Other studies have demonstrated that restricting lateral aggregation, which promotes the formation of dense fibrous gels, is linked to delayed clot lysis due to impaired diffusion of plasmin through smaller pores.^{5, 16}

In this chapter, we examine the effect of oxidation with hypochlorous acid on the structural, mechanical, and lytic properties of fibrin gels. A combination of small angle x-ray scattering (SAXS) and scanning electron microscopy (SEM) is used to characterize the structure of the fibrin gels. Shear rheology is utilized to measure the linear and non-linear bulk rheological properties of fully formed fibrin gels and to track the dissolution of gels during tissue plasminogen activator (tPA) and plasminogen induced clot lysis. The results of this work are discussed with respect to several studies that link conformational changes in the α -C domain to the inhibition of lateral aggregation in fibrin clots. From this discussion a specific biochemical mechanism for the inhibition of lateral aggregation via hypochlorite oxidation is proposed.

Materials and Methods

Sample Preparation

Human fibrinogen (plasminogen and von Willebrand depleted) and human- α -thrombin are purchased from Enzyme Research Laboratories in South Bend, Indiana. The

fibrinogen is defrosted to 37°C and dialyzed to achieve a 99.9% exchange into a buffer solution of 0.14 M NaCl and 44 mM Hepes titrated to pH 7.4 in deionized-H₂O. The fibrinogen solution is filtered through 0.45 µm PVDF filters and the concentration is determined with UV-VIS spectroscopy at $\lambda=280$ nm with an extinction coefficient of 1.6 mg mL⁻¹ cm⁻¹.¹⁷

The fibrinogen is oxidized with 50 or 150 µmol HOCl/g fibrinogen and incubated for one hour at 37°C. The oxidation reaction is quenched with a 10x molar excess of L-methionine. The non-oxidized sample is made to have the same composition as the 50 µmol sample by adding pre-quenched HOCl and methionine. After oxidation the samples are separated into aliquots and stored at -80°C. The gels are prepared by adding CaCl₂ and thrombin to activate factor XIII and to convert fibrinogen to fibrin. Unless otherwise stated, the final sample composition is 1-10 mg/mL fibrinogen, 0.16 NIH U/mL thrombin, 0.14 M NaCl, 44 mM Hepes and 2 mM CaCl₂ in deionized water at pH 7.4.

Liquid Chromatography-Mass Spectrometry (LC-MS)

Methionine oxidation is analyzed by collaborators Yi Wang and Xiaoyun Fu at the Puget Sound Blood Center Research Institute with nanoLC-MS.¹⁸ The fibrinogen is reduced with dithiothreitol, alkylated with iodoacetamide, and digested with trypsin in buffer containing 50 mM ammonium bicarbonate, 5 mM L-methionine, and 5% acetonitrile overnight at 37°C. The tryptic peptides are concentrated and desalted with C18 extraction cartridges (3M Empore), dried under vacuum, and then resuspended in the solvent containing 0.1% formic acid, 5 mM L-methionine, and 5% acetonitrile. The tryptic peptides from 200 ng protein were injected for each nanoLC-MS analysis. NanoLC-MS analyses are performed in the positive ion mode with a Thermo-Finnigan

LTQ linear ion trap mass spectrometer (San Jose, CA) coupled to a Waters nanoAcquity UltraPerformance LC (UPLC) system (Milford, MA). Peptides are separated at a flow rate of 0.3 $\mu\text{L}/\text{min}$ on a nanoUPLC BEH130 C18 column (100×0.075 mm, 1.7 μm , Waters), using 0.1% formic acid in water (Solvent A) and 0.1% formic acid in CH_3CN (Solvent B). Peptides are eluted using a linear gradient of 5%–35% solvent B over 90 min. The spray voltage is 2.0 kV, and the temperature of the heated capillary is 200°C. The collision energy for MS/MS was 35%. Methionine oxidation is determined by peak area from the reconstructed ion chromatograms of nonoxidized and oxidized methionine-containing peptides.

Circular Dichroism

Circular dichroism spectroscopy measurements are performed to determine whether significant alteration of the secondary structure occurs as a result of HOCl oxidation. Fibrinogen is prepared by dialyzing the buffered protein solution to remove salts, which interfere with the measurements. Circular dichroism spectra are obtained for 0.075 mg/mL fibrinogen in DI- H_2O with a Jasco 720 Circular Dichroism Spectrophotometer operated at 25°C.

UV-Vis Spectroscopy

UV-VIS spectroscopy measurements are made on an Evolution 300 Thermo Scientific UV-visible spectrophotometer. Spectra over $320 < \lambda < 780$ nm are taken in a 1 cm path length cell once per minute for one hour to capture gelation kinetics.

Scanning Electron Microscopy

All SEM images are obtained using an FEI Technai SEM with a 5 kV accelerating voltage. The samples are prepared from 1 mg/mL fibrin gels and gelation is allowed to proceed for 1 hour. The gel is rinsed three times with DI-H₂O to extract excess salt. The gels are frozen at -80°C and lyophilized to preserve the structure. The samples are sputtered with a 5 nm thick layer of gold with an SPI sputter coater.

Small Angle Neutron Scattering

Non-oxidized and 150 HOCl oxidized fibrin gels were formed in 4 mm pathlength demountable SANS with one of the quartz windows removed. The samples were prepared in the 0.14 M NaCl, 0.044 M HEPES and 2 mM CaCl₂ buffer (pH 7.4) with 6.5 mg/mL fibrinogen and 0.16 NIH u/mL thrombin. Gelation was allowed to proceed for 1 hour prior to additional processing. After gelation the buffer was exchanged with a deuterated buffer of identical composition such that the gel contained ~96% D₂O. The solvent exchange is required in order to reduce the incoherent background scattering such that high- q scattering features can be resolved.

Small angle neutron scattering (SANS) and ultra small angle neutron scattering (USANS) measurements are performed on the same samples at the Center for Neutron Research at NIST in Gaithersburg, Maryland. SANS measurements are performed on the NG3 30 meter instrument.¹⁹ Measurements are made at three detector distances to cover a broad q -range (0.002 to 0.3 Å⁻¹) using neutron wavelengths of 5.5 Å and 8.4 Å. The SANS data are corrected for background and sample cell scattering, and is placed on an absolute scale by measuring the direct beam flux.²⁰ Data is reduced and desmeared using the NIST Igor based software.²⁰

Rheology

Rheology measurements are performed on a stress-controlled Anton Paar MCR 301 rheometer with either a cone and plate configuration (25 mm diameter and 1° angle) or a concentric cylinder configuration (16.6 mm diameter × 25 mm length and 0.71 mm gap). The temperature is maintained at 37°C with a Peltier heat exchanger. Evaporation is prevented by the application of an immiscible oil layer to the exposed surface.

Gelation is monitored with 0.5% strain oscillations at one Hz for one hour. Frequency sweeps are performed over 0.0005 ω <math>< 50</math> Hz at 0.5% strain. To measure the non-linear rheology the shear stress (τ) is gradually increased from 0.001 Pa to an instrument limited maximum stress or until the gel breaks. During the stress ramp, the strain is measured at discrete stress intervals that are logarithmically spaced.

Lysis experiments are monitored rheologically on the cone and plate using 0.5% strain oscillations at 1 Hz. The samples contain 2.2 mg/mL fibrinogen and 5 μ g/mL plasminogen in the standard buffer. Thrombin is added at 1.0 NIH u/mL to initiate gelation and 0.5 μ g/mL tPA is added to convert plasminogen to plasmin and initiate clot lysis. Both gelation and fibrinolysis are initiated simultaneously. However, the tPA and plasminogen are added at much lower concentration to ensure that a strong gel is formed before significant fibrinolysis occurs.

tPA Activation Assay

A tPA activation assay was performed by collaborators White and Chung. The activation of plasminogen by tPA on immobilized baseline and oxidized (50 μ M HOCl) fibrinogen is assayed as described by Sauls et al.²¹ The control and oxidized fibrinogens are immobilized and/or converted to fibrin with 10 nM thrombin. After immobilization,

washing, and blocking, 100 μL of a mixture of 1 nM tPA, 5 $\mu\text{g}/\text{mL}$ of plasminogen, and 0.1 mM Spectrozyme PCa (American Diagnostica) is added and the plasmin activation is monitored by absorbance of the Spectrozyme cleavage product at 405 nm at room temperature. The maximal velocity of plasmin generation is then calculated as the steepest slope of the absorbance curve. The ratio of the maximal rates of substrate cleavage between control and oxidized fibrinogen/fibrin are compared.

Results

Fibrinogen Oxidation

Fibrinogen was oxidized by adding HOCl at physiologically relevant concentrations between 0-150 μmol HOCl/g fibrinogen (or \sim 0-300 μM based on 2 mg/mL fibrinogen concentration).²² The extent of oxidation for several methionine residues was determined with nanoLC-MS by collaborators at the Puget Sound Blood Center Research Institute and the results of this analysis are presented in Table 5.1.

Table 5.1: Oxidized fraction of selected methionine residues by HOCl with 0, 50, and 150 μM HOCl/g fibrinogen

	γ -78	α -91	α -476	β -190	β -305	β -367
0 HOCl	0.008	0.007	0.024	0.014	0.028	0.013
50 HOCl	0.112	0.010	0.256	0.052	0.043	0.137
150 HOCl	0.334	0.022	0.727	0.109	0.148	0.431

In this table, the oxidized fraction of each selected methionine residue is listed. In all cases, the addition of HOCl led to an increase in oxidation relative to the native fibrinogen. Three of the analyzed methionine residues γ -78, β -367 and α -476, appear to be preferentially oxidized (>10% oxidation in the 50 HOCl fibrinogen and >30%

oxidation in the 150 HOCl fibrinogen) over the remaining methionine residues. In Figure 5.1, the fibrinogen crystal structure is presented with all of the methionine residues circled and the highly oxidized residues labeled.^{23, 24} Though the crystal structure of the α -C domain has not yet been fully characterized, the structure of the N-terminal subdomain has been determined with a combination of circular dichroism and NMR.²⁴ The α -C domain is included in Figure 5.1 schematically with dotted lines and the structure of the N-terminal subdomain is highlighted with the highly oxidized α -476 methionine labeled.

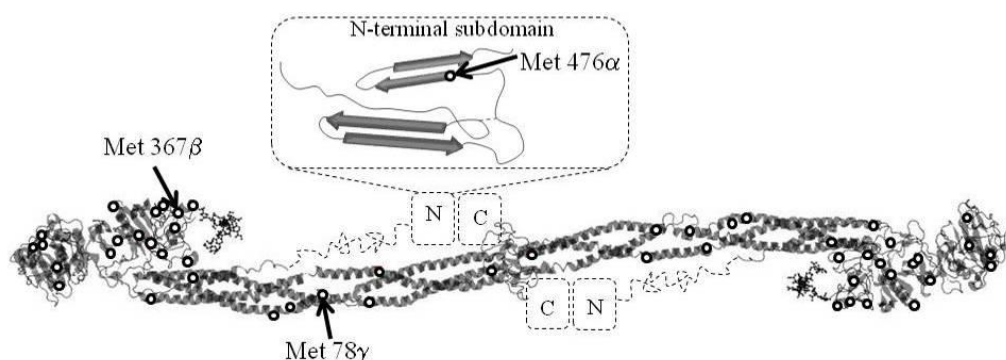


Figure 5.1: Fibrinogen molecule with all methionine residues circled and highly oxidized methionine residues labeled. The crystal structure was rendered from the protein data bank.^{23, 24} The α -C domain was added schematically with dotted lines, including the ordered N and C terminal subdomains.²³

Circular dichroism measurements were used to examine the effect that HOCl oxidation has on the secondary structure of fibrinogen. The circular dichroism spectrum as a function of wavelength for each of the 0, 50, and 150 HOCl fibrinogens is plotted in Figure 5.2. There are no significant changes in the spectra with oxidation, indicating the secondary structure is generally maintained upon oxidation.

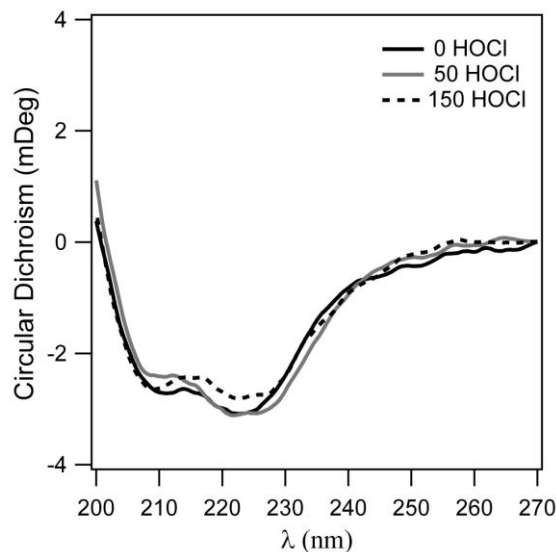


Figure 5.2: Circular dichroism spectra from 0, 50, and 150 HOCl fibrinogen at 0.075 mg/mL in water.

UV-Vis Spectroscopy

Fibrin gels were formed by adding thrombin to the prepared fibrinogen samples at all three levels of oxidation. Calcium (2 mM) was added to all solutions to activate Factor XIII and promote covalent ligation. A photograph of three 2 mg/mL fibrin gels at increasing levels of methionine oxidation is presented in Figure 5.3 (left). In the photo a series of black lines are placed behind the vials to gauge the relative turbidity of the gels. To quantify the turbidity during gelation the absorbance at $\lambda=350$ nm of 1 mg/mL fibrin gels was measured as a function of time and plotted in Figure 5.3 (right). We find that the gelation time is unchanged with oxidation, which suggests that oxidation does not affect the gelation kinetics. As in the photograph, however, the turbidity of the gels is highly influenced by oxidation, with the non-oxidized fibrin forming very opaque gels and the highly-oxidized fibrin forming nearly transparent gels. The turbidity of fibrin gels has long been linked to fiber diameter with fine fibers producing clear gels.¹⁷

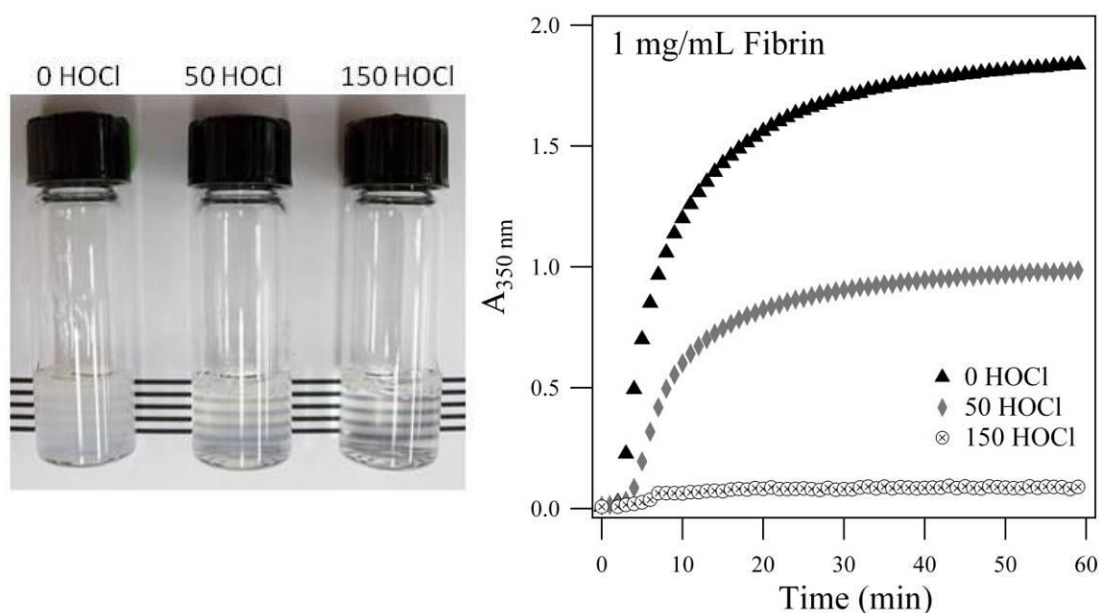


Figure 5.3: Left: Photograph of 2 mg/mL fibrin gel at increasing levels of oxidation. Right: Absorbance at 350 nm for 1 mg/mL fibrin gels plotted as a function of time during gelation.

To ensure that the decreasing turbidity was caused by a reduction in fiber size it is necessary to demonstrate that these changes are not attributable to inactive fibrinogen. A controlled volume of buffer was added to the top of a fully formed gel. After approximately 24 hours, the fibrinogen concentration in the tops was measured. It was found that the baseline gel contained less than 10% inactive fibrin. The concentration of unreacted fibrin in the oxidized gels was unmeasurable indicating that nearly all of it was activated and formed part of the clot.

Gel Structure

Given the physiological importance of fibrin gels and the existence of structure driven coagulopathy, characterizing the structure of fibrin gels has been the subject of many studies.^{1, 17, 23, 26, 27} Various microscopy and scattering techniques have been utilized to examine the structure of fibrin clots including SEM, scanning probe

microscopy, optical microscopy, small angle neutron scattering, small angle x-ray scattering, and turbidity analysis. In this study, the structure of the oxidized and untreated fibrin gels is characterized using a combination of SEM and SAXS. Both of these techniques have various advantages and disadvantages. SEM requires several post processing steps including drying and gold sputtering that could impact the imaged structure. In SAXS, the experiment can be performed on fully hydrated gels that were formed *in situ*. However, for the scattering experiments performed in this study, we are limited to characterizing features smaller than ~ 50 nm. This is smaller than the largest fiber diameters and not large enough to yield information about the overall network structure of the gels. However, when used in combination, these techniques complement each other and provide details about the structure of the individual fibers, the gel porosity, and the network density.

Fibrin gels were prepared from 1 mg/mL fibrinogen for SEM analysis. In Figure 5.4 SEM images at 1,000 and 20,000 \times magnification are presented for oxidized and untreated fibrin. In the 1,000 \times magnified images it is clear that the network density increases dramatically with increasing oxidation. In the non-oxidized fibrin gel very large fibers are separated by pores with diameter on the order of ~ 10 μm . In the 50 HOCl oxidized fibrin gel, the pore size is greatly reduced but remains on the order of ~ 1 μm . In the most highly oxidized fibrin gel, the pore size is on the order of ~ 100 nm. It should be noted that in the 150 HOCl oxidized fibrin gels the fibers were so closely packed in the bulk of gel that the sputtered gold obscured the individual fibers. For this reason, these images were taken near the edge of the gel where the fiber density was lower. It is expected that the high fiber density and reduced porosity observed in the oxidized fibrin

gels will lead to reduced diffusivity through the gel and impede the transport of enzymes critical to fibrinolysis.

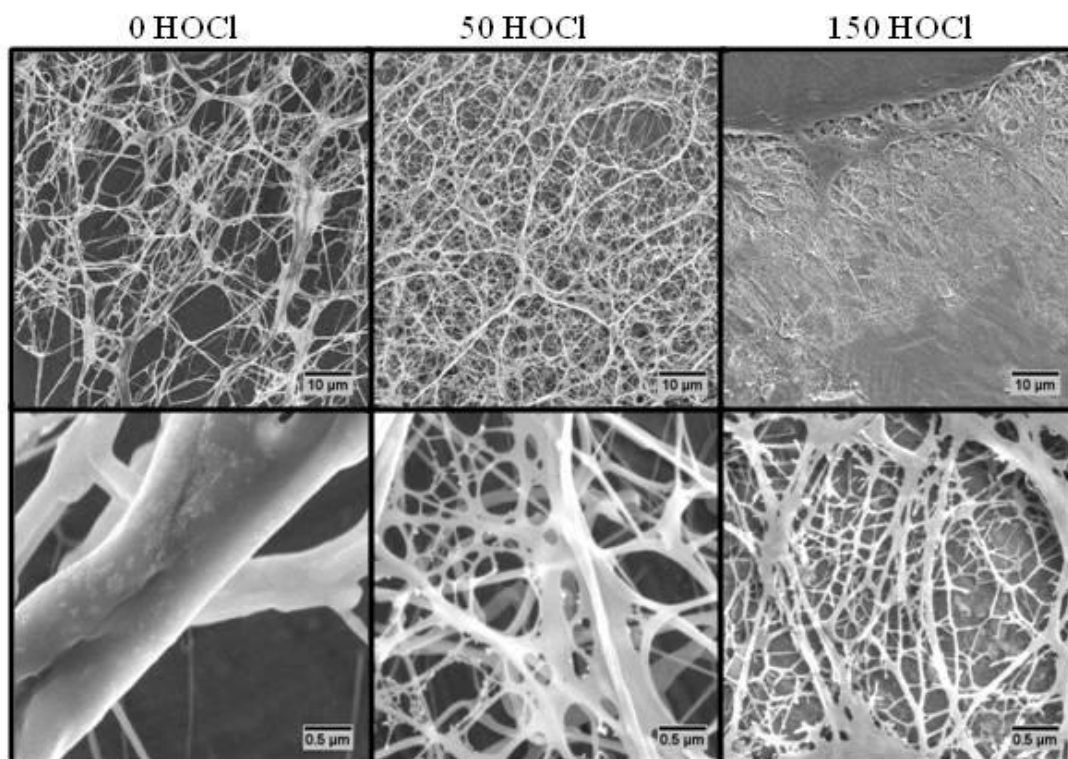


Figure 5.4: Scanning electron microscopy images of fibrin gels from HOCl oxidized fibrinogen at 1000X (top) and 20,000X (bottom) magnification.

SANS is used to characterize the structure of fully hydrated baseline and 150 HOCl fibrin gels. A relatively high concentration (6.5 mg/mL) of fibrinogen is used to increase the scattering relative to the background. Additionally, after gelation the hydrogenated buffer is exchanged for a deuterated buffer in order to reduce the incoherent scattering background. The scattering intensity (I) is plotted against the scattering vector (q) in Figure 5.5. Here, we observe substantial differences in the scattering from the oxidized and non-oxidized fibrin gels, as expected based on the results from the SEM and turbidity studies. The scattering from the baseline gel is typical for a coarse fibrin clot as presented in Chapters 3 and 4.^{26, 28} However, in the oxidized gel

the Guinier transition corresponding to the fiber diameter occurs at significantly higher- q , which is an indication of reduced fiber diameter. Additionally, there is no clear Porod region separating the internal structural features from the cross-sectional Guinier, suggesting that the fibers either have a broad or perhaps bimodal distribution in the fiber radius.

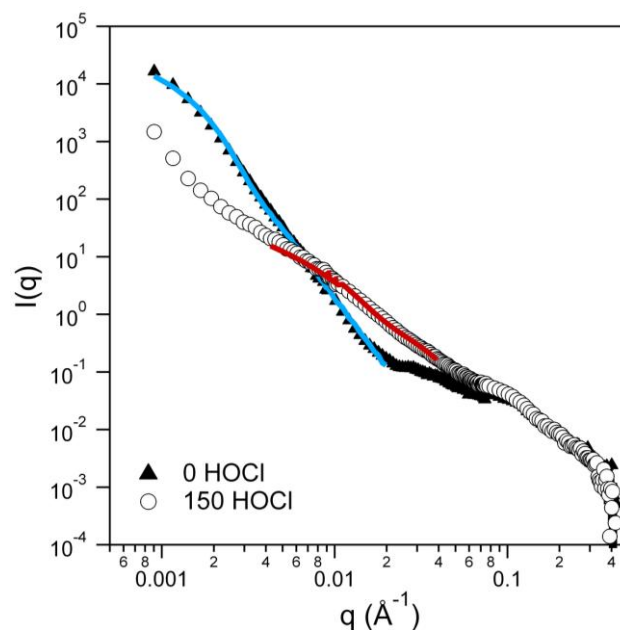


Figure 5.5: SANS data from 6.5 mg/mL fibrin gels treated with 0 and 150 μmol HOCl per gram fibrinogen. The data fits using the cylinder and bimodal cylinder models are represented as solid blue and red lines respectively.

The scattering from the non-oxidized gel was fit with a cylinder form factor model (Eq. 2.22). This model is described in detail in Chapter 2. The scattering length densities of the solvent and fibrinogen were fixed at 6.08×10^{-6} and $3.17 \times 10^{-6} \text{ \AA}^{-2}$ respectively and polydispersity in the radius was accounted for using a Schulz distribution with a polydispersity index of 0.3. The scattering in this q -range is not sensitive to the fiber length, so the length is held fixed at an arbitrary value of 1000 nm. The data was fit over a restricted q -range from 0.0009 - 0.02 \AA^{-1} , as the model does not

account for the high- q scattering that arises from the internal structure of the fibers. The resulting fit is plotted as a solid line over the 0 HOCl fibrin gel scattering in Figure 5.5 and the average fiber radius is found to be 95 nm.

The 150 HOCl gel is not well represented by a single polydisperse cylinder model. Instead, this data is fit with a bimodal distribution by summing the form factors of two polydisperse cylinders (Schulz distribution, PDI=0.3). As with the baseline gel, the polydispersity, scattering length densities, and fiber length are held constant. Here, the data is fit over a limited q -range between $0.004 < q < 0.04 \text{ \AA}^{-1}$. The resulting fit is plotted over the 150 HOCl scattering curve in Figure 5.5, with the best fit found with average radii at 15 and 3.4 nm. While the fit was very good, there is significant uncertainty in the absolute value of this fit. In fact, the small radius determined from the fit is slightly less than is typically reported for a single protofibril ($\sim 10 \text{ nm}$).²⁹ This result is consistent with the SEM images where both very small and slightly larger fibers are observed. In this section, we have used three complementary techniques to demonstrate that oxidation with HOCl inhibits the lateral aggregation of protofibrils leading to the formation of a network of densely packed fine fibers.

Rheology

The multiscale structure of fibrin gels gives rise to interesting linear and non-linear mechanical properties that are critical to the function of fibrin clots *in vivo*. Altered mechanical properties reflect changes in clot structure and measurements of these properties are often used as a diagnostic tool for coagulopathy. Typically, the mechanical properties of fibrin gels are measured with shear rheology (research) or thromboelastography (clinical).^{2, 30} In shear rheology, the structure of a clot is informed

by various models for the linear and non-linear elastic modulus as a function of concentration or strain.³¹⁻³³ Given the vast number of physiological modifications that human fibrinogen can undergo, mechanical measurements are a powerful tool for detecting abnormal fibrin coagulation

In this study, the mechanical properties of the fibrin gels are measured with shear rheology techniques. At low strain (<1%), the fibrin gels are below the linear viscoelastic limit. Small amplitude oscillations at strains within the linear viscoelastic limit were used to track the evolving elastic and viscous modulus during gelation. The viscous and elastic moduli are plotted as a function of time in Figure 5.6 (left). As with the UV-Vis measurements, we find that there are no significant changes in the gelation time and in all three cases the modulus is increasing only slightly at the end of a one hour gelation period. A long frequency sweep between 0.0005 and 50 Hz is also performed and data from these measurements are reported in Figure 5.6 (right). All of the samples, oxidized and baseline, have gel-like properties with $G' > G''$ over the entire frequency range that is probed. This is typical for crosslinked fibrin at the concentrations probed in this study.

In Figure 5.7, we examine the concentration dependence of the linear elastic modulus. The elastic modulus at 0.5% strain is plotted over a concentration range spanning two decades. We find that the oxidized gels are systematically weaker than the baseline gels, but that the overall concentration dependence is effectively the same. The linear elastic modulus is found to vary exponentially with fibrinogen concentration such that G' increases as $C^{2.12}$, $C^{2.32}$, and $C^{2.35}$ for the 0, 50 and 150 HOCl fibrin gels respectively. The variation in the exponential dependence is thought to be a result of experimental error rather than an indication of any underlying structural changes.

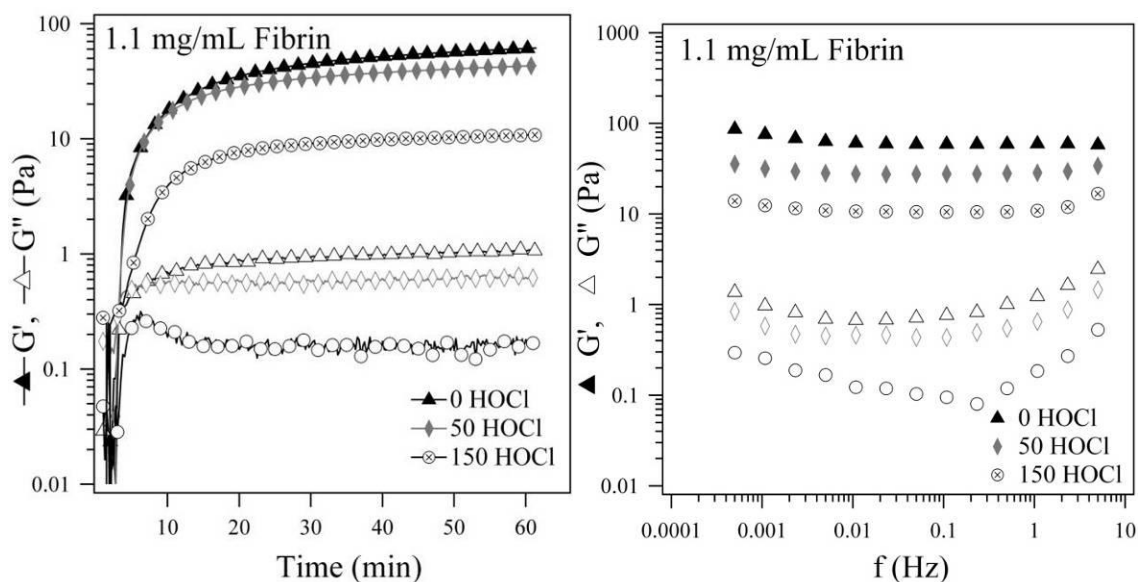


Figure 5.6: The elastic (G') and viscous (G'') moduli of oxidized and baseline fibrin gels are plotted as a function of time during gelation (left) and as a function of oscillation frequency for fully formed gels.

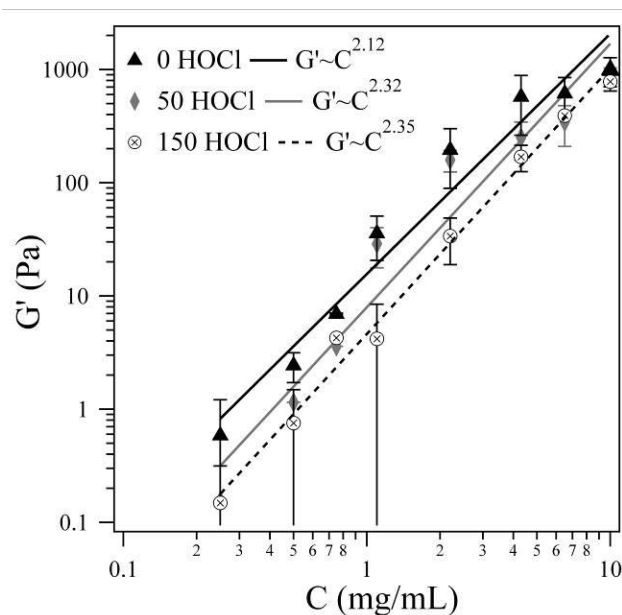


Figure 5.7: Linear elastic modulus of the fibrin gels plotted against the fibrinogen concentration.

Macintosh et. al., proposed a model which predicts that the linear elastic modulus of cross-linked biopolymer networks should have an exponential concentration dependence with $G' \sim C^{2.5}$. However, various experimental studies report exponential dependence for cross-linked fibrin ranging between $G' \sim C^{1.66}$ and $G' \sim C^{2.22}$.^{2, 26, 30, 33} The

values reported herein are consistent with these previous results. Additionally, SDS-PAGE separations were performed by collaborators Dominic Chung and Nathan White and used to demonstrate that covalent crosslinkage by Factor XIIIa is not inhibited by HOCl oxidation. The 115 kD - dimers (α_2) are prominent in both the oxidized and native fibrin samples and are indicative of covalent cross-linkage via Factor XIIIa. This is clear evidence that Factor XIII activation by thrombin and the activity of Factor XIIIa is not impaired by HOCl oxidation.

Fibrin gels are also known to exhibit highly non-linear strain hardening mechanical properties. To measure the non-linear rheology of the oxidized fibrin gels, a continuously increasing stress ramp is applied until the gel fails and the resulting strain is measured at discrete stress intervals. It should be noted however, that all of the 6.5 mg/mL fibrin gels and some of the 4.3 mg/mL fibrin gels were too strong to break in the rheometer. The instantaneous modulus (G_{inst}) is determined by taking the derivative of the shear stress (τ) with respect shear strain (γ). Curves of the average instantaneous modulus for 1.1, 2.2, 4.3 and 6.5 mg/mL fibrin gels formed from baseline and oxidized fibrinogen are plotted in Figure 5.8. The error bars reflect the standard deviation from a minimum of three different gels.

The non-linear rheology of fibrin is related to the underlying hierarchical structure of the clot and is therefore affected by alterations to the monomer. Like many biopolymers, fibrin gels are highly extensible and exhibit strain hardening.^{32, 33, 35} In this study all of the fibrin gels we tested strain hardened regardless of concentration or oxidation levels. The instantaneous modulus at the maximum strain before gel failure is typically 1-2 orders of magnitude greater than the linear elastic modulus. We consistently

find the maximum strain and maximum modulus are lower for oxidized gels than for baseline gels. For the 1 mg/mL gels, the average maximum strain before failure is

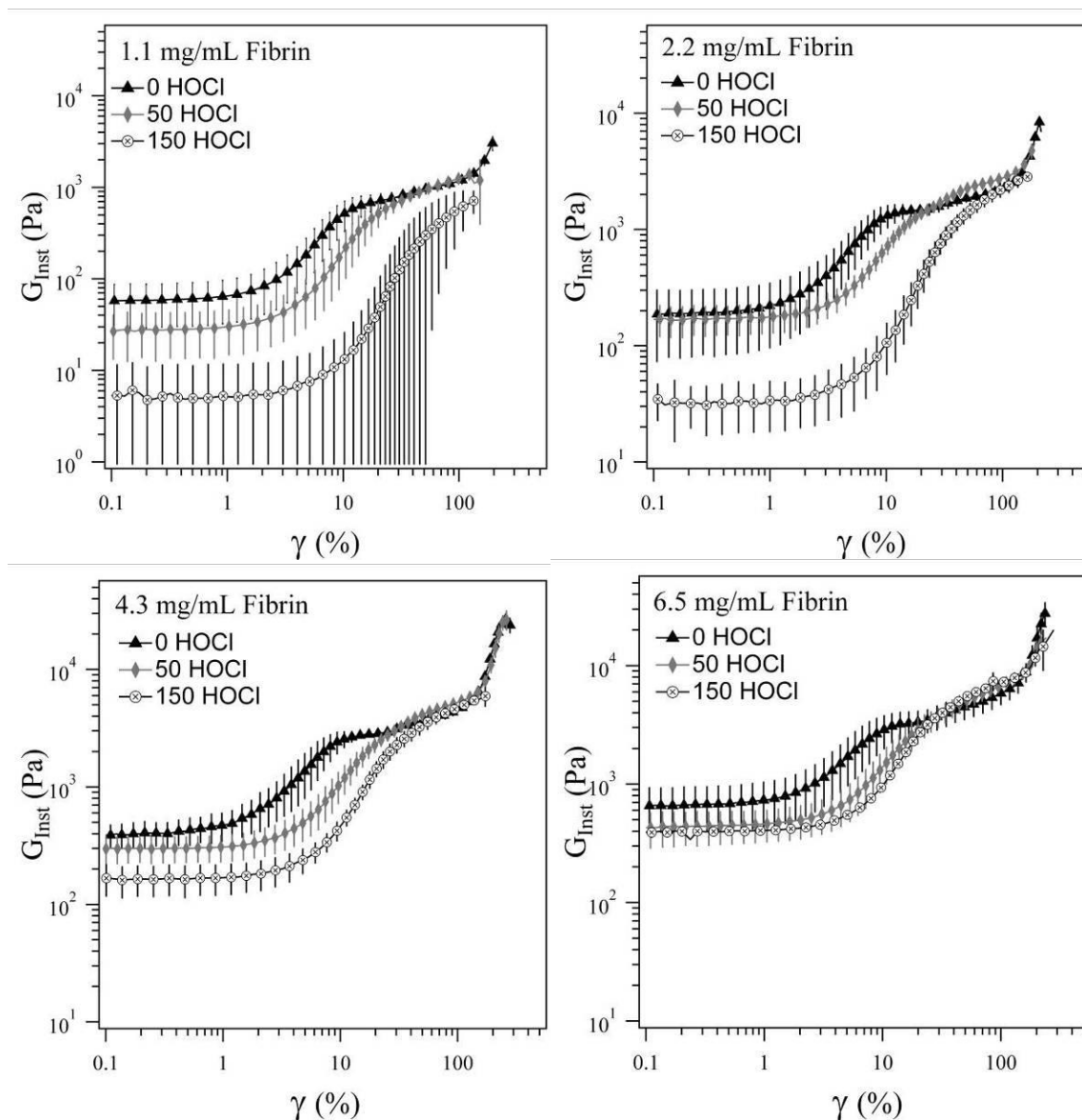


Figure 5.8: Instantaneous modulus (G_{Inst}) of fibrin gels with various concentrations of fibrinogen and oxidized to different levels with 0, 50 and 150 $\mu\text{mol HOCl/g}$ fibrinogen. Data plotted is the average of at least three trials with error bars corresponding to the standard deviation.

202 \pm 31, 143 \pm 10 and 157 \pm 20% for 0, 50, and 150 HOCl gels respectively. The average maximum modulus reached before gel failure is 3000 \pm 1500, 1400 \pm 100, and 800 \pm 200 Pa respectively. Though the linear elastic moduli and maximum instantaneous moduli of the

oxidized gels are lower than those measured in the baseline gels, at intermediate strains (approaching 100%) the magnitude of the instantaneous modulus of the baseline and oxidized gels begin to equalize. All of the baseline gels experience a second increase in the magnitude of strain hardening at very high strain. This upturn also occurs in the higher concentration 50 HOCl gels and the 6.5 mg/mL 150 HOCl gel.

The limit of linear viscoelasticity of the gels is also affected by HOCl oxidation. We find that the onset of strain hardening occurs at progressively higher strain with increasing oxidation. We quantify the delayed strain hardening by measuring the strain at which the instantaneous modulus reaches 200% of the linear modulus. This characteristic strain is found to be 3.6 ± 0.6 , 5.5 ± 1.5 and $7.5\pm 1.1\%$ for 0, 50, and 150 HOCl fibrin gels respectively when averaged over all concentrations. The linear viscoelastic limit also increases slightly with concentration, which is consistent with current models for strain hardening.^{33,36}

Clot Lysis

HOCl oxidation has been implicated in altered fibrinolysis in at least one previous report.¹⁵ Given the altered clot structure and rheology observed in this study, delayed fibrinolysis was expected in the oxidized fibrin gels as a direct result of reduced diffusivity of enzymes and co-factors through smaller pores. From the SEM images we estimate the pore size of the gels to be on the order of magnitude of 10 μm for untreated fibrinogen, 1 μm for the 50 HOCl oxidized fibrinogen, and 100 nm for the 150 HOCl oxidized fibrinogen at 1 mg/mL. The stokes radius of plasminogen is ~ 5 nm.³⁷ The

diffusion coefficient for plasminogen at infinite dilution in water (D_{AB}) can be calculated from the Stokes-Einstein equation:³⁸

$$D_{AB} = \frac{kT}{6\pi R\mu_B} \quad \text{Equation 5.1}$$

where, k is the Boltzmann's coefficient, T is the temperature, R is the radius of plasminogen, and μ_B is the viscosity of water. D_{AB} of plasminogen in water is calculated to be $6.49 \times 10^{-11} \text{ m}^2\text{s}^{-1}$ at 37°C .

In the case of plasminogen diffusing through a fibrin gel, the added restriction to diffusion imposed by the fiber network must be considered. Two correction factors, the steric partition coefficient ($F_1(\varphi)$) and the hydrodynamic hindrance factor ($F_2(\varphi)$) are utilized to account for this effect such that an effective diffusion coefficient for plasminogen through the fibrin gel (D_{AF}) can be calculated with Equation 5.2.³⁸

$$D_{AF} = D_{AB}F_1(\varphi)F_2(\varphi) \quad \text{Equation 5.2}$$

Both of these parameters are functions of the reduced pore diameter (φ):

$$\varphi = \frac{d_{plasminogen}}{d_{pore}} \quad \text{Equation 5.3}$$

where $d_{plasminogen}$ is the diameter of the plasminogen protein and d_{pore} is the estimated pore diameter. The steric partition coefficient accounts for the volume occupied by the plasminogen as it cannot be located closer than one radius away from the pore wall. This factor was originally derived using geometric arguments and is defined in Equation 5.4:³⁸

$$F_1(\varphi) = (1 - \varphi)^2 \quad \text{Equation 5.4}$$

The hydrodynamic hindrance factor accounts for the hindered Brownian motion of plasmin within the pore volume. The hydrodynamic hindrance factor developed by Renkin for hard spheres diffusing through cylindrical pores is valid for $0 < \varphi < 0.6$.³⁹

Though the pores in the fibrin gels are not cylindrical and the plasminogen is not a hard sphere, Equation 5.5 remains a reasonable approximation for the hydrodynamic hindrance factor in this system.

$$F_2(\varphi) = 1 - 2.104\varphi + 2.09\varphi^3 - 0.95\varphi^5 \quad \text{Equation 5.5}$$

Given the estimated pore sizes for fibrin gels with and without oxidation, the effective diffusion coefficients of plasminogen in gels are estimated as 6.45×10^{-11} , 6.09×10^{-11} and $3.29 \times 10^{-11} \text{ m}^2\text{s}^{-1}$ for the 0, 50, and 150 HOCl gels respectively. From these rough calculations we expect that the lysis time for oxidized fibrin gels will be only slightly delayed in the 50 HOCl fibrin gels but substantially delayed in the 150 HOCl fibrin gels.

A series of fibrinolysis experiments were performed using the rheometer with small amplitude shear oscillations to monitor the elastic and viscous modulus during gelation and the subsequent lysis of fibrin gels *in situ*. In this experiment 2.2 mg/mL fibrinogen and 1 $\mu\text{g/mL}$ plasminogen was combined with 1 NIH units/mL thrombin and 0.5 $\mu\text{g/mL}$ tPA and loaded directly into the rheometer using the cone and plate geometry. The results of this experiment are presented in Figure 5.9. We find that, as expected, the lysis time is delayed in oxidized gels. More specifically the lysis time is approximately inversely proportional to the calculated effective diffusion coefficients.

Fibrin is known to increase the rate of tPA-induced conversion of plasminogen to plasmin by increasing exposure of tPA binding sites.³⁸ When comparing fibrinogen to fibrin, tPA-induced plasmin activation is typically increased by a ratio of approximately 1:1.5-2. We anticipated that fibrinogen oxidation might decrease the rate of tPA-dependent plasminogen activation. However, both control and oxidized fibrin/fibrinogen

plasminogen activation ratios were similar (1.60 vs. 1.66 respectively), leading us to conclude that the rate of tPA-induced activation of plasminogen is essentially unchanged by the presence of oxidized fibrin. Therefore, the delayed lysis time may be fully attributed to the clot architecture and impaired plasminogen diffusion.

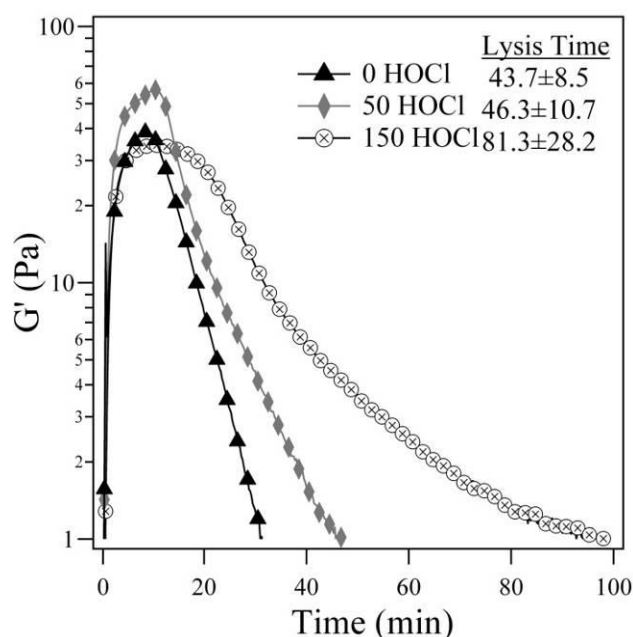


Figure 5.9: Fibrinolysis induced by tPA and plasminogen in 2.2 mg/mL fibrin gels formed from fibrinogen treated with 0, 50 and 150 $\mu\text{mol/g}$ fibrinogen.

Discussion

Fibrinogen treatment with HOCl leads to the preferential oxidation of specific methionine residues on the α , β and γ chains. The oxidation of one or all of these residues inhibits the lateral aggregation of protofibrils resulting in gels with smaller fibers and higher fiber density when compared with untreated fibrin gels. Both the linear and non-linear mechanical properties are affected by oxidation. Oxidized fibrin gels are weaker and experience a delayed onset of strain hardening.

High fiber density as a result of fine fiber formation is thought to reduce the diffusion rate of plasminogen through the gel and lead to prolonged lysis times. Several

medical conditions associated with thrombosis, including diabetes and impaired kidney function, have been associated with these characteristics.^{7,8} The results presented in this study suggest that a potential oxidation-specific mechanism associated with these diseases may be related to neutrophil activation and inflammation *in vivo*.^{10, 11} Moreover, in this chapter we demonstrate that the delayed lysis is not a result of decreased tPA-dependent activation of plasminogen, but rather can be fully attributed to a reduction in gel porosity and hindered diffusion of the plasminogen through the clot.

These results support an oxidative impairment of fibrin polymerization as has been previously reported.⁴⁰ Though, the exact mechanism of altered fibrin polymerization remains unclear, several studies have demonstrated inhibited lateral aggregation of protofibrils through the manipulation of the fibrinogen α -C domains.⁴²⁻⁴⁵ Removal of the α -C domain or substitution with chicken α -C domains inhibits lateral aggregation and results in clots similar to ours with higher fiber density, weaker gels and prolonged fibrinolysis times.^{43, 44} The distinct similarities between the abnormal coagulation observed with the α -C domain variants and our results suggest that perhaps oxidation via HOCl acts by promoting a conformational change in the α -C domain that inhibits interactions with adjacent domains during fibrin fiber polymerization.

The most preferentially oxidized methionine residue is α -476 with 2.4, 25.6 and 72.7% oxidized in the 0, 50, and 150 HOCl solutions respectively. This methionine is the first residue on a second β -sheet hairpin complex in the N-terminal subdomain of the α -C domain. Tsurupa and colleagues found that this second β -sheet hairpin is relatively unstable in human fibrinogen and that the unfolding of this structure reduces the extent of α -C fragment oligomerization.²⁵ Therefore, we suggest that oxidation of the methionine

residue α -476 is important for the altered clotting of HOCl oxidized fibrin gels by its effect on α -C domain interactions during fibrin clot formation.

References

1. R. F. Doolittle, *Annu. Rev. Biochem.*, 1984, **53**, 195-229.
2. E. A. Ryan, L. F. Mockros, J. W. Weisel and L. Lorand, *Biophysical Journal*, 1999, **77**, 2813-2826.
3. Z. Yang, I. Mochalkin and R. F. Doolittle, *Proc. Natl. Acad. Sci. U. S. A.*, 2000, **97**, 14156-14161.
4. E. Pretorius, H. Steyn, M. Engelbrecht, A. C. Swanepoel and H. M. Oberholzer, *Blood Coagulation & Fibrinolysis*, 2011, **22**, 696-700.
5. J. P. Collet, Z. Mishal, C. Lesty, M. Mirshahi, J. Peynet, A. Baumelou, A. Bensman, J. Soria and C. Soria, *Thrombosis and Haemostasis*, 1999, **82**, 1482-1489.
6. G. Jorneskog, K. Fatah and M. Blomback, *Fibrinolysis Proteolysis*, 1998, **12**, 360-365.
7. A. H. Henschen-Edman, in *Fibrinogen*, 2001, pp. 580-593.
8. E. Shacter, J. A. Williams, M. Lim and R. L. Levine, *Free Radical Biology and Medicine*, 1994, **17**, 429-437.
9. T. W. Stief, J. Kurz, M. O. Doss and J. Fareed, *Thrombosis Research*, 2000, **97**, 473-480.
10. S. L. Hazen, F. F. Hsu, D. M. Mueller, J. R. Crowley and J. W. Heinecke, *Journal of Clinical Investigation*, 1996, **98**, 1283-1289.
11. B. Shao, A. Belaouaj, C. L. M. J. Verlinde, X. Fu and J. W. Heinecke, *Journal of Biological Chemistry*, 2005, **280**, 29311-29321.
12. D. I. Pattison, C. L. Hawkins and M. J. Davies, *Biochemistry*, 2007, **46**, 9853-9864.
13. A. Nalian and A. V. Iakhiaev, *Thrombosis and Haemostasis*, 2008, **100**, 18-25.
14. C. B. Glaser, J. Morser, J. H. Clarke, E. Blasko, K. McLean, I. Kuhn, R. J. Chang, J. H. Lin, L. Vilander, W. H. Andrews and D. R. Light, *Journal of Clinical Investigation*, 1992, **90**, 2565-2573.
15. T. W. Stief, *Clinical and Applied Thrombosis-Hemostasis*, 2007, **13**, 259-278.
16. J. P. Collet, D. Park, C. Lesty, J. Soria, C. Soria, G. Montalescot and J. W. Weisel, *Arteriosclerosis Thrombosis and Vascular Biology*, 2000, **20**, 1354-1361.
17. M. E. Carr and J. Hermans, *Macromolecules*, 1978, **11**, 46-50.
18. X. Fu, J. Chen, R. Gallagher, Y. Zheng, D. W. Chung and J. A. Lopez, *Blood*, 2011, **118**, 5283-5291.
19. C. J. Glinka, J. G. Barker, B. Hammouda, S. Krueger, J. J. Moyer and W. J. Orts, *J. Appl. Crystallogr.*, 1998, **31**, 430-445.
20. S. R. Kline, *J. Appl. Crystallogr.*, 2006, **39**, 895-900.
21. D. L. Sauls, E. Lockhart, M. E. Warren, A. Lenkowski, S. E. Wilhelm and M. Hoffman, *Biochemistry*, 2006, **45**, 2480-2487.

22. B. Kalyanaraman and P. G. Sohnle, *Journal of Clinical Investigation*, 1985, **75**, 1618-1622.
23. J. M. Kollman, L. Pandi, M. R. Sawaya, M. Riley and R. F. Doolittle, *Biochemistry*, 2009, **48**, 3877-3886.
24. H. Berman, K. Henrick and H. Nakamura, *Nature Structural Biology*, 2003, **10**, 980-980.
25. G. Tsurupa, R. R. Hantgan, R. A. Burton, I. Pechik, N. Tjandra and L. Medved, *Biochemistry*, 2009, **48**, 12191-12201.
26. K. M. Weigandt, D. C. Pozzo and L. Porcar, *Soft Matter*, 2009, **5**, 4321-4330.
27. C. Yeromonahos, B. Polack and F. Caton, *Biophysical Journal*, 2010, **99**, 2018-2027.
28. K. M. Weigandt, L. Porcar and D. C. Pozzo *Soft Matter*, 2011, **7**, 9992-10000.
29. P.A. Janmey, J.P. Winer, and J.W. Weisel. *J. R. Soc. Interface*. 2009, **6**, 1-10.
30. V. G. Nielsen, B. M. Cohen and E. Cohen, *Acta Anaesthesiologica Scandinavica*, 2005, **49**, 222-231.
31. F. C. MacKintosh, J. Kas and P. A. Janmey, *Phys. Rev. Lett.*, 1995, **75**, 4425-4428.
32. C. Storm, J. J. Pastore, F. C. MacKintosh, T. C. Lubensky and P. A. Janmey, *Nature*, 2005, **435**, 191-194.
33. P. R. Onck, T. Koeman, T. van Dillen and E. van der Giessen, *Phys. Rev. Lett.*, 2005, **95**, 4.
34. P. A. Janmey, U. Euteneuer, P. Traub and M. Schliwa, *Journal of Cell Biology*, 1991, **113**, 155-160.
35. T. van Dillen, P. R. Onck and E. Van der Giessen, *Journal of the Mechanics and Physics of Solids*, 2008, **56**, 2240-2264.
36. H. Kang, Q. Wen, P. A. Janmey, J. X. Tang, E. Conti and F. C. MacKintosh, *J. Phys. Chem. B*, 2009, **113**, 3799-3805.
37. J. M. Marshall, A. J. Brown and C. P. Ponting, *Biochemistry*, 1994, **33**, 3599-3606.
38. C. E. Wicks, Welty, W. R., Wilson, R.E., and Rorrer, G.L., *Fundamentals Of Momentum, Heat, And Mass Transfer*, John Wiley & Sons, Inc., 2008.
39. E. M. Renkin, *Journal of General Physiology*, 1954, **38**, 225-243.
40. W. Nieuwenhuizen, in *Fibrinogen*, 2001, pp. 237-246.
41. E. Shacter, J. A. Williams and R. L. Levine, *Free Radical Biology and Medicine*, 1995, **18**, 815-821.
42. J. W. Weisel and L. Medved, in *Fibrinogen*, 2001, pp. 312-327.
43. J.-P. Collet, J. L. Moen, Y. I. Veklich, O. V. Gorkun, S. T. Lord, G. Montalescot and J. W. Weisel, *Blood*, 2005, **106**, 3824-3830.
44. L. Ping, L. Huang, B. Cardinali, A. Profumo, O. V. Gorkun and S. T. Lord, *Biochemistry*, 2011, **50**, 9066-9075.
45. G. Tsurupa, A. Mahid, Y. Veklich, J. W. Weisel and L. Medved, *Biochemistry*, 2011, **50**, 8028-8037.

Chapter 6

Structure and Rheology of P3HT Gels

Introduction

Given the pressing demand for clean energy sources, it is not surprising that the design of novel materials for producing efficient solar devices is a very active research area. Silicon based solar cells with high efficiency (>20%) are commercially available, but wide spread use of these devices is cost prohibitive when compared with traditional power sources.¹ While it is generally acknowledged that organic solar cells are not as efficient as their inorganic counterparts, the ease with which polymer solar cells can be processed and the ability to manufacture flexible devices with organic materials motivate the design and optimization of organic photovoltaic devices (OPVs).²

When sunlight strikes an OPV an exciton, or hole-electron pair, is generated. To generate current, the exciton must diffuse to the interface between the donor and acceptor material where the hole and electron will dissociate and diffuse to the appropriate electrodes. This process is represented schematically in Figure 6.1. The morphology of

the active layers is critical to the performance of the OPVs and, to this end, significant focus has been placed on the development of novel materials and the optimization of the active layer morphology.

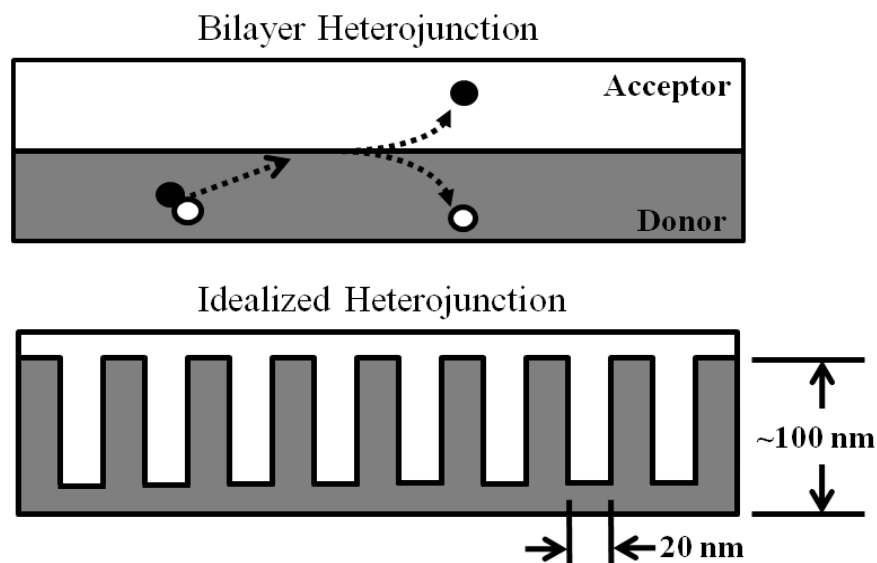


Figure 6.1: Example of a simple heterojunction and the idealized heterojunction suggested for maximizing device efficiency.

In a review from 2004, Coakley and McGehee suggested that producing a 10% efficient device with a lifespan of at least 10 years would result in commercial viability.² Furthermore, they outlined the key steps necessary to reach this benchmark performance level including designing new polymers with better electrical properties and optimizing the bulk heterojunction morphology. A schematic of a hypothetically ideal heterojunction is presented in Figure 6.1. The comb-like structure ensures that the distance an exciton must travel to reach the donor-acceptor interface is less than the distance an exciton can diffuse prior to recombination. Additionally, this idealized structure provides an unobstructed pathway for the holes and electrons to diffuse from the donor-acceptor interface to the electrodes.

Conjugated polymers are frequently used as donor materials in OPV devices. Many of these polymers are known to form fibers or gels depending on the polymer concentration, solvent, and temperature.³⁻⁷ In this Chapter, we use poly(3-hexylthiophene) (P3HT), as a model system for conjugated polymer gelation. P3HT is a commonly utilized donor material and is commonly paired with (6,6)-phenyl C61-butyric acid methyl ester (PCBM) to form a bulk heterojunction OPV.⁸⁻¹¹ P3HT is soluble in various organic solvents including benzene, toluene, and xylene at elevated temperatures between 50 and 80°C.¹²⁻¹⁴ When the solubility of the polymer is reduced in solutions of sufficient concentration, the polymer will begin to self-assemble.^{10, 15}

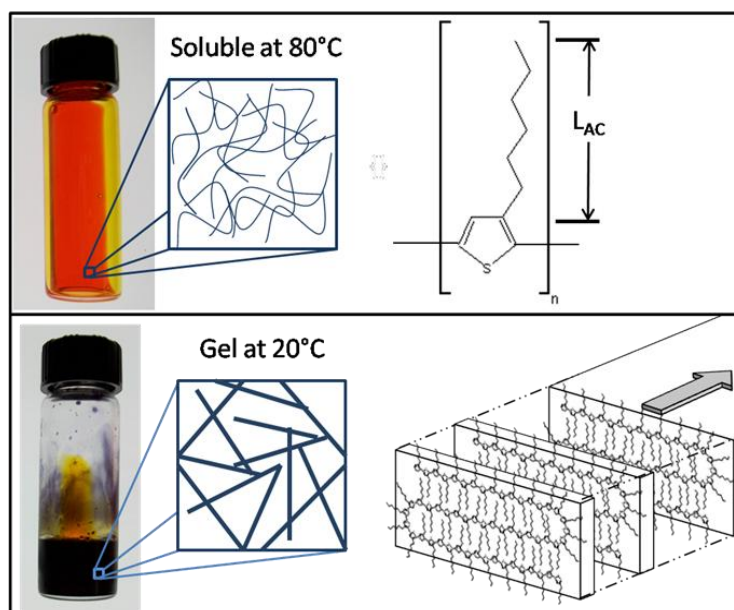


Figure 6.2: (Left) Photographs of P3HT at 80 °C and 25 °C in liquid and gel phases respectively. (Right) Schematic representation of the P3HT fiber and monomer.

The self-assembly of P3HT in solution is indicated by a characteristic spectroscopic red-shift with a striking color change from bright orange to deep purple as illustrated in Figure 6.2.¹⁶ P3HT aggregates into a semi-crystalline fibrillar structure with overlapping π -orbitals between adjacent polymer molecules (π - π stacking) along the long

fiber axis.¹⁷ Depending on crystallization conditions, the fibers are 2-10 nm thick, 20-30 nm wide and several microns in length.^{18, 19} Figure 6.2 depicts the postulated crystalline structure of P3HT fibers that is widely cited throughout the literature.¹² The overlapping π -orbitals are thought to facilitate charge transport along the fiber axis.¹⁷

One standard method for producing bulk-heterojunctions from P3HT-PCBM solutions is to spin-cast thin films of the solubilized blend.^{13, 20, 21} As the solution is spin-cast, the solvent evaporates inducing crystallization and fiber formation; however, this process is rapid and results in incomplete crystallization of the fibers.²² Typically, an annealing process at relatively high temperature is utilized to increase the crystallinity of the resulting film, but this can also lead to increased phase segregation of the component materials.^{23, 24} One method to enhance the crystallinity of P3HT is to form the fibers in dilute solution prior to spin-casting.¹² Unfortunately, the spin-casting of pre-crystallized P3HT yields thin films in which the fibers will tend to align parallel to the surface as a result of the applied shear field. So while pre-crystallizing the P3HT will lead to enhanced charge transport within the polymer phase, it will also restrict vertical charge transport between the electrode contacts.

At sufficiently high polymer concentrations (>5 mg/mL) it has been demonstrated that the crystallization of P3HT leads to the formation of a gel with a bicontinuous network of crystalline fibers.^{22, 25-28} The three-dimensional interconnected structure of a P3HT gel satisfies most of the criteria proposed by Coakley and McGehee for the ideal morphology of an OPV bulk heterojunction.² The cross-sectional dimensions of a P3HT fiber are less than the maximum exciton diffusion length and the interconnected fiber network will promote vertical charge transport through the device. However, the gelation

of P3HT is generally considered undesirable as it spoils liquid based electronic inks that are used in OPV production processes.²² This is because the mechanical properties of bulk P3HT gels prevent the utilization of traditional printing techniques when used directly. Recently, however, our group has focused on the development of electronic inks that combine the favorable morphology of P3HT gels with the processability of traditional electronic inks.²⁹

Colloidal particles of gelled P3HT in water are generated through the use of ultrasonication. The resulting particles have an effective radius on the order of 50-100 nm and optical properties that reflect the presence of crystalline P3HT fibers. Furthermore, the rheological properties of the particle suspension can be adjusted with the volume fraction of particles such that a 10% solution has a viscosity identical to water (Figure 6.3).²⁹ The underlying morphology of the gel particle is closely related to the structure of the parent gel. A thorough understanding of the structural and mechanical properties of bulk P3HT gels is necessary to optimize the electronic ink design and is one motivation for the ongoing study of these properties.



Figure 6.3: Soluble P3HT in xylene (Left), gelled P3HT in xylene (Center), and a suspension of P3HT gel particles (Right).

The critical structural, mechanical, and electronic properties of P3HT gels are largely unknown; however, some limited characterization of poly(3-alkylthiophene) (P3AT) gels has been reported in the literature.^{6, 22, 26-28, 30} Malik and Nandi have characterized the thermodynamic properties of P3HT with differential scanning calorimetry and report that gelation is a first order phase transition that occurs in two steps. The polymer undergoes a coil-to-rod transition followed by aggregations of the rod-like structure.⁶ They report that the dried P3HT gel has at least a ten-fold increase in conductivity over spun cast P3HT. Rheological characterization of the gels is very limited. Koppe et. al. determine the onset of gelation by measuring the complex viscosity as a function of time in order to evaluate electronic ink viability. Small angle x-ray scattering (SAXS) over a limited q -range has been used to characterize the fiber cross-section in P3HT gels.¹⁹ Very recently, a solar cell device with a 1.47 % efficiency was produced from a freeze dried gel.³¹

In this chapter, the results of a systematic characterization of P3HT gel morphology as a function of concentration in three relevant solvents are presented. Small angle neutron scattering (SANS), scanning transmission electron microscopy (sTEM) and UV-Vis spectroscopy are used to fully characterize the composition and morphology of P3HT gels in benzene, p-xylene, and toluene. In addition, rheological results highlighting concentration and solvent dependent mechanical properties are presented and discussed. These results lay the ground work for the rheoSANS study presented in Chapter 7 as well as ongoing work on the development of solution processable gel-based inks.

Materials and Methods

Materials

Sepiolid 200 poly(3-hexylthiophene) with regioregularity greater than 98% was purchased from Rieke Metals Inc (Lincoln, NE). This work utilizes polymer from two lots. Polymer from the two lots will be referred to as P3HT-L1 and P3HT-L2 in the text. The molecular weight distribution of the polymer from each lot is characterized using gel permeation chromatography (GPC) against a polystyrene standard. One mg/mL P3HT is dissolved into chlorobenzene and filtered using a 200 nm PTFE filter to remove any impurities. P3HT-L1 is shown to have an average molecular weight $M_w=24,000$ g/mol with a polydispersity index (*PDI*) equal to 2.0 and P3HT-L2 has an average molecular weight $M_w=16,800$ g/mol with $PDI=1.6$, where $PDI=M_w/M_n$. Toluene, p-xylene and benzene are purchased from Sigma Aldrich (St. Louis, MO). Deuterated 98% D-10 p-xylene, 99.5% D-6 benzene and 99.5% D-8 toluene are purchased from Cambridge Isotopes (Andover, MA) for neutron scattering experiments.

Gel Preparation

P3HT at concentrations ranging between 1-100 mg/mL is solubilized in benzene, xylene, and toluene by heating the solutions to approximately 80°C. The polymer is considered fully solubilized when the solution is bright orange and there are no visible undissolved polymer particles. At this point the solution is removed from heat and allowed to cool to room temperature. As the solution cools, the P3HT forms a gel. Subsequent analysis with SANS, sTEM, and UV-Vis spectroscopy is carried out after the equilibrium condition is reached (~ 24 hours).

UV-VIS Spectroscopy

UV-Vis spectroscopy is performed with a Thermo Scientific Evolution 300 spectrophotometer. An extinction coefficient for soluble P3HT at ~450 nm (ξ_{450nm}) has been measured and is found to be 50 mL/mg cm. The extinction coefficient enables the concentration of soluble P3HT (C_{P3HT}^{Sol}) to be calculated from the absorption (A) at 450 nm through a defined pathlength, L , from Beer's law using Equation 6.1:

$$C_{P3HT}^{Sol} = \frac{A}{\xi_{450nm} L} \quad \text{Equation 6.1}$$

Scanning Transmission Electron Microscopy

Small quantities of the organogels are transferred to copper TEM grids with Formvar support films by gently touching the grid to the surface of the gels without applying pressure. In this way, only a thin-film of organogel is transferred to the TEM grid. The aromatic solvents quickly evaporate under ambient conditions as the sample volume is very small. All images are obtained using scanning TEM on a FEI Tecnai G2 F20 instrument operating at 120 kV and were processed in Image J software.³²

Small angle neutron scattering

Small angle neutron scattering (SANS) and ultra small angle neutron scattering (USANS) measurements are performed on the same samples at the Center for Neutron Research at NIST in Gaithersburg, Maryland. SANS measurements are performed on the NG3 30 m instrument.³³ Measurements are made at three detector distances of 1.3, 7 and 13.2 meters to cover a broad q -range (0.001 to 0.3 Å⁻¹) using neutron wavelengths of 5 Å and 8.4 Å. All of the SANS data are corrected for background and sample cell scattering,

and are placed on an absolute scale by measuring the direct beam flux.³⁴ USANS measurements are performed on the BT5 perfect crystal diffractometer extending the measured q -range down to $4 \times 10^{-5} \text{ \AA}^{-1}$.³⁵ Data is reduced and desmeared using the NIST Igor based software.³⁴

Rheology

Rheological data was obtained with an Anton Paar MCR 301 stress controlled rheometer using both parallel plate and concentric cylinder configurations with a Peltier heat exchanger for temperature control. Making reproducible rheological measurements of thermoreversible organogels formed in volatile solvents proves especially challenging because of solvent evaporation during the heating-cooling cycles. To prevent evaporation, simple evaporation blockers illustrated in Figure 6.4 are used to trap the solvent, practically eliminating evaporative effects. The 25 mm parallel plate tool is used with at variable gap thickness between 0.25 and 1 mm requiring only a maximum of 0.5 mL sample volume. An immiscible edge bead of ethylene glycol is used to seal the interface between the gel and the air. To ensure that the gel is not displaced by the addition of the edge bead, the sample is rapidly quenched and a gel is formed prior to application of the solvent trap. The sample is subsequently reheated to dissolve the gel prior to measurement of mechanical properties. For concentric-cylinder measurements a 25 mm long by 17 mm diameter bob in a cup with a 1.0 mm gap, requiring ~5 mL sample volume is utilized. A custom solvent trap was machined to minimize evaporation by trapping the solvent molecules with a solid barrier and a liquid reservoir. Both evaporation blockers only negligibly affect the rheological measurements.

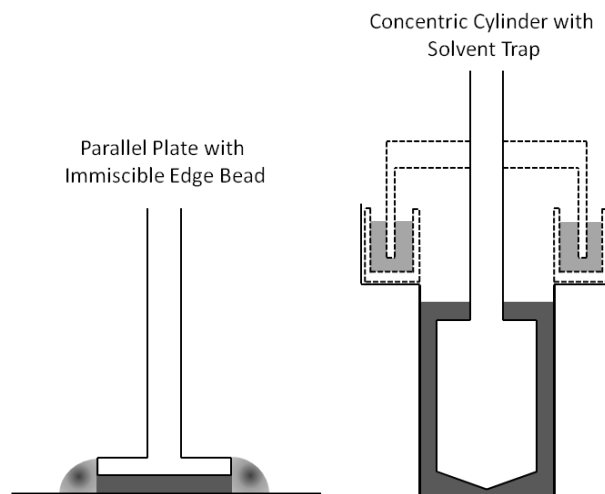


Figure 6.4: Schematic of evaporation blockers for organogel rheology.

The linear viscoelastic limit (γ_{LVE}) is established for P3HT gels with an oscillatory strain ramp from $0.001 < \gamma < 100\%$ at a frequency (f) of 1 Hz. This measurement is performed on a fully formed gel with no history of mechanical deformation. In subsequent experiments the linear mechanical properties of the gel are measured with small amplitude oscillations at strains below the linear viscoelastic limit and a frequency of 1 Hz. Additional details about specific rheology experiments are included in the sections below.

Results

The self-assembly of P3HT fiber networks occurs when the solubility of the polymer in solution is reduced either through a reduction in the solvent temperature, as is the case for all results presented in this study, or through manipulation of the solvent composition. P3HT is fully soluble at elevated temperatures in p-xylene ($\sim 70^\circ\text{C}$), toluene ($\sim 60^\circ\text{C}$), and benzene ($\sim 55^\circ\text{C}$). As the temperature is cooled, the solubility of the polymer is reduced and the polymer begins to self-assemble, forming a fibrillar gel at the

gelation temperature (T_{gel}). The structural and mechanical properties are measured for the fully formed gels.

Rheology

A full rheological characterization of toluene gels containing between 0.1 and 5 wt% P3HT are performed using the concentric cylinder rheology configuration with solvent trap. In these initial measurements, the P3HT in toluene solution is cooled from 80 °C to 10 °C at a rate of 0.5 °C/min. After the gel is cooled, it is held at 10 °C for 15 minutes prior to further measurement. During this initial cooling ramp, the mechanical properties are not tracked in order to ensure that the gel is not damaged so that the linear viscoelastic limit can be determined. The linear viscoelastic limit is measured by applying an oscillatory strain ramp from $0.001 < \gamma < 100\%$ at a frequency of 1 Hz and is found occur at approximately 0.5% strain for all gels regardless of concentration.

The gelation and dissolution of P3HT gels is tracked with small amplitude oscillations at strain amplitudes below the linear viscoelastic limit and the elastic and viscous moduli (G' and G'' respectively) of the gel is measured. An example of this measurement is shown in Figure 6.5 for a 5 wt% P3HT-toluene gel. As the solution is cooled, the polymer crystallizes and forms fibers. The percolation threshold is reached at the gelation temperature when the fibrillar domains form an interconnected network and an elastic modulus is measured. T_{gel} is approximately 24 °C for the 5 wt% P3HT gel in toluene. Beyond the percolation threshold, the elastic and loss moduli increase as a function of time and temperature as the ongoing fiber growth and increasing interconnectivity rigidifies the gel. Though not shown here, when the gel is reheated it gradually weakens but does not fully dissolve until well beyond the gelation temperature.

The evolving structural and mechanical properties of P3HT in aromatic solvents during gelation and dissolution of P3HT is the topic of Chapter 7.

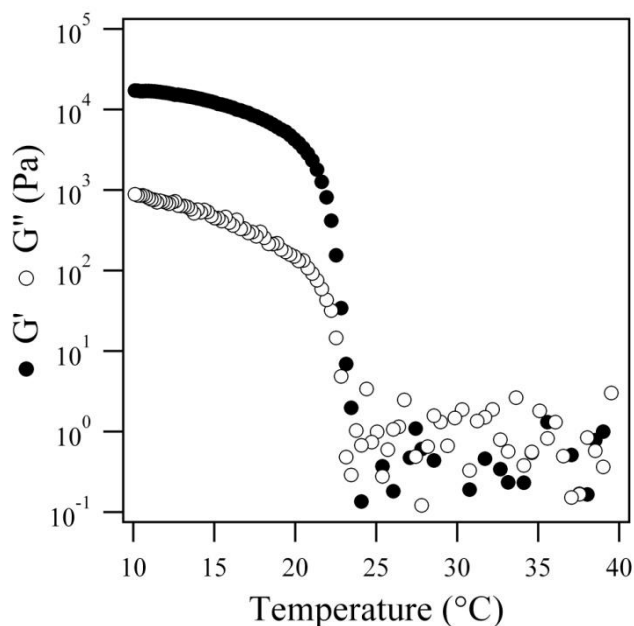


Figure 6.5: Elastic and viscous modulus of a 30 mg/mL P3HT gel as a function of temperature during a cooling ramp.

The frequency dependence of the gels are measured once the elastic modulus reaches equilibrium. The frequency sweep measurements are plotted in Figure 6.6 for gels of 0.1, 1, 1.5, 3, and 5 wt% P3HT in toluene. Here, all of the gels are probed over a minimum $0.01 < f < 100$ Hz and two of the gels (1 and 3 wt%) are probed over an expanded frequency range ($0.001 < f < 100$ Hz). The moduli are only reported for $f < 10$ Hz because at high frequency instrumental inertial effects give rise to experimental artifacts. All of these samples formed gels over the entire frequency range probed. This is especially interesting for the 0.1 wt% gel, which was not expected to form a gel based on direct observation of the samples. When the yield stress is measured by applying a logarithmically increasing shear stress ramp, we find that the yield stress for the 0.1 wt% gel is only 0.25 Pa. Just barely moving the vial that contains a 0.1 wt% gel imparts

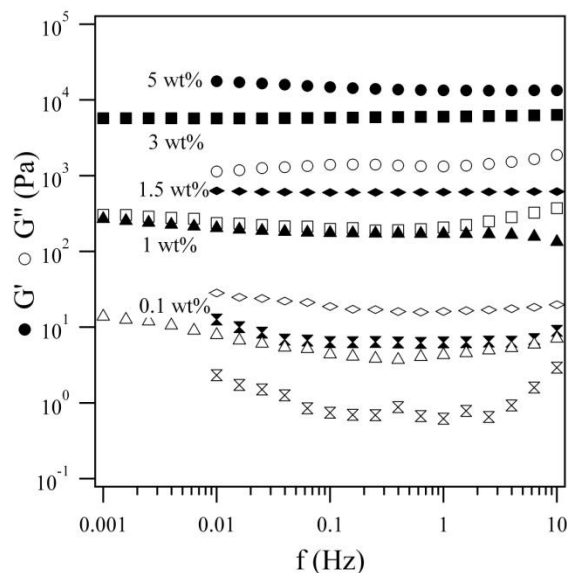


Figure 6.6: Frequency sweep for toluene gels of 5 wt% (circles), 3 wt% (squares), 1.5 wt% (diamonds), 1 wt% gels (triangle), and 0.1 wt% gels (hourglass).

sufficient force to break the gel structure that is indicated by the rheology data. The yield stress of the more concentrated gels was found to be 16, 25, 130 and 130 Pa for the 1, 1.5, 3, and 5% gels respectively. These low yield stresses make direct processing of gels by techniques such as doctor blading feasible. However, it is unknown whether any local three-dimensional network structure is maintained after damaging the gel in this manner.

A secondary rheological study of P3HT gels formed in p-xylene, toluene, and benzene is performed using a parallel plate rheometer configuration with an ethylene glycol edge bead solvent trap. In these measurements the cooling rate is increased to 3 °C per minute and the samples are cooled from a fully dissolved state to 20 °C to more closely mimic the gelation conditions utilized in the structural measurements. Gelation is then allowed to proceed for an additional 20 minutes. This is especially important for the benzene and toluene gels, where the gelation temperature is not much greater than the equilibrium temperature. The gelation as a function of time is plotted in Figure 6.7. The temperature reaches 20 °C after 10 minutes, which is indicated on the plot by a dashed

line. P3HT forms a gel in xylene at higher temperatures than observed in P3HT-toluene or P3HT-benzene sample. The elastic and viscous moduli of the toluene and xylene gels is nearly completely evolved at the end of the 30 minute gelation period; however, the benzene gel continues to slowly increase with additional time. A short frequency sweep for each of the gels is plotted in Figure 6.7 (right). In all of the gels, the moduli are independent of the frequency. Here it is clear that the final benzene gel forms the stiffest gel followed by xylene and toluene. The differences in the equilibrium modulus reflect differences in the structure. However, the exact nature of these structural differences cannot be directly determined from the rheology measurements presented herein.

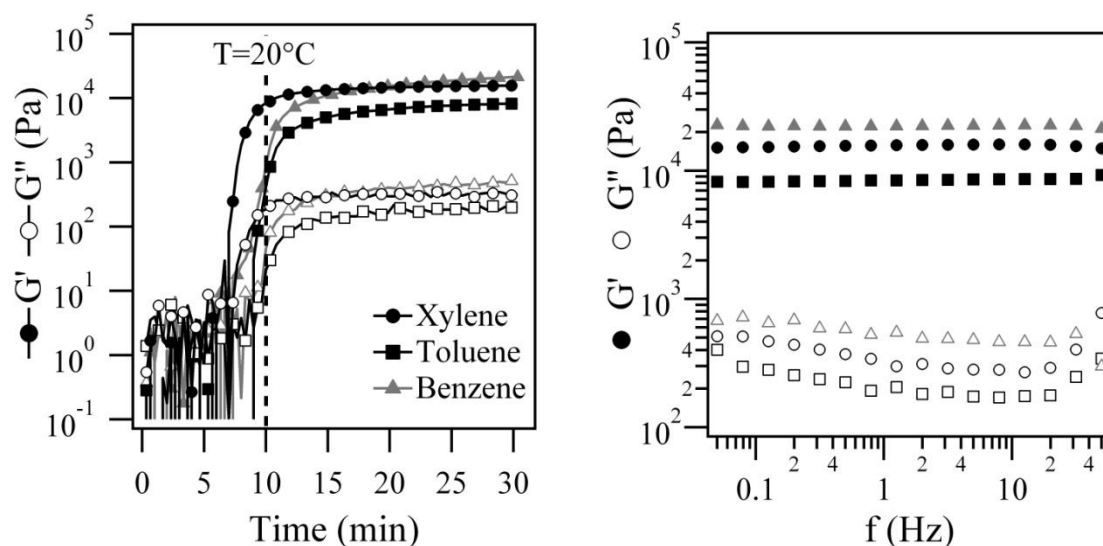


Figure 6.7: Left-Gelation as a function of time for 30 mg/mL gels cooled to 20°C at a rate of $3^\circ\text{C}/\text{min}$. $T=20^\circ\text{C}$ occurs 10 minutes into the experiment and is marked with a dashed line in the plot. Right- Frequency sweep for the gels after the 30 minute gelation period.

Gel Composition and Morphology

A combination of small angle neutron scattering (SANS) and scanning tunneling electron microscopy (sTEM) are used to characterize the morphology of P3HT gels. Additionally, UV-Vis spectroscopy is used to perform an independent assessment of the

gelation kinetics. If gelation is allowed to proceed isothermally at 20 °C, fiber growth will continue until an equilibrium state is reached as demonstrated in Figure 6.7. At equilibrium, fiber growth will cease when the remaining free polymer is fully soluble. The amount of soluble polymer at equilibrium depends on both the solvent and temperature. To ensure that the gels are fully evolved before characterizing the morphology of the gels with SANS and sTEM, it is necessary analyze the composition of the gel as a function of time. For these measurements, 10 mg/mL P3HT gels in p-xylene and toluene are prepared and sealed tightly to prevent evaporation. We assume that the results from the xylene and toluene gels will also reflect the kinetics of gelation in benzene. At regular time intervals between 1 and 48 hours, the gels are centrifuged to separate the fiber fraction from the soluble fraction. The concentration of the soluble fraction (C_{P3HT}^{Sol}) is determined by UV-Vis spectroscopy. From the soluble polymer concentration the solids fraction of P3HT relative to the total P3HT concentration (C_{P3HT}) is determined with Equation 6.2.

$$\phi_{Solid} = \frac{1 - C_{P3HT}^{Sol}}{C_{P3HT}} \quad \text{Equation 6.2}$$

The solids fraction of P3HT as a function of time is normalized to the 50 hour solids fraction concentration and plotted in Figure 6.8. Even after 50 hours at room temperature the polymer continues to crystallize slightly, however the majority of fiber formation occurs within the first hour. To ensure reproducibility, all morphological measurements are performed on gels that have been aged for at least 24 hours. Additional aging time may result in a ~5-10 % variation in the final reported polymer solids fraction.

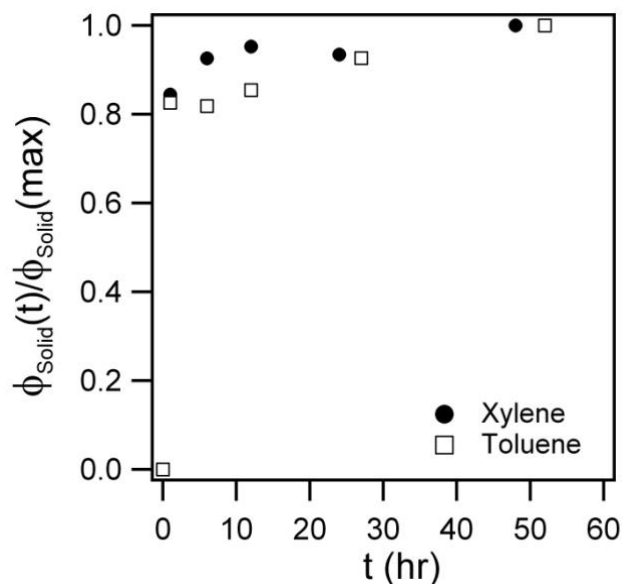


Figure 6.8: Solids fraction of P3HT as a function of time normalized by $\phi_{Solid}(t = 50)$.

As a technique, SANS is advantageous because it allows the bulk morphology of the gel to be studied in its native state. To inform the interpretation of the scattering data, the use of complementary techniques such as sTEM is invaluable. Figure 6.9 shows a series of TEM images illustrating the various structural features observed at different length scales in the dried gels. The images are from 30 mg/mL P3HT gels in toluene, but these features are typical of all of the gels studied in this chapter. As expected, the dried gels retain their underlying fibrillar structure, but the overall structure of the gel is more complex with various forms of heterogeneity including fiber bundles (or ropes), dense nucleation centers, individual fibers and bifurcations. Figure 6.9A is representative of the bulk structure observed throughout the gel and all of the features listed above are highlighted with circles.

Fiber bundling is highlighted in Figure 6.9B. These bundles are composed of several smaller fibers that are in very close proximity with less than 10 nm between

neighboring fibers. The fiber roping is consistent with results reported in another AFM study.¹⁹ The dense nucleation centers are only observed in the P3HT-L1 polymer gels and are highlighted in Figure 6.9C. It is likely that these nucleation centers arise in the presence of impurities in the polymer. We must also recall that P3HT-L1 had a higher average molecular weight than P3HT-L2 and this difference may also play a role in the formation of the spherulitic like domains.

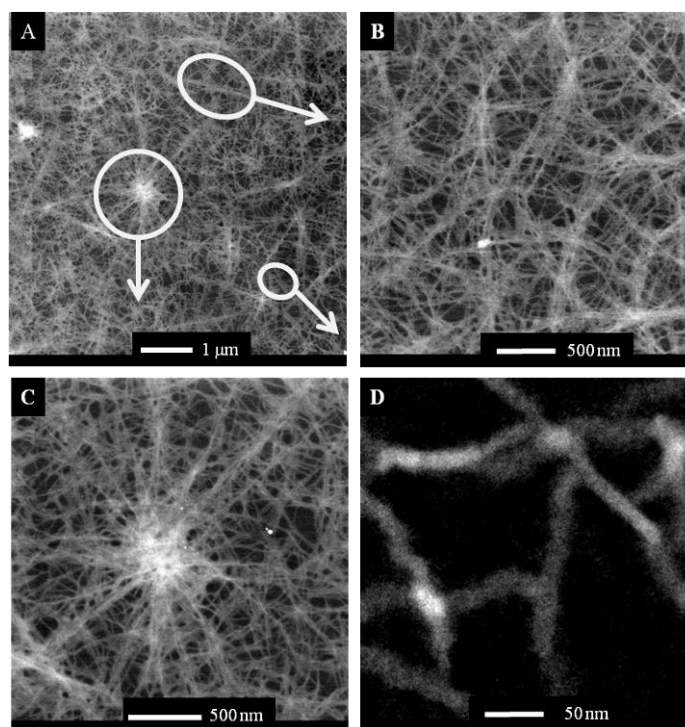


Figure 6.9: sTEM of 30 mg/mL P3HT gel in toluene. The four images highlight the structure at different length scales.

Figure 6.9D was taken near the edge of the gel where the fiber concentration is relatively low compared to the rest of the gel in order to highlight the morphology of the individual fibers and the fiber junctions. The width of the fibers is between 7.9 nm and 28 nm and the distance between fiber interaction sites is on average 60 nm. There are three types of fiber interaction in this region of the dried gel. In the upper left hand corner there

are two fibers that overlap for about 80 nm. This overlapping is may be related to the multi-fiber bundling observed in Figure 6.9B. The second interaction type is the y-junction which accounts for 70% of the fiber intersections in this image. Y-interactions can be divided into two subtypes, bifurcations and contact points; however, it is impossible to distinguish between the two in this image. True bifurcations are ideal as they allow for uninterrupted charge transport through the junction along the fiber axis through the π -orbital overlap. Contact point junctions are preferable over the alternative of having no junction, but the alkyl-side chains create an insulating layer between the adjoining fibers. The final type junction is the x-junction formed by the overlap of two crossing fibers. The x-junction accounts for 30% of the fiber overlap in Figure 6.9D. These apparent intersections are likely an artifact of drying and these fibers may or may not interact in swollen bulk gel.

A multiscale structural characterization of bulk P3HT gels in deuterated D10-p-xylene, D8-toluene, and D6-benzene over length scales between 1 nm and 10 μm is performed using a SANS and USANS measurements. Deuterated solvents are used to enhance the contrast between the polymer and the solvent. The scattering length density of the various components is calculated with Equation 2.2 and are listed in Table A1.2 in Appendix A. We originally assumed that the scattering length density of the fibers would be equal to the calculated scattering length density of the polymer. To confirm this, the scattering length density of the fibers is determined with a contrast variation experiment as described in Chapter 2. Gels with 30 mg/mL P3HT are formed in solvents of varying isotopic hydrogen composition. The extrapolated scattering intensity at $q=0$ is related to the scattering length density by the expression $I(0) \propto \rho_{SLD}^2$. The measured scattering

length density of the fibers is $\sim 40\%$ higher than the soluble P3HT and is found to be $1.07 \times 10^{-6} \text{ \AA}^{-2}$. This result suggests that the fibers contain as much as 10% entrained solvent. The measured scattering length density of the fibers and the calculated scattering length density of the solvents and polymer are used for all scattering calculations.

Samples containing 5, 10, 20, 30, and 50 mg/mL P3HT are prepared in each of the solvents. Figure 6.10 shows an isotropic scattering profile of a 30 mg/mL P3HT-L1 gel in xylene. This is typical of scattering from the lot-1 polymer. P3HT-L2 gels are similar to P3HT-L1 gels except that they do not exhibit the sharp upturn at very low- q . The differences between the two lots are most likely the result of either the shift in the molecular weight distribution or impurities in the polymer.

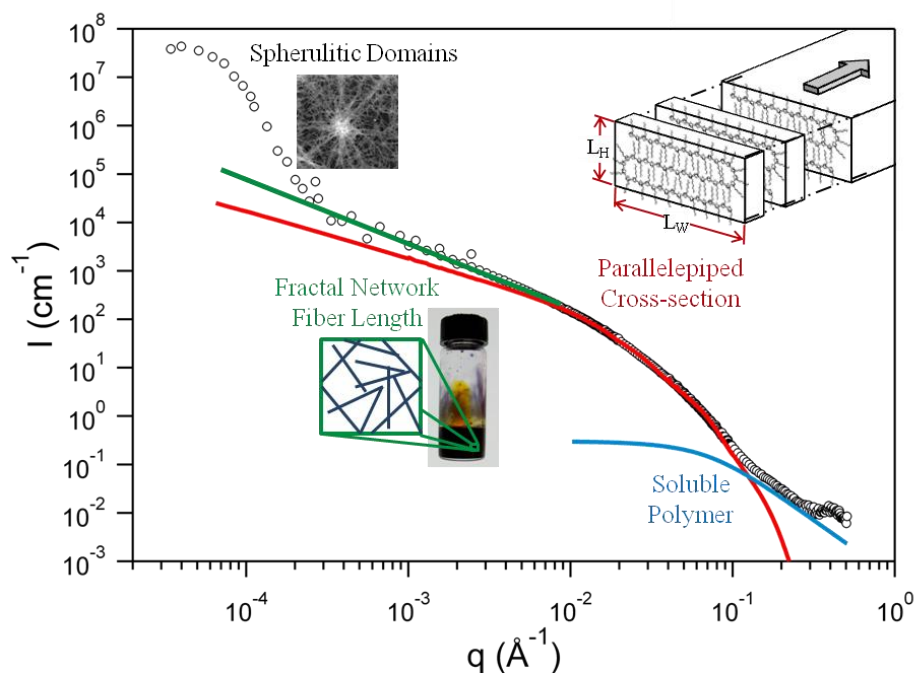


Figure 6.10: Characteristic combined SANS and desmeared USANS data from a 30 mg/mL P3HT-L1 gel in D10-p-xylene.

From Figure 6.10, it is clear that P3HT is a very complex system and many different structures must be accounted for at various length scales in order to fully

interpret the data. From both the literature and the sTEM images, it is determined that the cross-section of the fibers would be best fit with a parallelepiped model. However, this model only effectively fits the data for scattering vector, q , between $0.008 < q < 0.1 \text{ \AA}^{-1}$. At low- q , the model deviates from the scattering because the model only accounts for discrete isotropic fibers in dispersion. At $0.0001 < q < 0.008 \text{ \AA}^{-1}$ the scattering is dominated by the network structure of the gel, which accounts for the increased slope. A sharp upturn at low- q is indicative of the dense nucleation centers observed with the sTEM. At high- q , $q > 0.1 \text{ \AA}^{-1}$, scattering from the soluble polymer is significant relative to the scattering of the fibers. The soluble polymer is fit with an excluded volume polymer model. Finally, at $q \sim 0.3 \text{ \AA}^{-1}$ there is a small peak. The peak results from the periodic lamellar stacking of the alkyl chains and the thiophene backbones through the thickness of the fiber.

Fibrillar Cross-section

The combined parallelepiped and excluded volume polymer form factor described by Equations 2.17-2.19 are used to fit the scattering data from the P3HT gels with DANSE SansView software.³⁶ In this model, all parameters are fixed except for the cross-sectional dimensions L_H and L_W and the volume fraction of fibers. Because the lower- q limit to this fit is only 0.008 \AA^{-1} , the length is fixed at $100,000 \text{ \AA}$, which is larger than resolvable from SANS. Polydispersity factors are also used in fitting to account for the size distributions in fiber height, width, and length. The distribution is defined by a Gaussian function where the polydispersity factor is simply the ratio of one standard deviation to the mean dimension. The polydispersity factors for height, width, and length are held fixed for all fits at 0.35, 0.2, and 0.1 respectively.

Representative scattering curves are plotted with their corresponding fits in Figure 6.11. The combined model provides a very good fit to scattering over the relevant q -range. The cross-sectional dimensions, determined from the model fitting, are plotted on the left of Figure 6.11. The width of the fiber ranged between 22 and 26 nm, which is consistent with the sTEM micrographs. The thickness of the fibers formed in toluene and p-xylene is approximately 5 nm, which corresponds to P3HT lamellar sheets stacked with no alkyl chain intercalation. The thickness of a fiber formed in benzene is 6 nm, which is 20% larger than in toluene and p-xylene gels, increasing the likelihood that in any given fiber there will be four lamellar stacks of P3HT instead of three. The cross-sectional dimensions of the fiber are well fit with the parallelepiped form factor for individual fibers and agree with the reported morphology of P3HT in the literature.^{14, 18, 19}

The conversion of soluble P3HT to fibers is plotted in Figure 6.12. Only 50 to 60% of the P3HT forms fibers in the gel at room temperature ($T \sim 25$ °C), the remaining polymer is fully soluble even after several days. The solids fraction is relatively stable with respect to concentration, but is systematically higher for the xylene gels. A higher solids fraction will increase the charge mobility through the fiber network. The relative stability of solids fraction as a function of increasing concentration suggests that there may be a specific molecular weight fraction of the P3HT that remains fully soluble in each of the solvents.

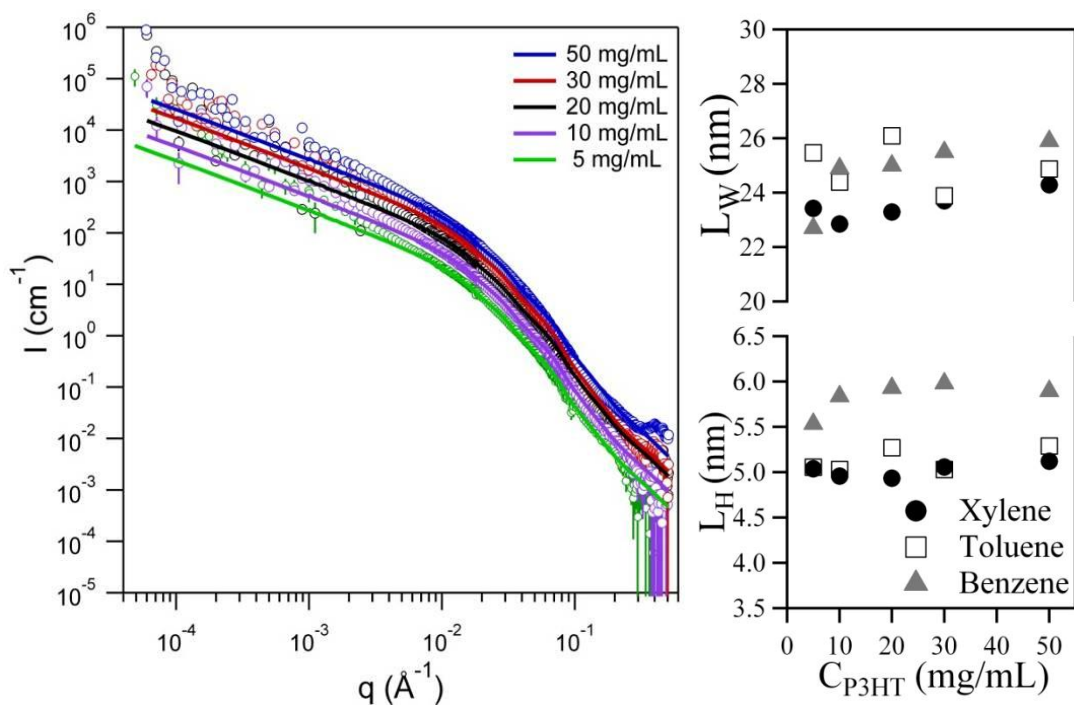


Figure 6.11: Right: combined model fits of the P3HT gels in p-xylene. Left: Cross-sectional dimensions for all gels.

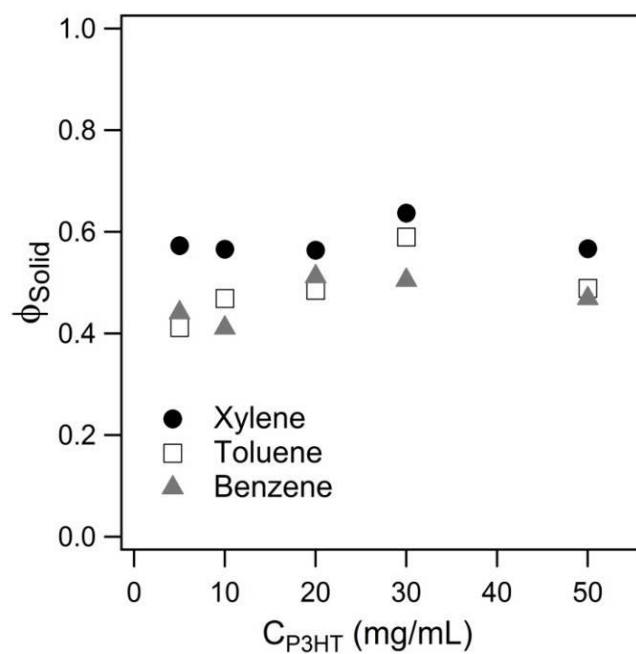


Figure 6.12: Fraction of P3HT converted to fibers during gelation.

To confirm this hypothesis, P3HT and xylene is gelled for 24 hours and before the remaining soluble fraction of P3HT is extracted by capping the gel with pure solvent and

waiting for the soluble polymer to diffuse into the liquid cap. The solvent cap is exchanged until it remains clear after sitting overnight. After the soluble polymer is removed, the soluble and fibrillar polymer samples are dried and then dissolved in chlorobenzene for GPC analysis. The results summarized in Table 7.1 confirm that the polymer partitions with high molecular weight polymer forming fibers and low molecular weight polymer remaining soluble.

Table 6.1: Molecular weight averages for P3HT-L2 batch polymer as purchased and partitioned into soluble and fibrillar polymer.

	M_w (Da)	M_w/M_N
P3HT-L2	16800	1.6
P3HT-Solid	24000	2.1
P3HT-Soluble	6800	1.9

Network Structure

As illustrated in Figures 6.10 and 6.11, the scattering at low- q deviates significantly from the parallelepiped-polymer combined model. This is because branching and networking of the fibers will cause the fractal dimension of the gel to deviate from the fractal dimension of a single fiber ($D_f=1$). In this region the intensity, $I(q)$, can be approximated by the structure factor, $S(q)$ which is related to the fractal dimension (D_f) of the network, Equation 6.3:

$$I(q) \approx S(q) \approx q^{-D_f} \quad \text{Equation 6.3}$$

An example of a fractal dimension power-law fit (left) and the results of the systematic evaluation of fractal dimension for all of the samples as a function of concentration (right) is shown in Figure 6.13. Gels containing at least 20 mg/mL P3HT have a consistent fractal dimension, $D_f \sim 1.4$. However, the fractal dimension for 10 and 5 mg/mL gels is lower. This can be attributed to local inhomogeneity in the structure.³⁷ It is

possible that in these low concentration gels, insufficient polymer is available and locally fiber-dense and fiber-poor regions form.

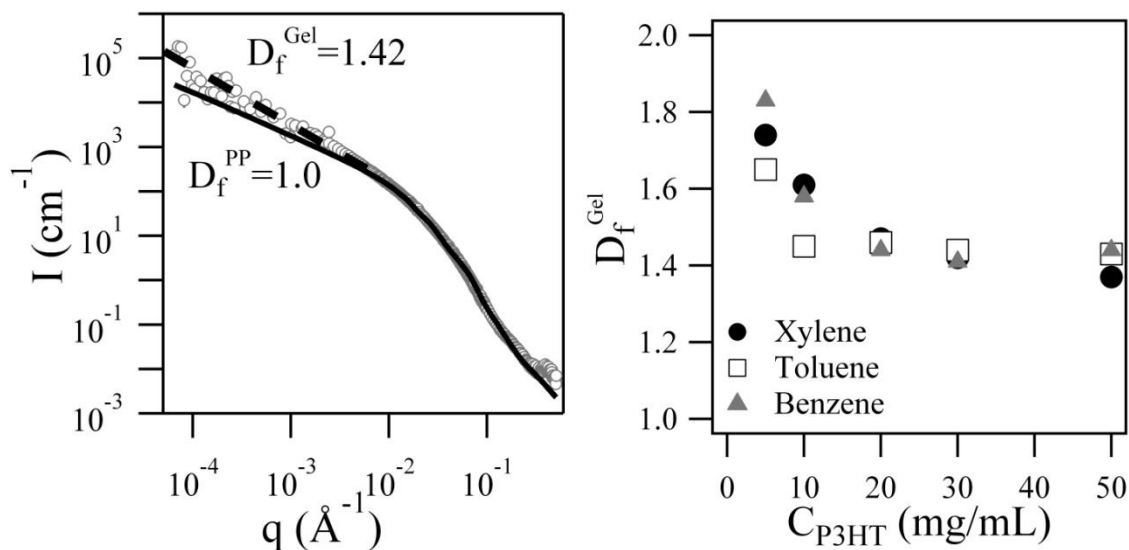


Figure 6.13: Left- Example of power law fit to determine fractal dimension. Right- Fractal dimension plotted as a function of concentration.

Discussion

A rigorous and systematic multiscale structural characterization of P3HT gels in benzene, toluene and p-xylene has been completed. Additionally, rheological characterization of P3HT gels is also presented. Interestingly, though the P3HT-xylene gels have the highest overall conversion from polymer to fibers, the elastic moduli of these gels are substantially lower than the comparable P3HT-benzene gels. P3HT-toluene gels have approximately the fiber fraction as the P3HT-benzene gels but are even weaker than the xylene gels. We expect that this may be due to the formation of thicker fibers in the P3HT-benzene gels. Thicker, more rigid, fibers may result in a stronger gel even though there are fewer fibers in these gels.

Electrical measurements performed by Newbloom et al. indicate that, like the mechanical properties, the conductivity of the P3HT gels is highly dependent on the solvent.³⁸ The conductivity of the P3HT-xylene gel is one to two orders of magnitude higher than the conductivity of comparable P3HT-benzene gels. The P3HT-toluene gel has only slightly weaker conductivity than the P3HT-xylene gel, which could be explained by the reduced fiber fraction. The origin of the differences in conductivity and mechanical properties between P3HT-benzene gels and the other P3HT gels remains unresolved. The results presented in this chapter lay the ground work for the rheoSANS study presented in Chapter 7 as well as ongoing work on the development of solution processable gel-based inks.

References

1. V. Avrutin, N. Izyumskaya and H. Morkoç, *Superlattices and Microstructures*, **49**, 337-364.
2. K. M. Coakley and M. D. McGehee, *Chemistry of Materials*, 2004, **16**, 4533-4542.
3. Z.-Q. Lin, N.-E. Shi, Y.-B. Li, D. Qiu, L. Zhang, J.-Y. Lin, J.-F. Zhao, C. Wang, L.-H. Xie and W. Huang, *Journal of Physical Chemistry C*, 2011, **115**, 4418-4424.
4. C.-Y. Chen, C.-S. Chang, S.-W. Huang, J.-H. Chen, H.-L. Chen, C.-I. Su and S.-A. Chen, *Macromolecules*, 2010, **43**, 4346-4354.
5. A. Nagai, J. Miyake, K. Kokado, Y. Nagata and Y. Chujo, *Journal of the American Chemical Society*, 2008, **130**, 15276-+.
6. S. Malik, T. Jana and A. K. Nandi, *Macromolecules*, 2001, **34**, 275-282.
7. P.-S. Wang, H.-H. Lu, C.-Y. Liu and S.-A. Chen, *Macromolecules*, 2008, **41**, 6500-6504.
8. Q. Bricaud, A. Cravino, P. Leriche and J. Roncali, *Solar Energy Materials and Solar Cells*, 2009, **93**, 1624-1629.
9. B. W. Boudouris, F. Molins, D. A. Blank, C. D. Frisbie and M. A. Hillmyer, *Macromolecules*, 2009, **42**, 4118-4126.
10. W. H. Baek, H. Yang, T. S. Yoon, C. J. Kang, H. H. Lee and Y. S. Kim, *Solar Energy Materials and Solar Cells*, 2009, **93**, 1263-1267.
11. J. A. Hauch, P. Schilinsky, S. A. Choulis, R. Childers, M. Biele and C. J. Brabec, *Solar Energy Materials and Solar Cells*, 2008, **92**, 727-731.

12. K. J. Ihn, J. Moulton and P. Smith, *Journal of Polymer Science Part B-Polymer Physics*, 1993, **31**, 735-742.
13. J. Jaczewska, A. Budkowski, A. Bernasik, E. Moons and J. Rysz, *Macromolecules*, 2008, **41**, 4802-4810.
14. W. D. Oosterbaan, V. Vrindts, S. Berson, S. Guillerez, O. Douheret, B. Ruttens, J. D'Haen, P. Adriaensens, J. Manca, L. Lutsen and D. Vanderzande, *Journal of Materials Chemistry*, 2009, **19**, 5424-5435.
15. Y. H. Chang, S. R. Tseng, C. Y. Chen, H. F. Meng, E. C. Chen, S. F. Horng and C. S. Hsu, *Organic Electronics*, 2009, **10**, 741-746.
16. T. A. Chen, X. M. Wu and R. D. Rieke, *Journal of the American Chemical Society*, 1995, **117**, 233-244.
17. H. Sirringhaus, P. J. Brown, R. H. Friend, M. M. Nielsen, K. Bechgaard, B. M. W. Langeveld-Voss, A. J. H. Spiering, R. A. J. Janssen and E. W. Meijer, 2000, pp. 129-132.
18. G. M. Newbloom, F. S. Kim, S. A. Jenekhe and D. C. Pozzo, *Macromolecules*, null-null.
19. C. Y. Chen, S. H. Chan, J. Y. Li, K. H. Wu, H. L. Chen, J. H. Chen, W. Y. Huang and S. A. Chen, *Macromolecules*, 2010, **43**, 7305-7311.
20. T. Kambayashi, H. Wada, M. Goto, T. Mori, B. Park, H. Takezoe and K. Ishikawa, *Organic Electronics*, 2006, **7**, 440-444.
21. J. M. Verilhac, G. LeBlevenec, D. Djurado, F. Rieutord, M. Chouiki, J. P. Travers and A. Pron, *Synthetic Metals*, 2006, **156**, 815-823.
22. M. Koppe, C. J. Brabec, S. Heiml, A. Schausberger, W. Duffy, M. Heeney and I. McCulloch, *Macromolecules*, 2009, **42**, 4661-4666.
23. X. N. Yang, J. Loos, S. C. Veenstra, W. J. H. Verhees, M. M. Wienk, J. M. Kroon, M. A. J. Michels and R. A. J. Janssen, *Nano Letters*, 2005, **5**, 579-583.
24. J. Zhao, A. Swinnen, G. Van Assche, J. Manca, D. Vanderzande and B. Van Mele, *Journal of Physical Chemistry B*, 2009, **113**, 1587-1591.
25. S. Malik, T. Jana and A. K. Nandi, *Macromolecules*, 2000, **34**, 275-282.
26. S. Malik and A. K. Nandi, *Journal of Polymer Science Part B: Polymer Physics*, 2002, **40**, 2073-2085.
27. S. Malik and A. K. Nandi, *The Journal of Physical Chemistry B*, 2003, **108**, 597-604.
28. S. Malik and A. K. Nandi, *Journal of Applied Polymer Science*, 2007, **103**, 2528-2537.
29. J. R. Richards, Weigandt, K.M, Pozzo, D.C., *Future Publication*, 2011.
30. W. Y. Huang, P. T. Huang, Y. K. Han, C. C. Lee, T. L. Hsieh and M. Y. Chang, *Macromolecules*, 2008, **41**, 7485-7489.
31. P.-T. Huang, Y.-S. Chang and C.-W. Chou, *Journal of Applied Polymer Science*, 2011, n/a-n/a.
32. M. D. Abramoff, Magalhaes, P. J. and Ram, S.J., , *Biophotonics International*, 2004, **11**, 36-42.
33. C. J. Glinka, J. G. Barker, B. Hammouda, S. Krueger, J. J. Moyer and W. J. Orts, *J. Appl. Crystallogr.*, 1998, **31**, 430-445.
34. S. R. Kline, *J. Appl. Crystallogr.*, 2006, **39**, 895-900.

35. J. G. Barker, C. J. Glinka, J. J. Moyer, M. H. Kim, A. R. Drews and M. Agamalian, *J. Appl. Crystallogr.*, 2005, **38**, 1004-1011.
36. <http://danse.chem.utk.edu/sansview.html>, SANSVIEW,
37. A. M. Hecht, R. Duplessix and E. Geissler, *Macromolecules*, 1985, **18**, 2167-2173.
38. G. M. Newbloom, K. M. Weigandt and D. C. Pozzo, *Macromolecules*, 2012, **45**, 3452-3462.

Chapter 7

RheoSANS Investigation of the Structural and Mechanical Evolution of P3HT during Gelation and Dissolution

Introduction

Poly(3-hexylthiophene) (P3HT) gelation is seldom reported on in the literature. This is largely because gelation has, as a general rule, been regarded as detrimental to solution based processing methods¹. In Chapter 6, we make the case that the formation of a self-assembled bifurcating network of fibers, which is characteristic of P3HT gelation, may actually be favorable for the development of bulk heterojunctions. This is because the interconnected structure of the P3HT gel meets many of the requirements for the idealized morphology proposed by Coakley and McGehee.^{2, 3} In fact, films generated from P3HT networks have been shown to have much higher conductivity than traditional solution processed films.^{3, 4} Furthermore, new developments toward gel processability make these gels a promising material for organic electronic devices.⁵⁻⁷

In two separate studies P3HT gels have been utilized in functioning organic solar cells.^{5, 7} Two methods of preparation, freeze drying of gels and formation of gel dispersions with sonication and subsequent solution processing, were used to prepare gel-based organic photovoltaic devices (OPVs) with power conversions efficiencies of 1.47% and 0.18% respectively. While the reported efficiencies are well below the industry record (reportedly over 10%), these fabrication methods are in their infancy and significant improvements are likely to occur in the near future.⁸ In fact, in one very recent study the use of a nanostructured interface in a P3HT-C60 OPV is shown to improve device efficiency by ~30% over a comparable device with a smooth P3HT-C60 interface.⁹ Given these recent advances in gel processing for organic electronics, understanding and developing structure-property relationships in conjugated polymer gels has become critically important.

Several groups have reported on the gelation of conjugated polymers in various organic solvents.^{1, 4, 10-14} In a 2001 study by Nandi and colleagues, it is suggested that gelation of P3HT occurs in a two step process. First P3HT undergoes a coil to rod transition as the solvent quality is reduced. Subsequently, the now rod-like polymer crystallizes and forms the network.⁴ Recently, two publications have revisited the gelation mechanism of P3HT.^{1, 15} The mechanism proposed by Koppe is very similar to the original Nandi mechanism with a coil-to-rod transition followed by an aggregation step.¹ However, in the Koppe mechanism, the nature of the aggregation is not specific. Here, they state that the polymer begins to aggregate and the subsequently physical interaction between aggregates leads to gelation. More recently, Xu and colleagues suggested that, prior to gelation, P3HT forms single fibers (un-branched) that

subsequently aggregate at some critical fiber concentration and form a percolating gel network.¹⁵ In this chapter, we propose a distinct gelation mechanism based on simultaneous mechanical and structural characterization of P3HT during gelation and dissolution.

It has been previously established that the structure of thermoreversible gels formed from small molecules and polymers can be adjusted by varying the self-assembly conditions.¹⁶⁻¹⁸ Adjusting the cooling rate, or changing the solvent quality can lead to dramatically different structural features in the gels. In dilute P3HT solutions and gels, simply switching between various aromatic solvents has been shown to change both the fibrillar and network structures.^{3, 19} To better understand how these structural variations arise, it is necessary to characterize the evolving structure of these gels. The structure of conjugated gels has been studied with a variety of techniques including scanning electron microscopy (SEM), transmission electron microscopy (TEM), atomic force microscopy (AFM) as well as small angle x-ray and neutron scattering (SAXS and SANS).^{3, 7, 20, 21} However, only with small angle scattering can the structure of the gel be evaluated *in situ* during gelation.

In this chapter, rheoSANS experiments are used to simultaneously characterize the mechanical and structural properties of P3HT gels formed in deuterated organic solvents. Additionally, the results from some complementary conductivity-SANS measurements are also reported. By combining these techniques, we are able to track the evolution of structural-mechanical and structural-electrical properties of these gels during gelation and dissolution as a function of decreasing and increasing temperature respectively. The results of these experiments suggest a more specific mechanism for the

formation of these gels than presented previously in the literature. Furthermore, based on this data, we also propose a dissolution mechanism that is quite distinct from the gelation mechanism and explains the dramatic hysteresis in the rheological and electrical properties during gelation and.

Materials and Method

Materials and Sample Preparation

Sepiolid P200 poly(3-hexylthiophene) (Lot# 22.10.2009) with 98% regioregularity is purchased from Rieke Metals (Lincoln, NE). The molecular weight distribution is measured with gel permeation chromatography (GPC) against a polystyrene standard in chlorobenzene. The number average molecular weight is found to be 16,770 g/mol with a polydispersity index of 1.6. P-xylene, toluene and benzene are purchased from Sigma-Aldrich (St. Louis, MO). D10-p-xylene (D>98%), D8-toluene (D>99.5%) and D6-benzene (D>99.5%) are purchased from Cambridge Isotopes (Andover, MA) and used for all neutron scattering experiments. Gels are prepared at a concentration of 30 mg/mL P3HT in each of the solvents. The polymer and solvent are mixed and heated at 80°C until the solution is a uniformly orange with no visible undissolved polymer.

RheoSANS

RheoSANS measurements are performed at the NIST Center for Neutron Research (NCNR) in Gaithersburg, MD on the NG7 30 m SANS instrument. An MCR 501 Anton Paar Rheometer is placed in the beam and aligned for radial measurements through the 1-3 plane. A titanium concentric cylinder geometry with a $R=14.5 \text{ mm} \times L=$

36 mm bob and a 0.5 mm gap is utilized for all RheoSANS measurements reported in this chapter. Additional details about the RheoSANS set up are located in Chapter 2. The rheometer and gel are preheated to 80°C prior to sample loading. Approximately 4 mL of solubilized P3HT solution is loaded into the rheometer and sealed against evaporation with a solvent trap by using a low viscosity non-volatile silicone oil. The temperature is held at 80°C for ~10 minutes prior to measurement to ensure that the polymer is fully dissolved.

To conserve scattering time the solution is cooled to a pre-experiment temperature known to be well above the gelation temperature of the solution for each solvent. The pre-experiment temperature is 65 °C, 60 °C, and 50 °C for D10-p-xylene, D8-toluene and D6-benzene respectively. Gelation is induced with a gradual decrease in temperature at a rate of 0.8 °C/min. Small amplitude oscillations of 1% strain at a frequency of 1 Hz are used to track the evolving mechanical properties at temperatures known to be above the gelation temperature. The oscillatory strain amplitude is reduced to 0.25% strain near the gelation temperature. This strain is just below the linear-viscoelastic limit of the P3HT gel ($\gamma_{LVE} \sim 0.5\%$). The gels are cooled beyond the gelation temperature to 15 °C, 9 °C and 10 °C for D10-p-xylene, D8-toluene and D6-benzene respectively. The minimum temperature reached in the D10-p-xylene P3HT gels is constrained by the freezing temperature of the solvent (13.5 °C). After gelation, the samples are reheated at 0.8 °C/min and the mechanical properties are tracked using 0.25% strain oscillations at 1 Hz until dissolution is achieved as indicated by the absence of a measurable elastic modulus. The temperature cycle is completed twice for each sample (except the P3HT-benzene gel).

The temperature cycle is repeated in order to enable structural measurements at two SANS instrument configurations. One scattering file is collected for each rheometer measurement and corresponds to a 1 °C change in the sample temperature. High- q scattering ($0.0131 < q < 0.2 \text{ \AA}^{-1}$) is measured at a sample to detector distance of 3 m with 6 Å neutrons. Low- q scattering is measured with one of two possible configurations. A q -range between $0.0035 < q < 0.04 \text{ \AA}^{-1}$ is measured at a sample to detector distance of 13 m using 6 Å neutrons. Even lower- q ($0.001 < q < 0.01 \text{ \AA}^{-1}$) is probed using a 15.8 m sample detector distance with 8 Å neutrons and neutron focusing lenses; however, the neutron flux is low with this configuration and leads to excessively noisy data. Therefore, this lowest- q configuration is only used once during the heating ramp on the D10-xylene P3HT gel. All of the SANS data are corrected for background and sample cell scattering and placed on an absolute scale by measuring the direct beam flux.²² The data is reduced and desmeared using the NIST Igor based software.²²

Dielectric-SANS

Complementary conductivity-SANS measurements are performed by Greg Newbloom at the high flux isotope reactor on the CG2 SANS instrument located at Oakridge National Labs in Oakridge, Tennessee. For these measurements, an Agilent e4980a Precision LCR meter is used to measure the conductivity with AC measurements at a frequency of 2 kHz and an applied voltage of $V_{AC}=200 \text{ mV}$, which is within the linear impedance response region. These measurements are made in a specially designed conductivity-SANS cell with Peltier block as described in Chapter 2. As with the RheoSANS, the polymer solution is loaded hot, sealed and then heated to 80 °C to ensure full polymer dissolution. The solution is cooled at a rate of 0.8 °C/min and then reheated

at a rate of 1.2 °C/min. The discrepancy in the reheating rates used in the conductivity-SANS and rheoSANS measurements seem to have no effect on the dissolution of the gel as a function of temperature. Scattering is measured at two sample to detector distances to measure q between $0.002 < q < 0.2 \text{ \AA}^{-1}$. Scattering files are measured at two minute intervals and matched to simultaneously collected temperature and conductivity data. The scattering data is corrected for background and empty cell scattering and placed on absolute scale using NIST Igor based software.²³ The conductivity measurements from this experiment are normalized because the surface resistivity of the aluminum can fluctuate due to variations in surface roughness caused by polishing and formation of an oxide layer over short time periods.

Results

P3HT at a concentration of 30 mg/mL is dissolved in deuterated p-xylene, toluene, and benzene by heating to ~80°C. Based on the results in Chapter 6, we expect that upon cooling, the reduced solubility will drive polymer self-assembly into semi-crystalline P3HT fiber networks and ultimately the formation of an organogel. These gels are relatively strong below a linear viscoelastic limit of ~0.5% strain, but have a very low yield stress and are easily damaged. Here, we have used rheoSANS to simultaneously characterize the structural and mechanical properties of P3HT organogels during gelation and dissolution through cooling and heating ramps. The mechanical properties are measured directly through small amplitude 0.25% strain oscillations as the temperature is gradually cooled and then reheated at a rate of 0.8°C/min. In Figure 7.1 the elastic and viscous moduli are plotted as a function of temperature.

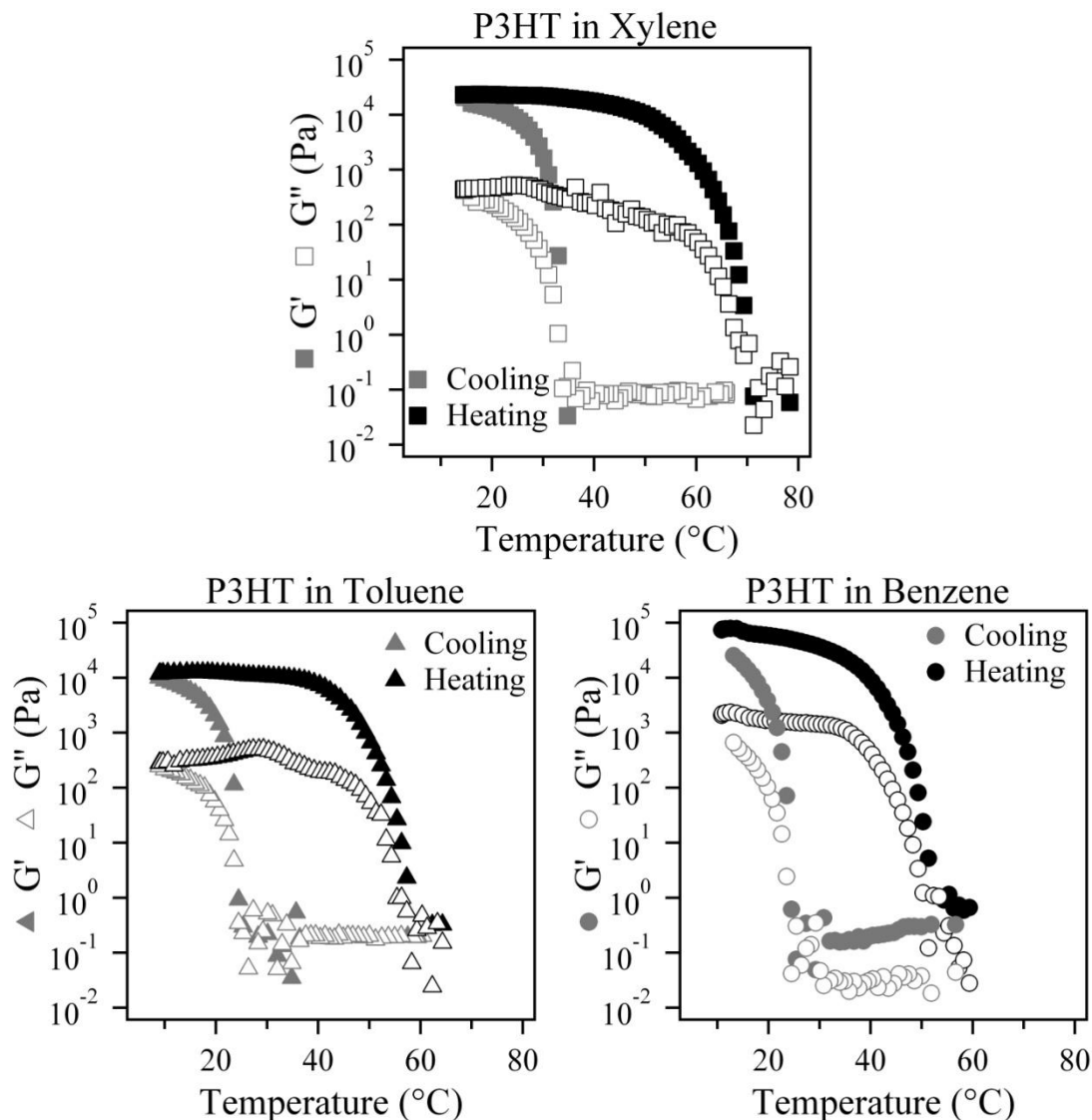


Figure 7.1: The viscous and elastic moduli of 30 mg/mL P3HT gels in xylene, toluene and benzene plotted as a function of temperature.

The gelation (T_g) and dissolution (T_d) temperatures are determined from the cross-over of the elastic and viscous moduli. Prior to gelation, the P3HT-solvent solution should have no measurable elasticity, such that $G'=0$. In some cases, either do to noise or external friction (as in the case of the benzene gel), a small elastic modulus is measured prior to gelation. As the fibers form and gelation occurs, the elastic modulus begins to rapidly rise and becomes greater than the viscous modulus. The temperature at which this cross-over occurs is the gelation temperature. Each of the gels examined in this study

have different gelation and dissolution temperatures. The elastic modulus is also highly dependent on the solvent. Based on data presented in Chapter 6, we have already confirmed that these samples are true gels over a wide range of frequency. The gelation and dissolution temperatures and the maximum elastic modulus are reported in Table 7.1. Note, that G'_{max} of the p-xylene gel is twice G'_{max} of the toluene gel, but about one third of G'_{max} for the benzene gel. This dramatic difference likely arises from differences in the structure of the gels.

Table 7.1: Rheology parameters from rheoSANS experiment.

	T_g (°C)	T_d (°C)	G'_{max} (Pa)
Xylene	32.9	70.3	23,600
Toluene	23.5	58.3	12,500
Benzene	23.5	52.3	79,000

The structure of the forming P3HT gels is probed directly in the rheometer with small angle neutron scattering. The rheometer and the SANS instrument are controlled such that one scattering file is obtained for each rheology point. This allows direct comparison between the mechanical and structural properties of these gels. In each scattering file, data is collected for approximately one minute. The data is reduced to correct for background radiation and the sample cell scattering and put into absolute scale. The reduced scattering data from the toluene gel during gelation and dissolution are plotted in Figures 7.2 and 7.3 respectively. In both plots, the lowest intensity scattering spectra is a soluble polymer file that has been averaged over a wide temperature range in order to enhance the scattering statistics and reduce noise of this low intensity sample. The scattering from the toluene gels at intermediate- and high- q ($q > 0.01 \text{ \AA}^{-1}$) is reflective

of the scattering data obtained for each of the gels. Due to time constraints low- q data is not obtained for all of the gels.

From the reduced scattering data we find that a percolated fiber network is formed almost instantaneously upon the onset of fiber formation. From Table 7.1, the gelation temperature for P3HT in toluene is 23.5 °C ($G'=114$ Pa) and in Figure 7.2 the corresponding scattering data is shown to be nearly overlapping with the soluble polymer scattering. Similarly, weak scattering is observed just prior to dissolution. Interestingly, dissolution occurs over an extended temperature range when compared to gelation, which suggests that the mechanism for dissolution of the fibers is distinct from the formation of fibers. To truly compare the structural and mechanical properties of these gels, additional analysis of the scattering data is necessary.

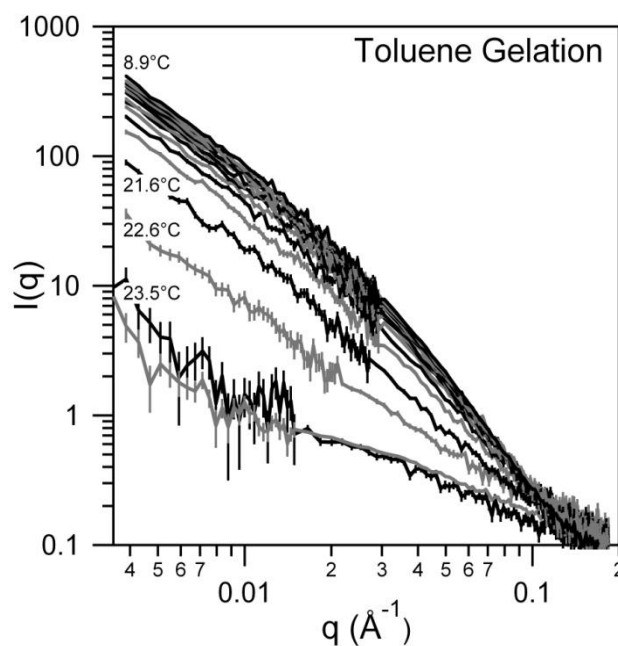


Figure 7.2: Reduced scattering data of a P3HT in toluene gel at 1 °C intervals during cooling. The scattering intensity increases as the gel forms during the cooling ramp.

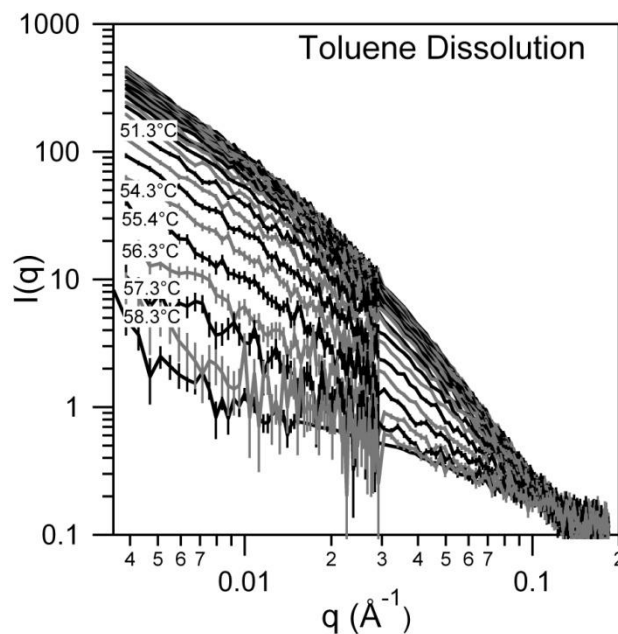


Figure 7.3: Reduced scattering data from a P3HT in toluene gel at 1 °C intervals during heating. The scattering intensity decreases as the gel dissolves during the heating ramp.

Recall from Chapter 2 that for scattering data in absolute scale, $I(q)$ can be modeled as the product of the form factor, structure factor, and a scale factor that accounts for the particle volume fraction and scattering contrast. Poly(3-hexylthiophene) gels are effectively three component systems where the scattering from the soluble polymer and the self-assembled fibrillar polymer must be accounted for separately. Here we model the polymer with the excluded volume polymer form factor ($P_{PEX}(q)$) as described in Equation 2.18 and the P3HT fibers with the parallelepiped form factor ($P_{PP}(q)$) as described in Equation 2.17. A model that accounts for the additive scattering from each of these components is described by the mass balance:

$$I(q) = \phi_{P3HT} \Phi_F (\Delta\rho_{SLD})^2 P_{PP}(q) + \phi_{P3HT} (1 - \Phi_F) (\Delta\rho_{SLD})^2 P_{PEX}(q) \quad \text{Equation 2.19}$$

where, ϕ_{P3HT} is the volume fraction of P3HT in solution, Φ_F is fraction of P3HT that is self-assembled into fibers and $\Delta\rho_{SLD}$ is the contrast between either the fibers or the soluble polymer and the solvent.

In Chapter 6, we found that the scattering length density of the P3HT fibers is $1.07 \times 10^{-6} \pm 0.10 \times 10^{-6} \text{ \AA}^{-1}$. The scattering length density of the soluble polymer is calculated based on the molecular composition, the mass-density and the scattering lengths (listed in Table A1.1 in Appendix 1) with the Equation 2.2. The scattering length density of the soluble polymer is $0.676 \times 10^{-6} \text{ \AA}^{-1}$. The discrepancy between the scattering length density of the soluble P3HT and the P3HT fibers is due to the entrainment of the highly deuterated solvent in the fiber structure.

The mass-density of the liquid phase varies significantly throughout the rheoSANS experiment as the gels are cooled and then subsequently reheated. For example, the density of D10-p-xylene decreases from 0.950 g/mL at 14.5 °C to 0.896 g/mL at 70.0 °C during the heating ramp. Several parameters are affected by the temperature variation including the volume fractions of the soluble polymer and fibers, the scattering length density of the solvent, and the incoherent background that arises from inelastic scattering. Over the 55 °C temperature increase, the scattering length density of D10-p-xylene decreases from 5.81×10^{-6} to $5.48 \times 10^{-6} \text{ \AA}^{-2}$, a nearly 6% difference. Similarly, the incoherent background also decreases by ~6% during the temperature ramp. While this difference may seem small, it can significantly impact the fitting results. We have accounted for this variation by measuring the mass-density of each of the deuterated solvents as a function of temperature with an Anton Paar DMA 5000 density meter and subsequently calculating the incoherent background, scattering

length density, and scale factors as a function of temperature. Equations for the mass-density of the deuterated solvents as a function of temperature are reported in Appendix 1, Table A1.2.

To further constrain our model, we assume that the composition of the dissolved polymer does not change substantially during gelation. The scattering from the fully solubilized polymer in each of the solvents is fit with the excluded volume polymer form factor. When applying the combined model to the scattering measured during gelation, the results of this initial fit are held constant with the exception of the scale parameter which is varied to account for the conversion of soluble polymer to fibers. GPC measurements have indicated that there is some molecular weight partitioning during gelation, which would affect the model parameters so the assumption that the fully soluble polymer scattering accounts for the remaining soluble polymer during gelation is not entirely realistic. Still, we have found this to be a reasonable approximation on which to base the analysis.

From the soluble polymer data fit we find the chain conformation parameter, ν , to be 0.7 ± 0.04 , which is reasonable for conjugated polymers in solution. In general, $\nu=1$ would represent fully extended chains, and a value of $\nu=0.6$ is expected for an excluded volume chain. The radius of gyration, R_g , is determined from the fit with Equation 7.1:

$$R_g^2 = \frac{a^2 n^{2\nu}}{(2\nu+1)(2\nu+2)} \quad \text{Equation 7.1}$$

where a , n and ν are parameters associated with the excluded volume polymer form factor described in Equation 2.17. The radius of gyration of the polymer is found to be 53 ± 4 Å regardless of the solvent used. Additionally, the molecular weight (MW) is

determined directly from the scattering with an extrapolation of the absolute scattering intensity to zero- q ($I(q=0)$) with Equation 7.2:²⁴

$$MW = \frac{N_A (\rho_m)^2 I(q=0)}{C (\Delta\rho_{SLD})^2} \quad \text{Equation 7.2}$$

where N_A is Avagadro's number, ρ_m is the mass density of P3HT (1.1 mg/mL), C is the polymer concentration and $\Delta\rho_{SLD}$ is the scattering contrast between the polymer and solvent. From this calculation, the molecular weight was found to be 8,500 g/mol. This is approximately half of what was measured with GPC against the polystyrene standard (16,800 g/mol), but this difference is expected as a result of error in the GPC characterization that arises from the reduced flexibility of the conjugated polymer relative to polystyrene.²⁵

With these additional constraints imposed on the soluble polymer fitting coefficients, only three fitting parameters remain unconstrained: the fiber width, the fiber height, and the fraction of polymer self-assembled into fibers. The model is fit to the data using the DANSE SansView package with a simple least squares fitting algorithm.²⁶ The models are adjusted to account for instrumental smearing. Furthermore, to achieve a good fit, it is necessary to account for some polydispersity in the fiber height. A polydispersity index (PD) of 0.35 with a Gaussian distribution is sufficient to account for the polydispersity in the fiber thickness. The polydispersity index is equal to the ratio of one standard deviation to the average fiber thickness. Figure 7.4 shows the fitting results for several scattering curves from P3HT in toluene during gelation. Additionally, the fully soluble scattering and fit and the predicted scattering for the limiting case where the polymer is fully converted to fibers is also included in this plot. The accuracy of the fits

presented for these example data files is characteristic of the fitting quality for all of the gels presented in this chapter.

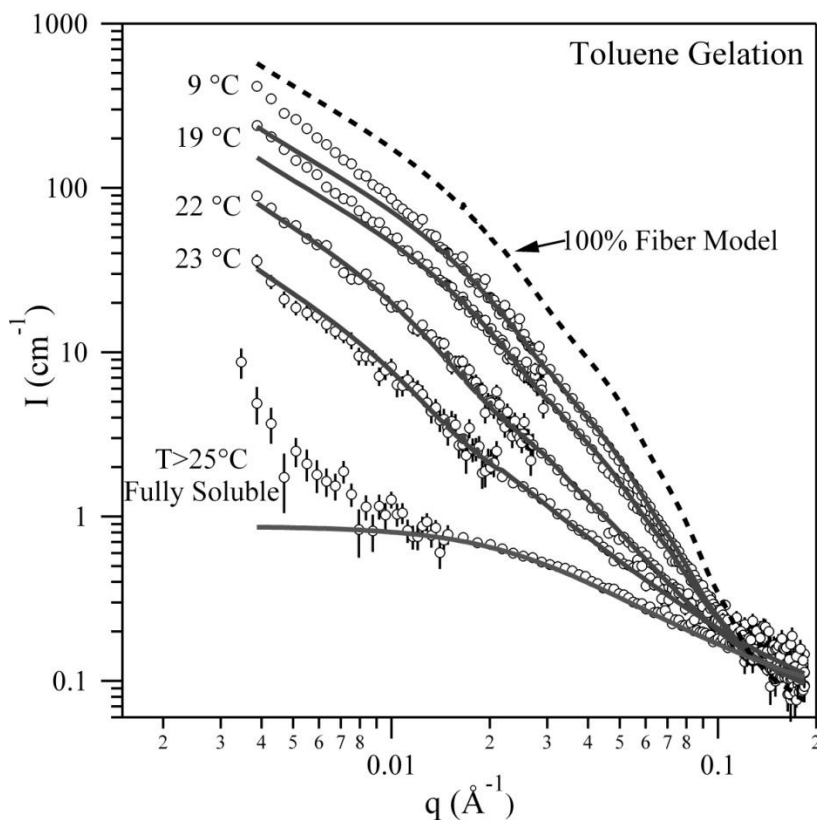


Figure 7.4: Selected scattering files from toluene gelation (\circ) fit with combined parallelepiped-excluded volume polymer model (- -). The dashed line represents the expected scattering from a theoretical gel where all of the soluble P3HT self-assembles into fibers.

Here it is shown that the combined model accurately accounts for the scattering intensity in all of the fiber containing samples at $q > 0.01 \text{ \AA}^{-1}$. Beyond this limit, the model generally underestimates the scattering observed from the evolving gel. This deviation, which is also observed in the fully formed P3HT gels of various concentrations in Chapter 6 and the fibrin gels in Chapter 3, is the result of the fractality of the fiber network and can typically be characterized by a fractal dimension. Because low- q data is not

obtained for all rheoSANS measurements and the scattering at low- q is noisy at the short scattering intervals used for this experiment, the fractal dimension is not extracted from this data. However based on the dielectric-SANS measurements, the fractal dimension is found to be ~ 1.45 for all of the gels regardless of concentration or temperature.³

The fitted parameters (height, width, and conversion fraction) for the gels formed in each organic solvent during both the heating and cooling ramps are plotted in Figure 7.5. When the gel first begins to form, the fiber volume fraction is so small the scattering model cannot be used to accurately fit the fiber dimensions. For this reason, the fitted parameters are only reported for $\Phi_F > 0.05$. The polymer conversion reaches 0.05 at 32 °C, 22.6 °C and 21.7 °C, or approximately 1-2 °C beyond the sol-gel transition, in the deuterated p-xylene, toluene, and benzene respectively. In all cases the polymer-fiber conversion proceeds rapidly upon onset and then gradually slows as the minimum temperature is approached. The maximum fiber conversion fraction in each gel is 0.54, 0.46 and 0.46 in the p-xylene, toluene and benzene respectively. Upon reheating, the polymer-fiber conversion gradually increases or remains unchanged until some critical temperature is reached, between 30 and 40°C, and the fibers begin to disassemble.

The fiber width remains relatively stable during the gelation and dissolution of the P3HT gels and is ~ 20 nm regardless of the solvent. This width roughly corresponds to the length of the average molecular weight P3HT molecule when fully extended. It should be noted that the width decreases very slightly during at the onset of fiber formation and then increases slightly near full dissolution. This may be related to the molecular weight partitioning as measured by GPC. It is possible that the highest molecular weight P3HT chains are first to self-assemble and last to disassemble.

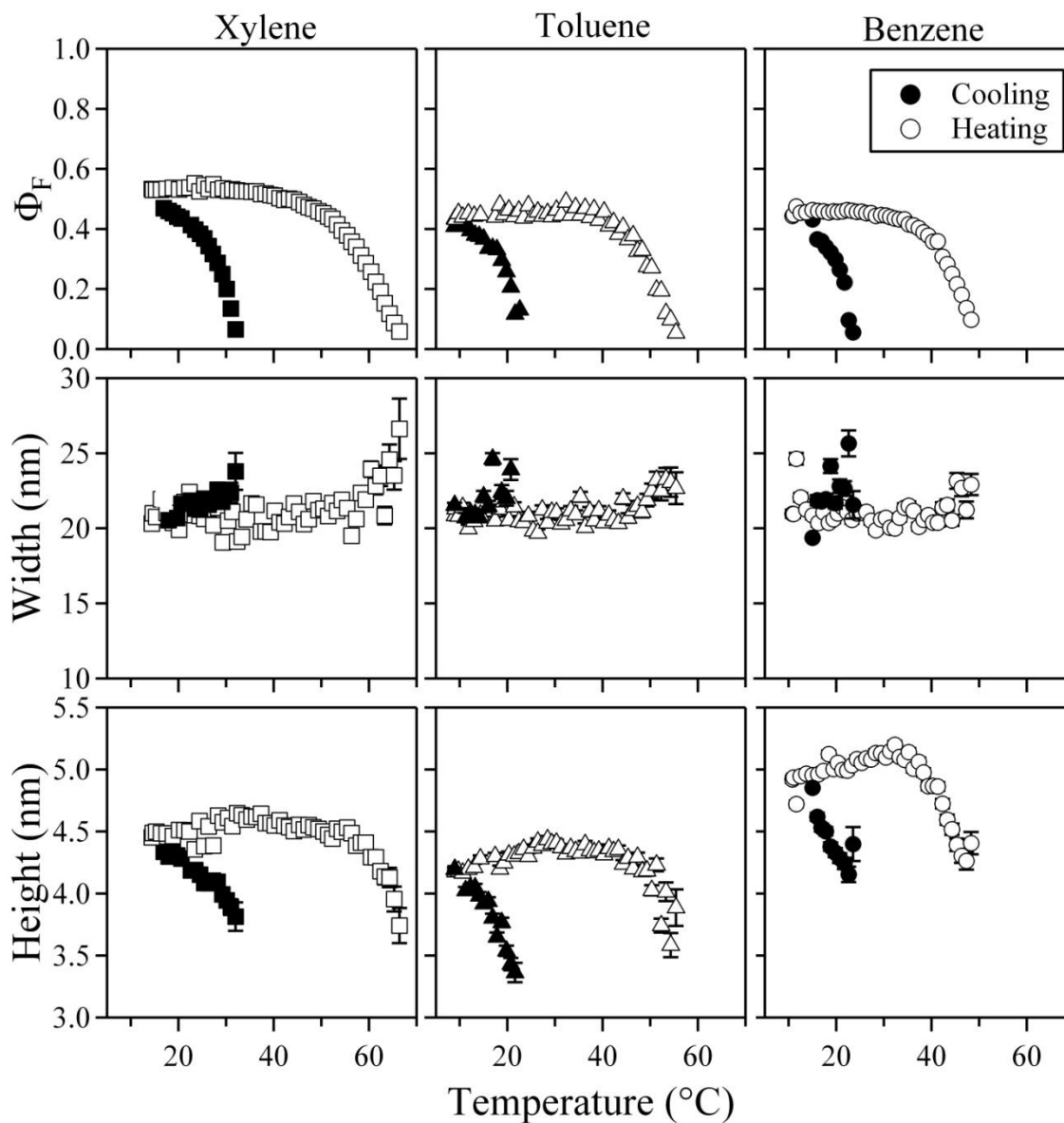


Figure 7.5: Fitting results (width, height, and fiber conversion fraction) for 30 mg/mL fibrin gels formed in deuterated xylene, toluene and benzene as a function of temperature during gelation and dissolution.

While the width of the fiber is relatively constant, the fiber thickness varies significantly both as a function of temperature and between solvents. The maximum thickness of the fibers during the temperature cycle typically occurs between 30 and 40 °C, which corresponds the onset of fiber dissolution. The maximum fiber height is 46.47,

44.4, and 51.2 nm in the p-xylene, toluene, and benzene respectively. Here the fibers formed in benzene are ~10% thicker than the fibers formed in the xylene and toluene.

The specific surface area of the fibers as a function of temperature is determined using Equations 2.9 and 2.10 from Chapter 2. In this case, because the soluble polymer contributes significantly to the high- q scattering for gels with low Φ_F , the specific surface area cannot be applied directly to the reduced data. First the scattering contribution from the soluble polymer and the incoherent background must be subtracted from the reduced data file in order to isolate the scattering from the fibers. The result of this subtraction for a toluene gel with $\Phi_F=0.3$ is plotted in Figure 7.6 (left). Notice, that the high- q scattering has a $I(q)\propto q^4$ dependence, which is characteristic of the sharp interface between the fibers and the solvent. This dependence is highlighted by the Porod plot in Figure 7.6 (right), and the $\lim_{q\rightarrow\infty}[I(q)\cdot q^4]$ is found to be 1.21×10^{-5} . This parameter is related to the surface area per volume ratio of fibers within the gel. The specific surface area in units of m^2/g fibrillar P3HT is determined from Φ_F and the sample composition. The specific surface area is plotted in Figure 7.7. In this plot the error bars are determined from the fitting uncertainty in determining the $\lim_{q\rightarrow\infty}[I(q)\cdot q^4]$.

Because the specific surface area is calculated based on the fibrillar polymer and not the total sample polymer, the reported values are reflective of the specific surface area of the fibers and not the overall sample. Here, we find that the specific surface area of the fibers is between ~600 and 1000 m^2/g for all samples. Furthermore, during the cooling ramp S_v decreases at least 100 m^2/g for every gel, which reflects the growing fiber height. Toluene gels have fibers with the highest specific surface area, where benzene gels have the lowest specific surface area. The specific surface area is directly

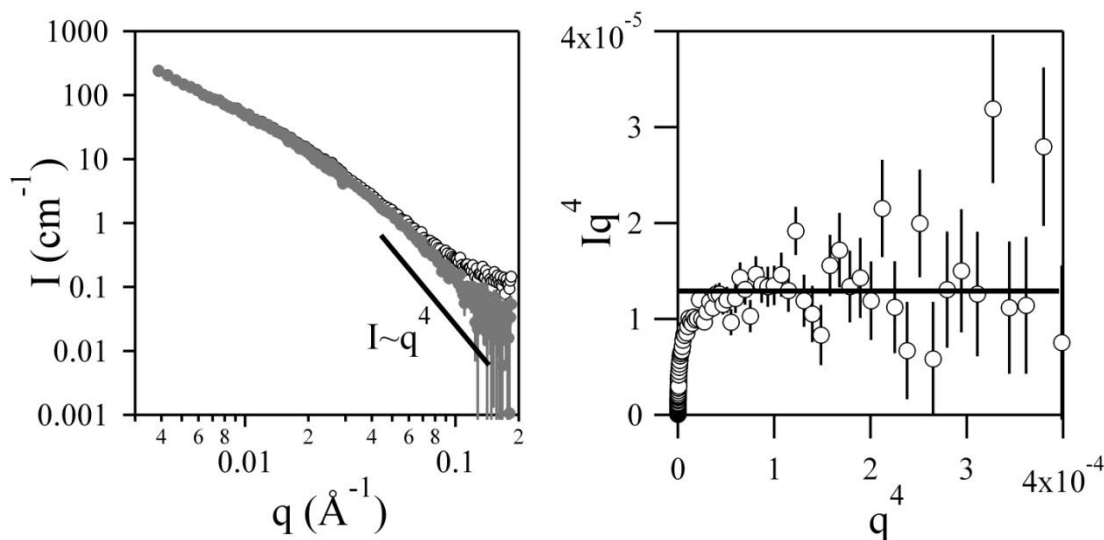


Figure 7.6: (Left) Reduced scattering data from P3HT-toluene gel with $\Phi_F = 0.3$ before and after subtraction of soluble polymer scattering and incoherent background. (Right) Porod plot for scattering from only fibers.

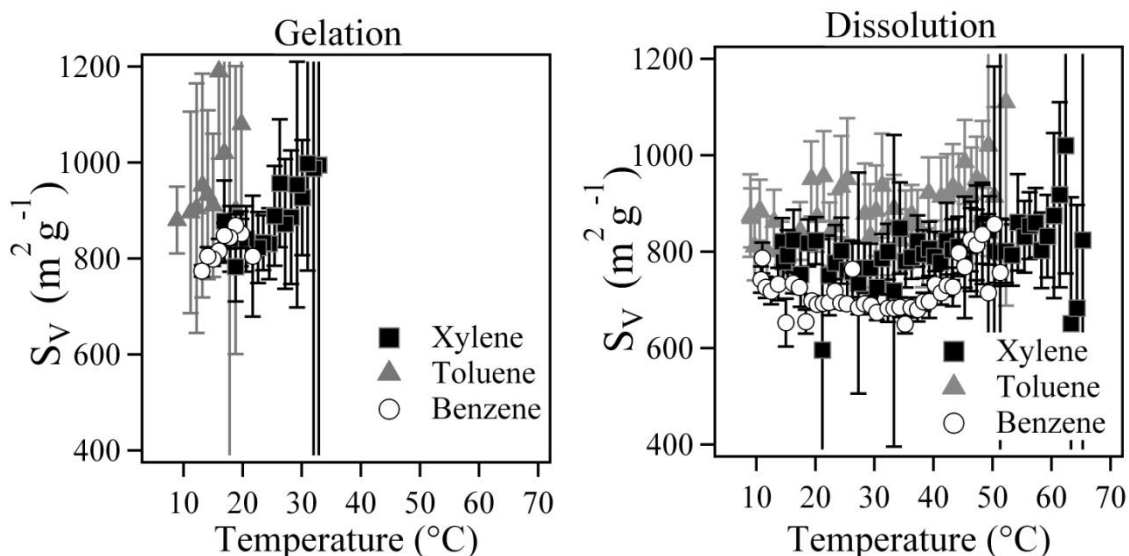


Figure 7.7: Specific surface area of fibers in P3HT gels plotted as a function of temperature. The error bars are determined from the fitting uncertainty.

related to the shape of the fibers, where $S_V \propto a^{-1} + b^{-1}$. Therefore, these results are consistent with the fiber cross-section dimensions as determined from the model fitting where the fiber height increased during gelation in all gels and was greatest in the benzene gels. Regardless of the variability, both between the gels and during gelation, all of these gels

contain fibers with high specific surface area as required for charge separation in OPV devices.

The fiber volume fraction is calculated based on the sample composition and the polymer-fiber conversion. The rheology for the toluene gel is re-plotted on the same graph with the fiber volume fraction in Figure 7.8 and is representative of all three gels. As mentioned previously, mechanical percolation occurs nearly simultaneously with fiber formation (within the same one minute measurement interval). Additionally, from complementary dielectric measurements it was found that electrical percolation also occurs simultaneously the fiber formation.²⁷ This is especially interesting given the very low fiber fraction at the onset of mechanical percolation, less than 0.001, for all of the gels probed in this study.

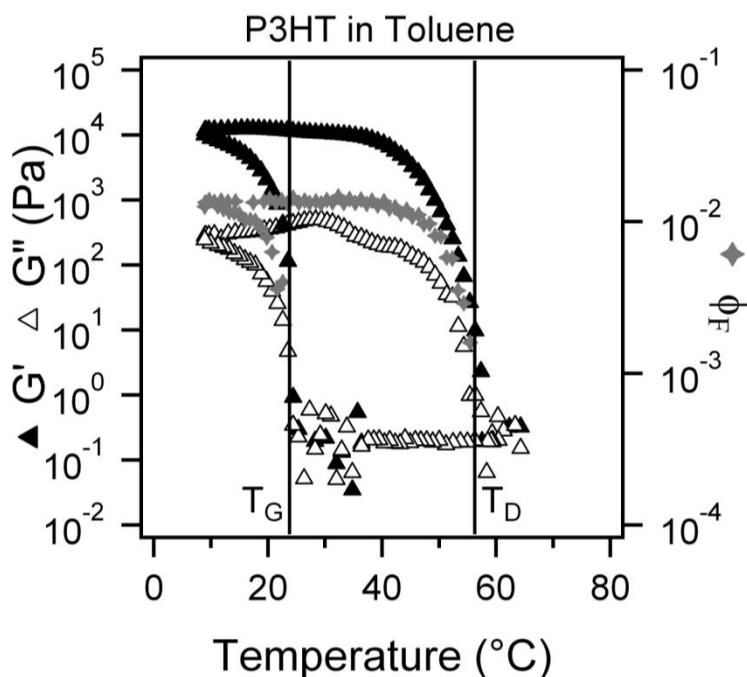


Figure 7.8: P3HT-toluene gel rheology and fiber volume fraction plotted as a function of temperature during gelation and dissolution.

As with the mechanical properties, there are large differences in the electrical properties between these gels. Interestingly, the variations in the electrical and mechanical properties in the various gels are not systematic. Where the P3HT-benzene gel was mechanically the strongest it was also least conductive with a maximum conductivity that was two orders of magnitude less than the conductivity of the P3HT-p-xylene gel. The toluene gel is approximately four times less conductive than the xylene gel. These results may seem contradictory; however, they can be partially explained based on the fiber structure. The mechanical strength of the gel depends upon, not only the number of fibers, but also the strength of the individual fibers and the nature of the interaction between the fibers. The benzene gels contain fibers that are ~10% thicker than the fibers in the toluene or xylene gels. This alone may explain the higher rigidity of the benzene gel despite the lower polymer-fiber conversion. Furthermore, the larger cross-sectional area in P3HT-benzene fibers coupled with the lower polymer-fiber conversion relative to xylene suggests that these gels have the fewest number of fibers when compared to the gels formed in xylene or toluene. While this explains a moderate reduction in the gel conductivity, it does not account for the two orders of magnitude drop that is observed relative to the xylene gels. It is possible that these differences are also related to changes in network branching that would only be resolvable at lower- q than is measured SANS alone.

In Figure 7.9 we explore the relationship between the volume fraction of fibers and the mechanical properties during the early stages of dissolution. As the toluene gel is reheated, both the elastic and viscous modulus continue to increase for the first few

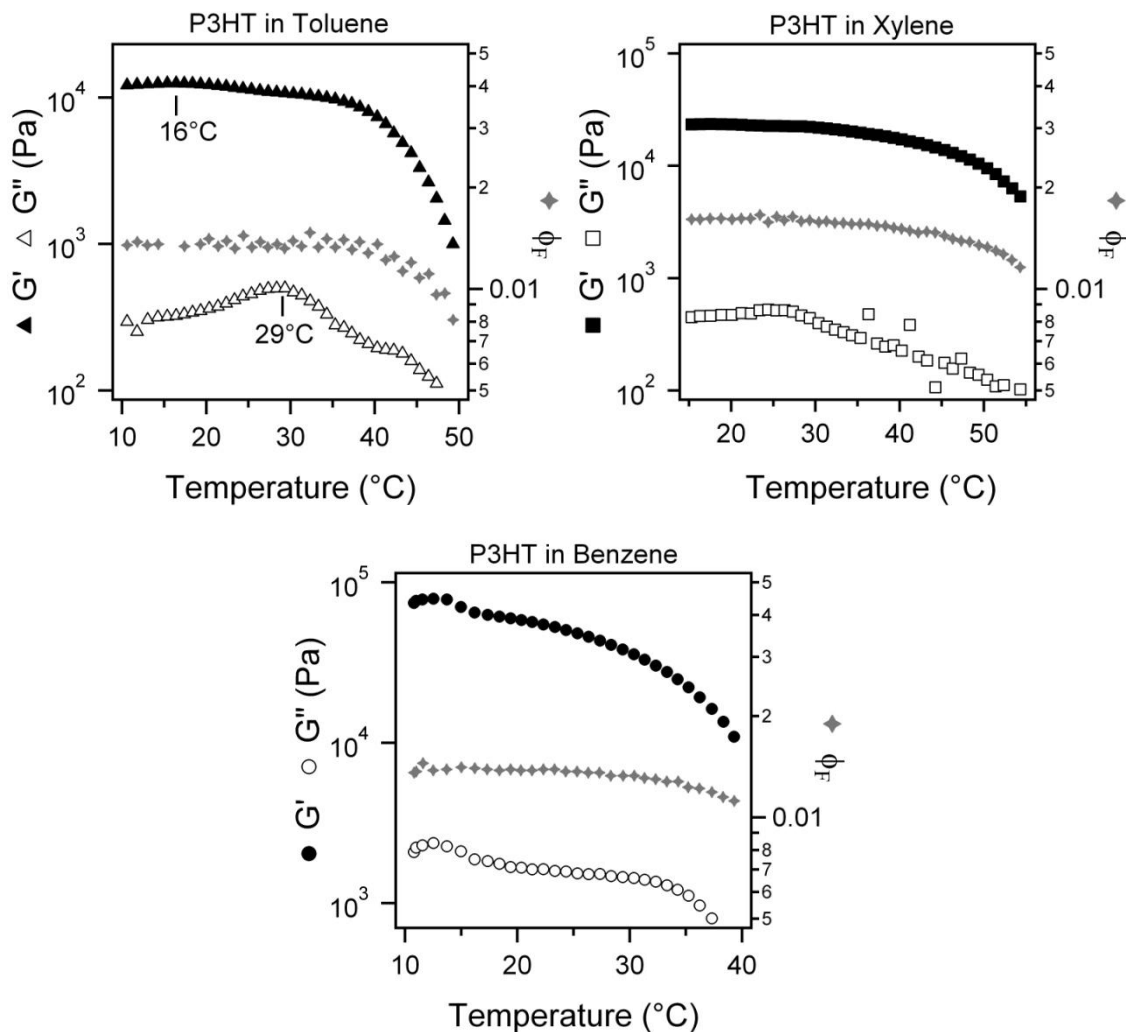


Figure 7.9: Rheology and fiber volume fraction during the early stages of dissolution for P3HT gels in aromatic solvents.

points. At $\sim 16^{\circ}\text{C}$ the elastic modulus begins to decrease slowly while the viscous modulus increases more rapidly until it reaches a maximum at $\sim 29^{\circ}\text{C}$ and begins to decrease. A similar but less pronounced behavior is observed in the xylene gels; however, in the benzene gels, the elastic and viscous moduli mirror each other over the entire heating ramp. In all three cases this behavior is also observed in complementary dielectric-rheology measurements.²⁷ Interestingly, the fiber volume fraction does not show any significant variation during the early stages of the heating ramp in any of the

three gels. This suggests that the variation in the mechanical properties during heating at relatively low temperatures may be the result of increased thermal fluctuations of the polymer or solvent within the fibers.

Discussion

In this chapter, we have utilized rheoSANS towards the development of structure-mechanical property relationships in P3HT gels. Additionally, some qualitative data from complementary conductivity-SANS and dielectric-rheology measurements are also reported. These measurements provide unprecedented insight into the thermoreversible self-assembly and dissolution of P3HT gels in various aromatic solvents.

We have found that mechanical and electrical percolation occur nearly simultaneously with the onset of fiber formation, corresponding to fiber volume fractions less than 0.001 in all of the gels. From the onset of fiber formation, both the polymer-fiber conversion and the elastic and viscous moduli increase during the entire cooling ramp. Upon heating there is significant hysteresis in both the mechanical and structural measurements. Full dissolution occurs at temperatures 30-40 °C greater than the onset of fiber formation. As with the onset of gelation, fibrillar dissolution as measured with both scattering and rheology occur simultaneously.

Across all of the gels the fiber width is found to be ~20 nm, which roughly corresponds to the extended length of an average P3HT chain. Based on these results we would expect to be able to control the fiber width by adjusting the average polymer molecular weight. Unlike the width, the fiber height varies significantly during gelation and dissolution. Initially, relatively thin fibers form, and as gelation proceeds the fiber

height increases. Given the widely accepted crystalline structure of these fibers (illustrated in Figure 6.2), it is reasonable to expect that additional polymer chains are being continuously added to the already formed fibers resulting in full third or four layer of polymer in the fiber backbone.

Based on these observations and previously reported structural analyses of dilute P3HT colloidal network formation, we propose an updated gelation mechanism.¹⁹ A schematic of this mechanism from a recent publication is illustrated in Figure 7.10.²⁷ Unlike the mechanism proposed by Xu and colleagues, our results do not indicate that single fiber formation is a requirement for gelation.¹⁵ In fact, in a recent paper by Newbloom et. al. the formation of discrete colloidal networks of P3HT fibers from very dilute P3HT solutions is reported.^{3, 19} At these higher concentrations, we had expected to observe the same type of cluster formation prior to gelation (Figure 7.10 right); however the percolation threshold was reached so quickly that pre-gel cluster formation cannot be verified from these experiments.

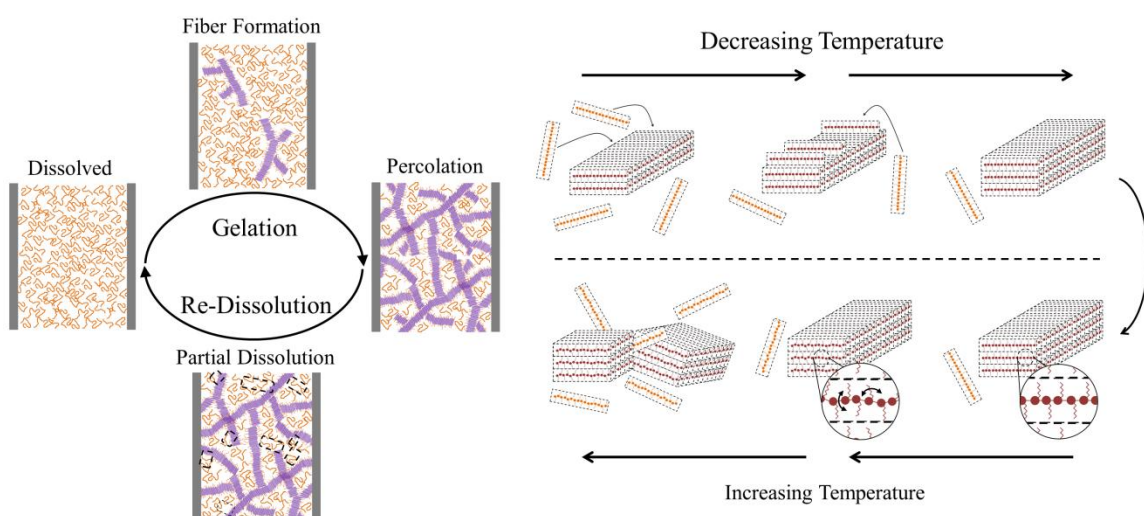


Figure 7.10: The development and re-dissolution of the fibrillar P3HT organogel structure (left). The self-assembly and break-up of individual P3HT fibers that occurs as a function of temperature (right).

Beyond the percolation threshold, new fibers continue to grow and additional layers of polymer are added to the existing fibers. Upon reheating, the fiber morphology initially remains unchanged; however, evolving mechanical properties suggest that the polymers within the fiber begin to undergo thermal fluctuations. This added energy is insufficient to break apart the fiber until well beyond the initial gelation temperature.

Based on these results, we find that it is possible to tune the mechanical and electrical properties of these gels by indirectly altering the fiber and network structure. In this work we have developed relationships between these properties for the gels in three aromatic solvents and found that small fibers with high specific surface area are attributed to higher conductivity, where larger fibers are associated with higher modulus and low conductivity. Ongoing work is necessary to explore other avenues for adjusting the structure of the fibers and the network so that an engineering toolbox can be developed with which the mechanical, structural, and electrical properties can be optimized.

References

1. M. Koppe, C. J. Brabec, S. Heiml, A. Schausberger, W. Duffy, M. Heeney and I. McCulloch, *Macromolecules*, 2009, **42**, 4661-4666.
2. K. M. Coakley and M. D. McGehee, *Chemistry of Materials*, 2004, **16**, 4533-4542.
3. G. M. Newbloom, K. M. Weigandt and D. C. Pozzo, *Macromolecules*, 2012, **45**, 3452-3462.
4. S. Malik, T. Jana and A. K. Nandi, *Macromolecules*, 2001, **34**, 275-282.
5. J. J. Richards, K. M. Weigandt and D. C. Pozzo, *Journal of Colloid and Interface Science*, 2011, **364**, 341-350.
6. B.-G. Kim, E. J. Jeong, H. J. Park, D. Bilby, L. J. Guo and J. Kim, *ACS Applied Materials & Interfaces*, 2011, **3**, 674-680.
7. P.-T. Huang, Y.-S. Chang and C.-W. Chou, *Journal of Applied Polymer Science*, 2011, n/a-n/a.

8. M. A. Green, K. Emery, Y. Hishikawa, W. Warta and E. D. Dunlop, *Prog. Photovoltaics*, 2012, **20**, 12-20.
9. D. H. Kim, Y. P. Jeon, S. H. Lee, D. U. Lee, T. W. Kim and S. H. Han, *Organic Electronics*, 2012, **13**, 1068-1072.
10. Z.-Q. Lin, N.-E. Shi, Y.-B. Li, D. Qiu, L. Zhang, J.-Y. Lin, J.-F. Zhao, C. Wang, L.-H. Xie and W. Huang, *Journal of Physical Chemistry C*, 2011, **115**, 4418-4424.
11. C.-Y. Chen, C.-S. Chang, S.-W. Huang, J.-H. Chen, H.-L. Chen, C.-I. Su and S.-A. Chen, *Macromolecules*, 2010, **43**, 4346-4354.
12. P.-S. Wang, H.-H. Lu, C.-Y. Liu and S.-A. Chen, *Macromolecules*, 2008, **41**, 6500-6504.
13. S. Malik and A. K. Nandi, *The Journal of Physical Chemistry B*, 2003, **108**, 597-604.
14. S. Malik and A. K. Nandi, *Journal of Applied Polymer Science*, 2007, **103**, 2528-2537.
15. W. T. Xu, H. W. Tang, H. Y. Lv, J. Li, X. L. Zhao, H. Li, N. Wang and X. N. Yang, *Soft Matter*, 2012, **8**, 726-733.
16. P. Terech and R. G. Weiss, *Chem. Rev.*, 1997, **97**, 3133-3159.
17. J.-L. Li, B. Yuan, X.-Y. Liu and H.-Y. Xu, *Crystal Growth & Design*, 2010, **10**, 2699-2706.
18. X. Y. Liu and P. D. Sawant, *Advanced Materials*, 2002, **14**, 421-+.
19. G. M. Newbloom, F. S. Kim, S. A. Jenekhe and D. C. Pozzo, *Macromolecules*, 2011, **44**, 3801-3809.
20. W. Yin and M. Dadmun, *Acs Nano*, 2011, **5**, 4756-4768.
21. C. Y. Chen, S. H. Chan, J. Y. Li, K. H. Wu, H. L. Chen, J. H. Chen, W. Y. Huang and S. A. Chen, *Macromolecules*, 2010, **43**, 7305-7311.
22. S. R. Kline, *J. Appl. Crystallogr.*, 2006, **39**, 895-900.
23. S. Kline, *Journal of Applied Crystallography*, 2006, **39**, 895-900.
24. J. Plestil, H. Pospisil, Y. M. Ostanevich and G. Degovics, *Journal of Applied Crystallography*, 1991, **24**, 659-664.
25. M. Kreyenschmidt, F. Uckert and K. Muellen, *Macromolecules*, 1995, **28**, 4577-4582.
26. <http://danse.chem.utk.edu/sansview.html>.
27. G. W. Newbloom, Weigandt, KM, and Pozzo, DC, Submitted.

Chapter 8 Conclusion and Outlook

In this dissertation a combination of mechanical and structural measurements are used to characterize fibrillar gels in order to develop or understand structure-function relationships in these materials. Recall from Chapter 1 that fibrillar gels are materials that exhibit solid-like mechanical properties despite being composed primarily of liquid. The elasticity of these gels is the result of the bicontinuous network of self-assembled fibers that act like a scaffold for the surrounding fluid phase. In Chapters 3-7, fibrillar gels prepared from fibrin and aqueous buffer or poly(3-hexylthiophene) (P3HT) and various aromatic solvents are described. The volume fraction of polymer or protein in these gels is very small ranging from 1 mg/mL to 50 mg/mL. Despite these very low concentrations, the prepared gels from both systems are highly elastic with linear elastic moduli as high as 50 kPa.

The non-linear mechanical properties of the systems studied are extremely distinct. Fibrin gels exhibit a non-linear strain hardening behavior that, though typical for biopolymer gels, is an unusual property that is not observed in most materials. At even small deformations of just 1-5 % strain, the elastic modulus begins to increase. The non-

linear mechanical properties of fibrin are related to the multiscale structure of these gels at the molecular, fibrillar, and network levels. In Chapters 3-5, various aspects of the mechanical and structural properties of fibrin gels were explored. P3HT gels, on the other hand, have very low yield stresses and only very small deformations of $\sim 0.5\%$ strain are required to damage the network structure of these gels. The differences in the non-linear behavior in these gels arise, at least partially, as a result of the nature of the intermolecular attractions that drive self-assembly and stabilize the fibers. P3HT gels are thermoreversible physical gels with weak intermolecular interactions that can be easily disrupted. The mechanical and structural properties of P3HT gels were discussed in Chapters 6 and 7.

In Chapter 3 we demonstrated that SANS and USANS are excellent non-invasive techniques to characterize the structural properties of fibrin clots in aqueous solution at length scales between 1 nm and 15 μm . The analysis of the scattering invariant was an effective method for determining the average internal volume fraction of protein in the fibers. The volume fraction increased systematically with initial monomer concentration. The average radius of the fibers was also determined directly with a Guinier analysis. Finally, the fractal dimension and correlation length were calculated by applying a fractal model to the USANS data. The average radius of fibers is found to decrease slightly with increasing concentration until the fractal correlation length approaches the diameter of the fibers. When the gel starts to get crowded, the fibers begin to grow radially. This change in structural behavior with increased concentration warrants further study as physiological blood clots are expected to have higher concentrations of fibrinogen than in

uncoagulated blood and also contain platelets and blood cells which may cause crowding at even lower concentrations.

In Chapter 4, an experimental framework was developed to characterize a fully hydrated biopolymer gel using small angle neutron scattering under simultaneous strain. Both the fiber dimensions and the extent of fiber alignment were measurable regardless of the opacity of the sample and without any required sample processing steps. The use of neutron scattering has enabled characterization of structural transitions in a single gel with very fine resolution as a function of strain. In this chapter, SANS was utilized as a tool to systematically monitor the structure of fibrin gels as a function of increasing strain. This technique has proven to be especially useful for determining the structural changes that occur in higher concentration and coarse fiber gels as the opacity of these gels prevent the use of most optical techniques. The implementation of two-dimensional form factor fits was critical to the rigorous strain dependent characterization of structural parameters in aligned fibers.

The unique non-linear rheological response of coarse fibrin gels suggests that more than one mechanism is responsible for the strain-hardening response in fibrin. We have shown that both of the primary theories for strain-hardening are necessary to describe the rich rheological behavior of these gels over all levels of deformation. At low strains, a reduction in the conformational entropy of the fibers resulted in a 50% increase in the shear modulus. This was followed by a region of significant structural changes ($\gamma > 30\%$) where fibers align, stretch and contract radially as shown in Figure 4.7. These structural transitions were perfectly correlated with a simultaneous increase in shear modulus of more than 80%. These observations were also consistent with a transition

from a bending-dominated response to a stretching-dominated response. Separating these two regions, we found a strain-softening behavior that is still poorly understood and not fully characterized. Further research is necessary to understand the unique strain weakening that occurs at intermediate strains ($10\% < \gamma < 30\%$).

In Chapter 5, we examined the effect of direct chemical modification of fibrinogen by oxidation with HOCl on the structural and mechanical properties of fibrin gels. Oxidation with HOCl led to the preferential oxidation of specific methionine residues on the α , β and γ chains of fibrinogen. We found that methionine oxidation inhibits the lateral aggregation of protofibrils. This led to the formation of gels with small fibers and reduced porosity as a result of the high fiber density when compared to non-oxidized fibrin. The oxidized gels were also found to have a weaker linear viscoelastic moduli and a higher linear viscoelastic limit as a result of the morphological alterations. The high fiber density and low porosity that arises from the inhibition of protofibril aggregation led to prolonged clot lysis times, which were attributed to reduced diffusivity of plasminogen through the gel. This work has important medical implications as several conditions that are associated with thrombosis have been shown to induce clots with similar morphological characteristics to those associated with HOCl oxidation in Chapter 5. These results suggest that there is a potential oxidation-specific mechanism associated with these diseases that leads to abnormal coagulation.

A natural next step for the fibrin project is to use these combined SANS and rheology methods to develop a better understanding of fibrinolysis. In Chapter 5 the use of oxidized fibrinogen in fibrin gels was shown to prolong clot lysis times. By simultaneously characterizing the mechanical and structural measurements of clots

during gelation and lysis valuable insight may be gained. For instance, once the plasmin reaches a fiber, does it cleave the proteins along the outside of the fibers or slice the proteins through the fiber diameter? In a simple rheoSANS experiment the fiber diameter and volume fraction can be measured as a function of time during fibrinolysis. In this experiment, if the plasmin preferentially slices through the diameter of the fibers we would expect that short non-networked fibers may still exist even after mechanical percolation is disrupted.

In Chapter 6, we transition from fibrin gels to P3HT gels. Here P3HT gels of variable concentration were prepared in benzene, toluene, and p-xylene. The mechanical and structural properties of these gels were characterized with a combination of rheology and small angle neutron scattering. In this system, gelation was induced by cooling the P3HT-solvent solution to reduce the polymer solubility. Self-assembly of P3HT results in the formation of a three-dimensional network of semi-crystalline fibers, which is expected to facilitate charge transport in organic photovoltaic devices. We found that substantial molecular weight partitioning occurs during fiber formation with higher molecular weight polymer forming fibers and lower molecular weight polymer remaining soluble. The overall conversion of polymer into fibers is solvent dependent. Here we found that gels formed in xylene have ~10% greater polymer conversion than gels in benzene or toluene. Interestingly, although the P3HT-xylene gels had the highest overall conversion of polymer into fibers, the elastic moduli of these gels were found to be significantly lower than the P3HT-benzene gels. In contrast, the P3HT-toluene gels were weaker than the P3HT-xylene gels as expected. From the structural analysis, we found that the fibers had similar morphology in all three solvents with the exception of the fiber

thickness. Fibers formed in benzene were thicker than fibers formed in xylene and toluene. Increased rigidity of the thicker fibers may explain the higher elastic modulus measured in the benzene-P3HT gels.

In Chapter 7, simultaneous rheology and SANS, rheoSANS, measurements were used to probe the evolution of P3HT in aromatic solvents during gelation and dissolution. We had hypothesized that we would observe fiber growth and the formation of discrete fibrillar networks in dispersion prior to mechanical percolation. Surprisingly, we instead found that mechanical percolation occurs nearly instantaneously with the onset of P3HT self-assembly. The width of the fibers was relatively constant and roughly corresponded to the extended length of the average polymer chain. The fiber thickness varied significantly throughout the gelation and dissolution processes, with additional polymer stacking to add a third (xylene and toluene) or fourth (benzene) layer of P3HT to the fibers. This effect was most dramatic in the benzene gels where the fiber thickness continued to increase even as the gel was heated until dissolution began. Based on the mechanical and rheological measurements reported in Chapter 7, we have proposed a new mechanism for the formation and dissolution of fibers in P3HT gels.

For the P3HT system, ongoing work is necessary to explore other avenues for adjusting the structure of the fibers and the network so that an engineering toolbox can be developed with which the mechanical, structural, and electrical properties can be optimized. The benzene-P3HT gels were expected to have a lower conductivity as a result of having fewer fibers than the other gels. However, the orders of magnitude drop in conductivity in the benzene-P3HT gels relative to the toluene or xylene-P3HT gels

remains poorly understood. Determining the origin of these differences may be the key to designing gels with optimized properties.

In this dissertation, we have developed a rigorous strategy for determining structure-property relationships in fibrillar gels. Using small angle scattering to characterize the unmodified gels formed *in situ* eliminates artifacts that commonly occur when these low solid fraction materials are prepared for other traditional structural characterization techniques. Furthermore, by combining neutron scattering with mechanical measurements or deformation we are able to directly associate mechanical and structural properties in evolving materials. These strategies have proven to be invaluable in the understanding of the two systems described herein and will be critical to ongoing and future work with these and other materials.

Bibliography

- Abramoff, M. D., Magalhaes, P. J. and Ram, S.J., (2004). "Image Processing with ImageJ." Biophotonics International **11**(7): 36-42.
- Anand, S. and S. L. Diamond (1996). "Computer simulation of systemic circulation and clot lysis dynamics during thrombolytic therapy that accounts for inner clot transport and reaction." Circulation **94**(4): 763-774.
- Avrutin, V., N. Izyumskaya, et al. (2010). "Semiconductor solar cells: Recent progress in terrestrial applications." Superlattices and Microstructures **49**(4): 337-364.
- Baek, W. H., H. Yang, et al. (2009). "Effect of P3HT:PCBM concentration in solvent on performances of organic solar cells." Solar Energy Materials and Solar Cells **93**(8): 1263-1267.
- Barker, J. G., C. J. Glinka, et al. (2005). "Design and performance of a thermal-neutron double-crystal diffractometer for USANS at NIST." Journal of Applied Crystallography **38**(6): 1004-1011.
- Basu, S., C. P. Marini, et al. (1995). "Comparative-Study of Biological Glues - Cryoprecipitate Glue, 2-Component Fibrin Sealant, and French Glue." Annals of Thoracic Surgery **60**(5): 1255-1262.
- Berman, H., K. Henrick, et al. (2003). "Announcing the worldwide Protein Data Bank." Nature Structural Biology **10**(12): 980-980.
- Boudouris, B. W., F. Molins, et al. (2009). "Synthesis, Optical Properties, and Microstructure of a Fullerene-Terminated Poly(3-hexylthiophene)." Macromolecules **42**(12): 4118-4126.
- Bricaud, Q., A. Cravino, et al. (2009). "Poly(thiophenes) derivatized with oligo(oxyethylene) chains as donor materials for organic solar cells." Solar Energy Materials and Solar Cells **93**(9): 1624-1629.
- Broedersz, C. P., K. E. Kasza, et al. (2010). "Measurement of nonlinear rheology of cross-linked biopolymer gels." Soft Matter **6**(17): 4120-4127.
- Brown, A. E. X., R. I. Litvinov, et al. (2009). "Multiscale Mechanics of Fibrin Polymer: Gel Stretching with Protein Unfolding and Loss of Water." Science **325**(5941): 741-744.

- Brown, A. E. X., R. I. Litvinov, et al. (2007). Forced unfolding of the coiled-coils of fibrinogen by single molecule AFM, Biophysical Society.
- Burger, C., B. S. Hsiao, et al. (2010). "Preferred Orientation in Polymer Fiber Scattering." Polymer Reviews **50**(1): 91-111.
- Carr, M. E., R. M. Dent, et al. (1996). "Abnormal fibrin structure and inhibition of fibrinolysis in patients with multiple myeloma." Journal of Laboratory and Clinical Medicine **128**(1): 83-88.
- Carr, M. E. and J. Hermans (1978). "Size and Density of Fibrin Fibers from Turbidity." Macromolecules **11**(1): 46-50.
- Chang, Y. H., S. R. Tseng, et al. (2009). "Polymer solar cell by blade coating." Organic Electronics **10**(5): 741-746.
- Chaudhuri, O., S. H. Parekh, et al. (2007). "Reversible stress softening of actin networks." Nature **445**(7125): 295-298.
- Chen, C.-Y., C.-S. Chang, et al. (2010). "Phase-Separation-Induced Gelation of Poly(9,9-dioctylfluorene) Methylcyclohexane Solution." Macromolecules **43**(9): 4346-4354.
- Chen, C. Y., S. H. Chan, et al. (2010). "Formation and Thermally-Induced Disruption of Nanowhiskers in Poly(3-hexylthiophene)/Xylene Gel Studied by Small-Angle X-ray Scattering." Macromolecules **43**(17): 7305-7311.
- Chen, T. A., X. M. Wu, et al. (1995). "Regiocontrolled Synthesis of Poly(3-Alkylthiophenes) Mediated by Rieke Zinc – Their Characterization and Solid-State Properties." Journal of the American Chemical Society **117**(1): 233-244.
- Coakley, K. M. and M. D. McGehee (2004). "Conjugated polymer photovoltaic cells." Chemistry of Materials **16**: 4533-4542.
- Collet, J.-P., J. L. Moen, et al. (2005). "The $\hat{I}\pm C$ domains of fibrinogen affect the structure of the fibrin clot, its physical properties, and its susceptibility to fibrinolysis." Blood **106**(12): 3824-3830.
- Collet, J. P., Z. Mishal, et al. (1999). "Abnormal fibrin clot architecture in nephrotic patients is related to hypofibrinolysis: influence of plasma biochemical modifications - A possible mechanism for the high thrombotic tendency?" Thrombosis and Haemostasis **82**(5): 1482-1489.
- Collet, J. P., D. Park, et al. (2000). "Influence of fibrin network conformation and fibrin fiber diameter on fibrinolysis speed - Dynamic and structural approaches by confocal microscopy." Arteriosclerosis Thrombosis and Vascular Biology **20**(5): 1354-1361.

- Collet, J. P., H. Shuman, et al. (2005). "The elasticity of an individual fibrin fiber in a clot." Proceedings of the National Academy of Sciences of the United States of America **102**(26): 9133-9137.
- Dobrynin, A. V. and J. M. Y. Carrillo (2011). "Universality in Nonlinear Elasticity of Biological and Polymeric Networks and Gels." Macromolecules **44**(1): 140-146.
- Doolittle, R. F. (1984). "Fibrinogen and Fibrin." Annual Review of Biochemistry **53**: 195-229.
- Erk, K. A., K. J. Henderson, et al. (2010). "Strain Stiffening in Synthetic and Biopolymer Networks." Biomacromolecules **11**(5): 1358-1363.
- Fatah, K., A. Silveira, et al. (1996). "Proneness to formation of tight and rigid fibrin gel structures in men with myocardial infarction at a young age." Thrombosis and Haemostasis **76**(4): 535-540.
- Flory, P. J. (1974). "Introductory lecture." Faraday Discussions of the Chemical Society **57**: 7-18.
- Fu, X., J. Chen, et al. (2011). "Shear stress-induced unfolding of VWF accelerates oxidation of key methionine residues in the A1A2A3 region." Blood **118**(19): 5283-5291.
- Glaser, C. B., J. Morser, et al. (1992). "Oxidation of a Specific Methionine in Thrombomodulin by Activated Neutrophil Products Blocks Cofactor Activity – A Potential Mechanism for Modulation of Coagulation." Journal of Clinical Investigation **90**(6): 2565-2573.
- Glinka, C. J., J. G. Barker, et al. (1998). "The 30 m Small-Angle Neutron Scattering Instruments at the National Institute of Standards and Technology." Journal of Applied Crystallography **31**(3): 430-445.
- Gorkun, O. V., Y. I. Veklich, et al. (1994). "ROLE OF THE ALPHA-C DOMAINS OF FIBRIN IN CLOT FORMATION." Biochemistry **33**(22): 6986-6997.
- Green, M. A., K. Emery, et al. (2012). "Solar cell efficiency tables (version 39)." Progress in Photovoltaics **20**(1): 12-20.
- Guenet, J. M. (2006). "Microfibrillar networks: Polymer thermoreversible gels vs organogels." Macromolecular Symposia **241**: 45-50.
- Guinier, A. and G. Fournet (1955). Small-angle scattering of X-rays, Wiley.
- Guthold, M., W. Liu, et al. (2007). "A comparison of the mechanical and structural properties of fibrin fibers with other protein fibers." Cell Biochemistry and Biophysics **49**: 165-181.

- Guthold, M., W. Liu, et al. (2004). "Visualization and mechanical manipulations of individual fibrin fibers suggest that fiber cross section has fractal dimension 1.3." Biophysical Journal **87**: 4226-4236.
- Hammouda, B. 2011. Probing Nanoscale Structures - The SANS Toolbox.
- Hartmann, A., P. Boukamp, et al. (2006). "Confocal reflection imaging of 3D fibrin polymers." Blood Cells Molecules and Diseases **36**(2): 191-193.
- Hauch, J. A., P. Schilinsky, et al. (2008). "Flexible organic P3HT : PCBM bulk-heterojunction modules with more than 1 year outdoor lifetime." Solar Energy Materials and Solar Cells **92**(7): 727-731.
- Hazen, S. L., F. F. Hsu, et al. (1996). "Human neutrophils employ chlorine gas as an oxidant during phagocytosis." Journal of Clinical Investigation **98**(6): 1283-1289.
- Hecht, A. M., R. Duplessix, et al. (1985). "Structural Inhomogeneities in the Range 2.5-2500 Å in Polyacrylamide Gels." Macromolecules **18**(11): 2167-2173.
- Henschen-Edman, A. H. (2001). Fibrinogen non-inherited heterogeneity and its relationship to function in health and disease. Fibrinogen. **936**: 580-593.
- Hermans, J. J., P. H. Hermans, et al. (1946). "Quantitative Evaluation of Orientation in Cellulose Fibres from the X-ray Fibre Diagram." Recueil Des Travaux Chimiques Des Pays-Bas-Journal of the Royal Netherlands Chemical Society **65**(7-8): 427-447.
- Houser, J. R., N. E. Hudson, et al. (2010). "Evidence that alpha C Region Is Origin of Low Modulus, High Extensibility, and Strain Stiffening in Fibrin Fibers." Biophysical Journal **99**(9): 3038-3047.
- <http://danse.chem.utk.edu/sansview.html>.
- Huang, P.-T., Y.-S. Chang, et al. (2011). "Preparation of porous poly(3-hexylthiophene) by freeze-dry method and its application to organic photovoltaics." Journal of Applied Polymer Science: n/a-n/a.
- Huang, W. Y., P. T. Huang, et al. (2008). "Aggregation and Gelation Effects on the Performance of Poly(3-hexylthiophene)/Fullerene Solar Cells." Macromolecules **41**(20): 7485-7489.
- Hudson, N. E., J. R. Houser, et al. (2010). "Stiffening of Individual Fibrin Fibers Equitably Distributes Strain and Strengthens Networks." Biophysical Journal **98**(8): 1632-1640.
- Ihn, K. J., J. Moulton, et al. (1993). "Whiskers of Poly(3-Alkylthiophene)s." Journal of Polymer Science Part B-Polymer Physics **31**(6): 735-742.

- Ikkai, F. and E. Adachi (2004). "Novel method of producing polymer gels in aqueous solution using UV irradiation." Macromolecular Rapid Communications **25**(16): 1514-1517.
- Immaneni, A. and A. J. McHugh (1998). "Flow-induced conformational changes and phase behavior of aqueous poly-L-lysine solutions." Biopolymers **45**(3): 239-246.
- Ishi-i, T. and S. Shinkai (2005). "Dye-based organogels: Stimuli-responsive soft materials based on one-dimensional self-assembling aromatic dyes." Supramolecular Dye Chemistry **258**: 119-160.
- Jaczewska, J., A. Budkowski, et al. (2008). "Polymer vs solvent diagram of film structures formed in spin-cast poly(3-alkylthiophene) blends." Macromolecules **41**(13): 4802-4810.
- Janmey, P. A., J. Winer et al. (1991). " Fibrin gels and their clinical and bioengineering applications. " Journal of the Royal Society Interface **6**(1): 1-10.
- Janmey, P. A., U. Euteneuer, et al. (1991). "Viscoelastic Properties of Vimentin Compared with Other Filamentous Biopolymer Networks." Journal of Cell Biology **113**(1): 155-160.
- Jorneskog, G., K. Fatah, et al. (1998). "Fibrin gel structure in diabetic patients before and during treatment with acetylsalicylic acid: a pilot study." Fibrinolysis & Proteolysis **12**(6): 360-365.
- Kalyanaraman, B. and P. G. Sohnle (1985). "Generation of Free-Radical Intermediates from Foreign Compounds by Neutrophil-Derived Oxidants." Journal of Clinical Investigation **75**(5): 1618-1622.
- Kambayashi, T., H. Wada, et al. (2006). "Enhancement of conductivity in poly (3-hexylthiophene) films prepared by spin-coating from blended solutions with small molecules." Organic Electronics **7**(5): 440-444.
- Kang, H., Q. Wen, et al. (2009). "Nonlinear Elasticity of Stiff Filament Networks: Strain Stiffening, Negative Normal Stress, and Filament Alignment in Fibrin Gels." Journal of Physical Chemistry B **113**(12): 3799-3805.
- Keller, A. (1995). "Introductory lecture - Aspects of polymer gels." Faraday Discussions **101**: 1-49.
- Kim, B.-G., E. J. Jeong, et al. (2011). "Effect of Polymer Aggregation on the Open Circuit Voltage in Organic Photovoltaic Cells: Aggregation-Induced Conjugated Polymer Gel and its Application for Preventing Open Circuit Voltage Drop." ACS Applied Materials & Interfaces **3**(3): 674-680.

- Kim, D. H., Y. P. Jeon, et al. (2012). "Enhancement of the power conversion efficiency for organic photovoltaic devices due to an embedded rugged nanostructural layer." Organic Electronics **13**(6): 1068-1072.
- Kline, S. (2006). "Reduction and analysis of SANS and USANS data using IGOR Pro." Journal of Applied Crystallography **39**(6): 895-900.
- Kline, S. R. (2006). "Reduction and analysis of SANS and USANS data using IGOR Pro." Journal of Applied Crystallography **39**: 895-900.
- Kollman, J. M., L. Pandi, et al. (2009). "Crystal Structure of Human Fibrinogen." Biochemistry **48**(18): 3877-3886.
- Koppe, M., C. J. Brabec, et al. (2009). "Influence of Molecular Weight Distribution on the Gelation of P3HT and Its Impact on the Photovoltaic Performance." Macromolecules **42**(13): 4661-4666.
- Kreyenschmidt, M., F. Uckert, et al. (1995). "A New Soluble Poly(p-phenylene) with Tetrahydropyrene Repeating Units." Macromolecules **28**(13): 4577-4582.
- Larsson, U. (1988). "Polymerization and gelation of fibrinogen in D₂O." European Journal of Biochemistry **174**(1): 139-144.
- Li, J.-L., B. Yuan, et al. (2010). "Microengineering of Supramolecular Soft Materials by Design of the Crystalline Fiber Networks." Crystal Growth & Design **10**(6): 2699-2706.
- Liberatore, M. W., F. Nettesheim, et al. (2006). "Spatially resolved small-angle neutron scattering in the 1-2 plane: A study of shear-induced phase-separating wormlike micelles." Physical Review E **73**(2).
- Lin, D. C., J. F. Douglas, et al. (2010). "Development of minimal models of the elastic properties of flexible and stiff polymer networks with permanent and thermoreversible cross-links." Soft Matter **6**(15): 3548-3561.
- Lin, Y. C., N. Y. Yao, et al. (2010). "Origins of Elasticity in Intermediate Filament Networks." Physical Review Letters **104**(5): 4.
- Lin, Z.-Q., N.-E. Shi, et al. (2011). "Preparation and Characterization of Polyfluorene-Based Supramolecular pi-Conjugated Polymer Gels." Journal of Physical Chemistry C **115**(11): 4418-4424.
- Lindner, P. (2004). Neutrons, X-rays, and light: scattering methods applied to soft condensed matter, Elsevier.
- Linnes, M. P., B. D. Ratner, et al. (2007). "A fibrinogen-based precision microporous scaffold for tissue engineering." Biomaterials **28**(35): 5298-5306.

- Liu, W., R. Hantgan, et al. (2004). "Mechanical properties of individual fibrin fibers." Bioophysical Journal **86**(1): 477A-477A.
- Liu, X. Y. and P. D. Sawant (2002). "Mechanism of the formation of self-organized microstructures in soft functional materials." Advanced Materials **14**(6): 421-+.
- Mackintosh, F. C., J. Kas, et al. (1995). "Elasticity of semiflexible biopolymer networks." Physical Review Letters **75**(24): 4425-4428.
- Malik, S., T. Jana, et al. (2001). "Thermoreversible gelation of regioregular poly(3-hexylthiophene) in xylene." Macromolecules **34**(2): 275-282.
- Malik, S. and A. K. Nandi (2002). "Crystallization mechanism of regioregular poly(3-alkyl thiophene)s." Journal of Polymer Science Part B: Polymer Physics **40**(18): 2073-2085.
- Malik, S. and A. K. Nandi (2003). "Thermodynamic and Structural Investigation of Thermoreversible Poly(3-dodecyl thiophene) Gels in the Three Isomers of Xylene." The Journal of Physical Chemistry B **108**(2): 597-604.
- Malik, S. and A. K. Nandi (2007). "Influence of alkyl chain length on the gelation mechanism of thermoreversible gels of regioregular poly(3-alkyl thiophenes) in xylene." Journal of Applied Polymer Science **103**(4): 2528-2537.
- Marshall, J. M., A. J. Brown, et al. (1994). "Conformational Studies of Human Plasminogen and Plasminogen Fragments: Evidence for a Novel Third Conformation of Plasminogen." Biochemistry **33**(12): 3599-3606.
- Miserez, A., S. ScottWasko, et al. (2009). "Non-entropic and reversible long-range deformation of an encapsulating bioelastomer." Nature Materials **8**(11): 910-916.
- Mittelbach, P. a. P., G. (1961). Acta Phys. Austriaca **14**: 185-211.
- Morales, M. E., V. Gallardo, et al. (2009). "Study and description of hydrogels and organogels as vehicles for cosmetic active ingredients." Journal of Cosmetic Science **60**(6): 627-636.
- Nagai, A., J. Miyake, et al. (2008). "Highly Luminescent BODIPY-Based Organoboron Polymer Exhibiting Supramolecular Self-Assemble Structure." Journal of the American Chemical Society **130**(46): 15276-+.
- Nalian, A. and A. V. Iakhiaev (2008). "Possible mechanisms contributing to oxidative inactivation of activated protein C: Molecular dynamics study." Thrombosis and Haemostasis **100**(1): 18-25.
- Neutron News, Vol. 3, No. 3, 1992, pp. 29-37 (Neutron cross section data.)

- Newbloom, G. M., F. S. Kim, et al. (2011). "Mesoscale Morphology and Charge Transport in Colloidal Networks of Poly(3-hexylthiophene)." Macromolecules **44**(10): 3801-3809.
- Newbloom, G. M., K. M. Weigandt, et al. (2012). "Electrical, Mechanical, and Structural Characterization of Self-Assembly in Poly(3-hexylthiophene) Organogel Networks." Macromolecules **45**(8): 3452-3462.
- Newbloom, G. M., K. M. Weigandt, et al. (2012). "Structure and property development of poly(3-hexylthiophene) organogels probed with combined rheology, conductivity and small angle neutron scattering" Soft Matter **8**: 8854-8864
- Nielsen, V. G., B. M. Cohen, et al. (2005). "Effects of coagulation factor deficiency on plasma coagulation kinetics determined via thrombelastography (R): critical roles of fibrinogen and factors II, VII, X and XII." Acta Anaesthesiologica Scandinavica **49**(2): 222-231.
- Nieuwenhuizen, W. (2001). Fibrin-mediated plasminogen activation. Fibrinogen. **936**: 237-246.
- Onck, P. R., T. Koeman, et al. (2005). "Alternative explanation of stiffening in cross-linked semiflexible networks." Physical Review Letters **95**(17).
- Oosterbaan, W. D., V. Vriendts, et al. (2009). "Efficient formation, isolation and characterization of poly(3-alkylthiophene) nanofibres: probing order as a function of side-chain length." Journal of Materials Chemistry **19**(30): 5424-5435.
- Pattison, D. I., C. L. Hawkins, et al. (2007). "Hypochlorous acid-mediated protein oxidation: How important are chloramine transfer reactions and protein tertiary Structure?" Biochemistry **46**(34): 9853-9864.
- Pelton, R. (2000). "Temperature-sensitive aqueous microgels." Advances in Colloid and Interface Science **85**(1): 1-33.
- Piechocka, I. K., R. G. Bacabac, et al. (2010). "Structural Hierarchy Governs Fibrin Gel Mechanics." Biophysical Journal **98**(10): 2281-2289.
- Ping, L., L. Huang, et al. (2011). "Substitution of the Human alpha C Region with the Analogous Chicken Domain Generates a Fibrinogen with Severely Impaired Lateral Aggregation: Fibrin Monomers Assemble into Protofibrils but Protofibrils Do Not Assemble into Fibers." Biochemistry **50**(42): 9066-9075.
- Pisano, J. J., Finlayso,Js, et al. (1968). "Cross-Link in Fibrin Polymerized by Factor 13 Epsilon-(Gamma-Glutamyl)Lysine." Science **160**(3830): 892-&.
- Plestil, J., H. Pospisil, et al. (1991). "Molecular-Weight Determination from Small-Angle Scattering Without Absolute Intensities –Advantages and Limitations." Journal of Applied Crystallography **24**: 659-664.

- Porcar, L., D. Pozzo, et al. (2011). "Rheo-small-angle neutron scattering at the National Institute of Standards and Technology Center for Neutron Research." Review of Scientific Instruments **82**(8): 7.
- Pretorius, E., H. Steyn, et al. (2011). "Differences in fibrin fiber diameters in healthy individuals and thromboembolic ischemic stroke patients." Blood Coagulation & Fibrinolysis **22**(8): 696-700.
- Qin, Z., L. Kreplak, et al. (2009). "Hierarchical Structure Controls Nanomechanical Properties of Vimentin Intermediate Filaments." Plos One **4**(10): 14.
- Renkin, E. M. (1954). "Filtration, Diffusion, and Molecular Sieving Through Porous Cellulose Membranes." Journal of General Physiology **38**(2): 225-243.
- Richards, J. J., K. M. Weigandt, et al. (2011). "Aqueous dispersions of colloidal poly(3-hexylthiophene) gel particles with high internal porosity." Journal of Colloid and Interface Science **364**(2): 341-350.
- Ross-Murphy, S. B. (1998). "Reversible and irreversible biopolymer gels - Structure and mechanical properties." Berichte Der Bunsen-Gesellschaft-Physical Chemistry Chemical Physics **102**(11): 1534-1539.
- Ryan, E. A., L. F. Mockros, et al. (1999). "Structural origins of fibrin clot rheology." Biophysical Journal **77**(5): 2813-2826.
- Sauls, D. L., E. Lockhart, et al. (2006). "Modification of fibrinogen by homocysteine thiolactone increases resistance to fibrinolysis: A potential mechanism of the thrombotic tendency in hyperhomocysteinemia." Biochemistry **45**(8): 2480-2487.
- Shacter, E., J. A. Williams, et al. (1995). "Oxidative Modification of Fibrinogen Inhibits Thrombin-Catalyzed Clot Formation." Free Radical Biology and Medicine **18**(4): 815-821.
- Shacter, E., J. A. Williams, et al. (1994). "Differential Susceptibility of Plasma-Proteins to Oxidative Modification – Examination by Western-Blot Immunoassay." Free Radical Biology and Medicine **17**(5): 429-437.
- Shah, J. V. and P. A. Janmey (1997). "Strain hardening of fibrin gels and plasma clots." Rheologica Acta **36**(3): 262-268.
- Shao, B., A. Belaaouaj, et al. (2005). "Methionine Sulfoxide and Proteolytic Cleavage Contribute to the Inactivation of Cathepsin G by Hypochlorous Acid." Journal of Biological Chemistry **280**(32): 29311-29321.
- Shulman, S. (1953). "The Size and Shape of Bovine Fibrinogen – Studies of Sedimentation, Diffusion and Viscosity." Journal of the American Chemical Society **75**(23): 5846-5852.

- Sirringhaus, H., P. J. Brown, et al. (2000). Microstructure-mobility correlation in self-organised, conjugated polymer field-effect transistors.
- Spalla, O. (2002). Neutrons, X-rays, and Light: Scattering Applied to Soft Condensed Matter. Amsterdam, Elsevier.
- Spanhel, L. and M. A. Anderson (1991). "Semiconductor Clusters in the Sol-Gel Process – Quantized Aggregation, Gelation, and Crystal-Growth in Concentration ZNO Colloids." Journal of the American Chemical Society **113**(8): 2826-2833.
- Stief, T. W. (2007). "Singlet oxygen potentiates thrombolysis." Clinical and Applied Thrombosis-Hemostasis **13**(3): 259-278.
- Stief, T. W., J. Kurz, et al. (2000). "Singlet oxygen inactivates fibrinogen, factor V, factor VIII, factor X, and platelet aggregation of human blood." Thrombosis Research **97**(6): 473-480.
- Storm, C., J. J. Pastore, et al. (2005). "Nonlinear elasticity in biological gels." Nature **435**(7039): 191-194.
- Sun, S. Y., T. Salim, et al. (2011). "A new insight into controlling poly(3-hexylthiophene) nanofiber growth through a mixed-solvent approach for organic photovoltaics applications." Journal of Materials Chemistry **21**(2): 377-386.
- Teixeira, J. (1988). "Small-angle scattering by fractal systems." Journal of Applied Crystallography **21**(6): 781-785.
- Terech, P. and R. G. Weiss (1997). "Low molecular mass gelators of organic liquids and the properties of their gels." Chemical Reviews **97**(8): 3133-3159.
- Totosaus, A., J. G. Montejano, et al. (2002). "A review of physical and chemical protein-gel induction." International Journal of Food Science & Technology **37**(6): 589-601.
- Tsurupa, G., R. R. Hantgan, et al. (2009). "Structure, Stability, and Interaction of the Fibrin(ogen) alpha C-Domains." Biochemistry **48**(51): 12191-12201.
- Tsurupa, G., A. Mahid, et al. (2011). "Structure, Stability, and Interaction of Fibrin alpha C-Domain Polymers." Biochemistry **50**(37): 8028-8037.
- van Dillen, T., P. R. Onck, et al. (2008). "Models for stiffening in cross-linked biopolymer networks: A comparative study." Journal of the Mechanics and Physics of Solids **56**(6): 2240-2264.
- Verilhac, J. M., G. LeBlevenec, et al. (2006). "Effect of macromolecular parameters and processing conditions on supramolecular organisation, morphology and electrical transport properties in thin layers of regioregular poly(3-hexylthiophene)." Synthetic Metals **156**(11-13): 815-823.

- Voter, W. A., C. Lucaveche, et al. (1986). "Concentration of Protein in Fibrin Fibers and Fibrinogen Polymers determined by Refractive-Index Matching." Biopolymers **25**(12): 2375-2384.
- Wang, P.-S., H.-H. Lu, et al. (2008). "Gel formation via physical cross-linking in the soluble conjugated polymer, poly [2-methoxy-5-(2-ethylhexyloxy)-1,4-phenylenevinylene], in solution by addition of alkalies." Macromolecules **41**(17): 6500-6504.
- Weigandt, K. M., D. C. Pozzo, et al. (2009). "Structure of high density fibrin networks probed with neutron scattering and rheology." Soft Matter **5**(21): 4321-4330.
- Weigandt, K. M., L. Porcar, et al. (2011). "In situ neutron scattering study of structural transitions in fibrin networks under shear deformation." Soft Matter **7**:9992-10000.
- Weigandt, K. M., N. White et al. (2012). "Alterations in Fibrin Clot Structure and Mechanics Attributed to Specific Oxidation of Methionine Residues in Fibrinogen." Submitted to the Biophysical Journal.
- Weisel, J. W. (1986). "Fibrin Assembly – Lateral Aggregation and the Role of the 2 Pairs of Fibrinopeptides." Biophysical Journal **50**(6): 1079-1093.
- Weisel, J. W. (2004). "The mechanical properties of fibrin for basic scientists and clinicians." Biophysical Chemistry **112**(2-3): 267-276.
- Weisel, J. W. and L. Medved (2001). The structure and function of the alpha C domains of fibrinogen. Fibrinogen. **936**: 312-327.
- Wen, Q., A. Basu, et al. (2007). "Local and global deformations in a strain-stiffening fibrin gel." New Journal of Physics **9**.
- Wicks, C. E., Welty, W. R., Wilson, R.E., and Rorrer, G.L. (2008). Fundamentals Of Momentum, Heat, And Mass Transfer, John Wiley & Sons, Inc.
- Xu, W. T., H. W. Tang, et al. (2012). "Sol-gel transition of poly(3-hexylthiophene) revealed by capillary measurements: phase behaviors, gelation kinetics and the formation mechanism." Soft Matter **8**(3): 726-733.
- Yang, X. N., J. Loos, et al. (2005). "Nanoscale morphology of high-performance polymer solar cells." Nano Letters **5**(4): 579-583.
- Yang, Z., I. Mochalkin, et al. (2000). "A model of fibrin formation based on crystal structures of fibrinogen and fibrin fragments complexed with synthetic peptides." Proceedings of the National Academy of Sciences of the United States of America **97**(26): 14156-14161.

- Yeromonahos, C., B. Polack, et al. (2010). "Nanostructure of the Fibrin Clot." Biophysical Journal **99**(7): 2018-2027.
- Yin, W. and M. Dadmun (2011). "A New Model for the Morphology of P3HT/PCBM Organic Photovoltaics from Small-Angle Neutron Scattering: Rivers and Streams." Acs Nano **5**(6): 4756-4768.
- Zhao, J., A. Swinnen, et al. (2009). "Phase Diagram of P3HT/PCBM Blends and Its Implication for the Stability of Morphology." Journal of Physical Chemistry B **113**(6): 1587-1591.

Appendix 1

Useful Tables for Scattering Experiments and Analysis

Table A1.1 Neutron scattering lengths and cross sections relevant to this research. Elements with very high absorption cross sections are useful for blocking neutrons and are highlighted with bold text. Scattering lengths are used with Equation 2.2 to calculate the scattering length density.¹

Element	Bound Coherent Scattering Length (fm)	Coherent Cross Section (barn)	Incoherent Cross Section (barn)	Absorption Cross Section (barn)
H	-3.7406	1.7583	80.27	0.3326
D	6.671	5.592	2.05	0.000519
B	5.30-0.213 <i>i</i>	3.54	1.7	767
C	6.646	5.551	0.001	0.0035
N	9.36	11.01	0.5	1.9
O	5.803	4.232	0.0008	0.0001
Na	3.63	1.66	1.62	0.53
Al	3.449	1.495	0.0082	0.231
Si	4.1491	2.163	0.004	0.171
S	2.847	1.0186	0.007	0.53
Cl	9.5770	11.5287	5.3	33.5
Ca	4.70	2.78	0.05	0.43
Ti	-3.438	1.485	2.87	6.09
Cd	4.87-0.70 <i>i</i>	3.04	3.46	2520
Gd	6.5-13.82 <i>i</i>	29.3	151	49700

1. Neutron News, Vol. 3, No. 3, 1992, pp. 29-37

Table A1. 2: Mass density and scattering length density table. Here MW (g/mol) is the molecular weight, ρ_m (g/mL) is the mass density, $\rho_{\text{SLD}}^{\text{N}}$ (\AA^{-2}) is the neutron scattering length density and $\rho_{\text{SLD}}^{\text{X}}$ (\AA^{-2}) is the x-ray scattering length density.

Fibrin Project Materials		MW (g/mol)	ρ_m (25°C) (g/mL)	$\rho_{\text{SLD}}^{\text{N}}$ (25°C) (\AA^{-2})	$\rho_{\text{SLD}}^{\text{X}}$ (25°C) (\AA^{-2})
Fibrinogen		~350,000	---	3.17E-06	---
Water	H ₂ O	18.015	0.997	-5.60E-07	9.46E-06
Deuterated Water	D ₂ O	20.0276	1.107	6.36E-06	9.41E-06
P3HT Project Materials		MW (g/mol)	ρ_m (25°C) (g/mL)	$\rho_{\text{SLD}}^{\text{N}}$ (25°C) (\AA^{-2})	$\rho_{\text{SLD}}^{\text{X}}$ (25°C) (\AA^{-2})
P3HT	[C ₁₀ H ₁₄ S] _n	---	1.1	6.76E-07	1.02E-05
Benzene	C ₆ H ₆	78.11	0.874	1.18E-06	7.99E-06
D6-Benzene	C ₆ D ₆	84.14	0.942†	5.37E-06	8.00E-06
Toluene	C ₇ H ₈	92.14	0.867	9.41E-07	8.00E-06
D8-Toluene	C ₇ D ₈	100.17	0.943†	5.66E-06	8.01E-06
p-Xylene	C ₈ H ₁₀	106.16	0.861	7.71E-07	8.00E-06
D10-p-Xylene	C ₈ D ₁₀	116.23	0.948†	5.89E-06	8.05E-06
† Equations to calculate density of deuterated solvent over the experimentally relevant temperature range.					
D6-Benzene	ρ_m (g/mL) = -1.2x10 ⁻³ T(°C)+0.9725				
D8-Toluene	ρ_m (g/mL) = -1.04x10 ⁻³ T(°C)+0.966				
D10-p-Xylene	ρ_m (g/mL) = -9.84x10 ⁻⁴ T(°C)+0.9637				

Appendix 2

Fibrin Sample Preparation Protocols

Purchasing and Product Storage Information

Human fibrinogen, depleted of plasminogen and von Willenbrand factor, is purchased from Enzyme Research Laboratories in South Bend, Indiana (Catalog no. Fib 2). The protein is sold in 1 g quantities, frozen in a 20 mM sodium citrate-HCl buffer at pH 7.4 at concentrations of ~40 mg/mL and is shipped overnight delivery on dry ice. Upon receipt the protein is stored in a -80 °C freezer until use. Additionally if experiments are carried out overseas the protein is lyophilized prior to shipping due to the extended shipping time and must be reconstituted with water upon arrival.

Fibrinogen Stock Preparation

Standard Preparation

The frozen fibrinogen solution is defrosted and then maintained at 37°C to maximize the protein stability. The protein is dialyzed against the a buffer solution to ensure that all samples have consistent composition regardless of protein concentration

and to eliminate the sodium citrate, which acts as a chelating agent and inhibits Factor XIII activation. Regenerated cellulose dialysis tubing with a 10 mm flat width (12,000-14,000 nominal MW) is used for dialysis. Each dialysis stage requires ~4 hr time to equilibrate.

Three buffers have been used in this research. The first buffer contains 0.5 M NaCl and 0.05 M tris in DI-H₂O and is titrated to pH 7.4. The second buffer, used in Chapters 3 and 4 contains 0.5 M NaCl and 0.05 M tris in D₂O and is titrated to pD 7.4. D₂O is purchased from Cambridge Isotope Laboratories in Andover, MA. The third buffer, used in Chapter 5 for the oxidized fibrinogen study, contains 0.14 M NaCl and 44 mM hepes in DI-H₂O and is titrated to pH 7.4. Titration curves for adjusting the pH or pD of the buffer solutions are plotted in Figure A2-1. The tris buffer pH and pD are adjusted by varying the molar ratio of tris-base and tris-HCl. The hepes buffer is titrated with the addition of NaOH.

After dialysis the fibrinogen solution is filtered through 0.45 μm PVDF syringe filters to remove any protein aggregates. If PVDF syringe filters are unavailable, an alternative material that minimizes protein adsorption can also be used (PTFE also works well). The concentration of the filtered protein solution is determined with UV-Vis spectroscopy using an extinction coefficient (ξ_{280}) of $1.6 \text{ mL}\cdot\text{mg}^{-1}\cdot\text{cm}^{-1}$. The samples are diluted with the buffer to the desired stock concentration, aliquoted into appropriate volumes and stored at $-80 \text{ }^\circ\text{C}$. After an aliquot has been defrosted unused fibrinogen should be discarded and not refrozen for future use.

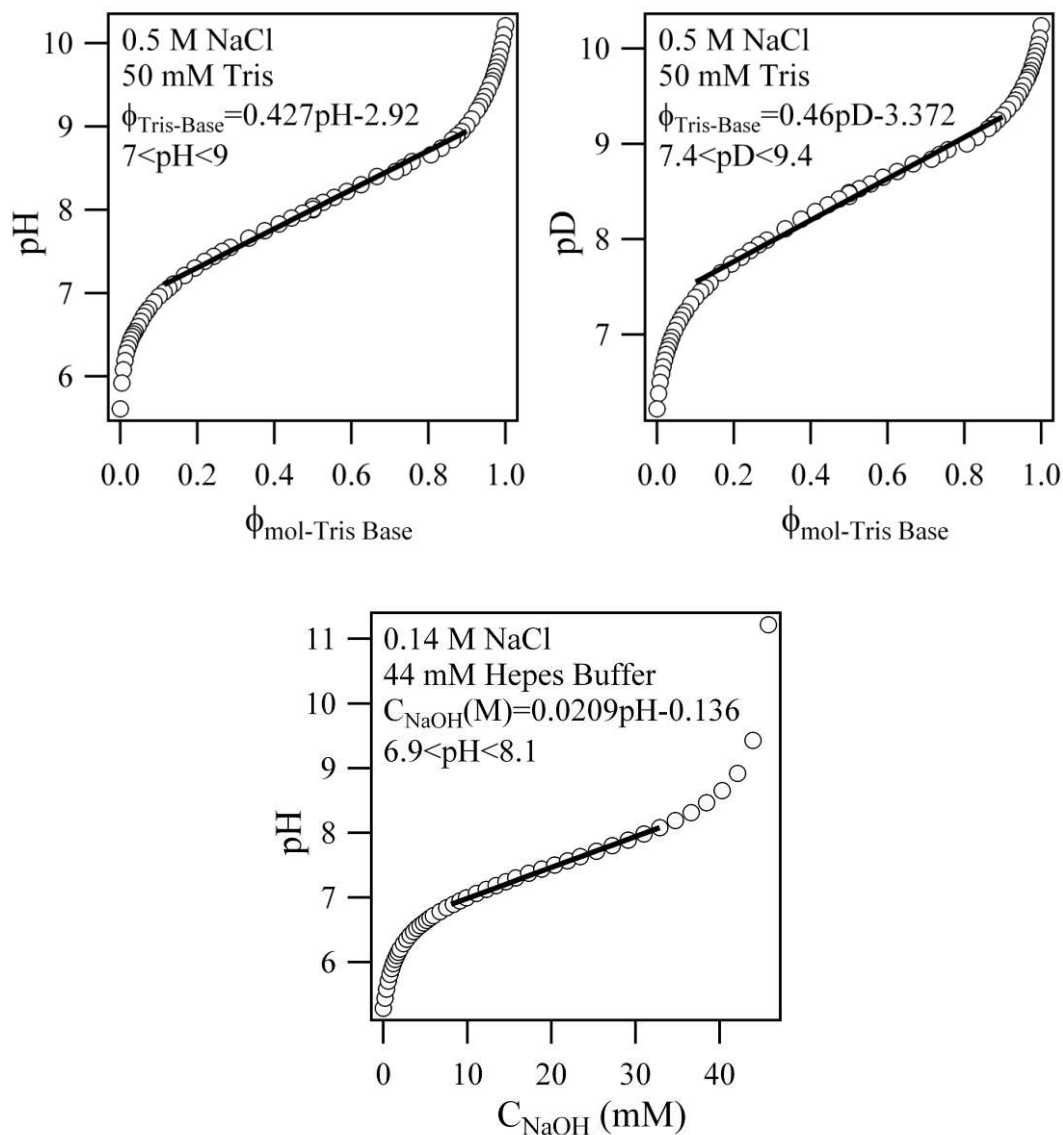


Figure A2.1: Titration curves for preparation of buffer solutions. The equation is from a linear fit over the defined pH or pD range.

Dialysis into D₂O

For neutron scattering experiments the buffer must contain >98% D₂O to ensure that a constant composition is maintained when diluting the protein to the various sample concentrations. This is necessary to maintain a constant solvent scattering length density across all samples. The buffer exchange is performed in three steps with at least 30 mL of D₂O for every 10 mL of protein solution. By performing the dialysis in three steps, the

total amount of D₂O required to reach a 98% exchange is reduce, which is necessary given the cost of the deuterated water. All other preparation steps are identical to those described in the standard protocol above.

Fibrinogen Oxidation

For experiments described in Chapter 5, the fibrinogen is oxidized with HOCl by the addition of a sodium hypochlorite solution. To oxidize the fibrinogen, 50 or 150 mol HOCl is added per gram fibrinogen and incubated at 37°C for 1 hour. The HOCl is taken from a 0.607 M stock solution. HOCl degrades slowly over time. Therefore, the concentration of of the NaOCl stock solution is verified using UV-Vis spectroscopy with an extinction coefficient (ξ_{292}) of 350 cm⁻¹ M⁻¹ at $\lambda=292$ nm. The fibrinogen aggregates and crashes out of solution if the NaOCl is added directly from the stock solution. It must be diluted ~100x before being added in order to prevent a locally high concentration gradient. To quench the oxidation reaction a 10× molar excess of methionine is added to the HOCl treated fibrinogen after one hour. A 0.303 M stock solution of methionine is prepared. This concentration of methionine is just below the solubility limit of methionine in water (0.322 M at 20°C). The oxidized solutions are aliquoted and stored in the -80°C freezer until use.

Thrombin Stock Preparation

Human- α -thrombin is purchased in 1000 NIH unit quantities from Enzyme Research Laboratories and is shipped as described for the fibrinogen. The thrombin is stored at -80°C until the first use. DI-H₂O is added to dilute the thrombin to 1 mL. Subsequently, 20 μ L aliquots are prepared and stored at -80°C.

Sample preparation

Unless otherwise specified in the text all samples were prepared to a final concentration of 0.25-40 mg/mL fibrinogen, 0.16 NIH u/mL, 2.5 mM CaCl₂ in one the standard buffers. This thrombin concentration is lower than expected under physiological conditions, however, it is necessary to slow the gelation in order to allow adequate time for sample loading.

The fibrinogen and thrombin aliquots are warmed to 37°C. The thrombin aliquot is diluted to 1 mL yielding a 20 NIH U/mL concentration thrombin solution. At this concentration protein adsorption onto the vial is negligible relative to the total concentration. However, additional dilution prior to sample loading may lead to irreproducible protein concentration. The fibrinogen is filtered with the 0.45 µm syringe filter and the concentration is verified with UV-Vis spectroscopy as described above. Calcium chloride should be added just prior to gelation, especially for high concentration samples in D₂O, as the addition of calcium has occasionally promoted spontaneous gelation, even in the absence of thrombin.

Neutron Scattering

Samples prepared for neutron scattering, and in particular USANS, must be degassed to remove any small air bubbles that can cause scattering artifacts at low- q . The fibrinogen and thrombin solutions are degassed under moderate vacuum (-30 mmHg) at 37°C for 40 minutes prior to mixing. Standard neutron scattering experiments are performed in demountable cells with quartz windows and a 4 mm pathlength. The CaCl₂ and degassed thrombin is added to the fibrinogen, mixed with gentle pipetting or swirling

and then loaded into the cells. Approximately 2 mL sample is necessary for the 4 mm pathlength cell. For rheoSANS and 1-2 plane shear SANS, the samples are prepared in the same manner except that larger sample volumes (~5-15 mL) are required.

SAXS

Small angle x-ray scattering is used to characterize the structure of the fibrin fibers in the oxidized fibrinogen study. Only ~100 μ L of solution is necessary to fill the glass capillary sample holders. Further dilution of thrombin and fibrinogen is necessary to accurately prepare such small volumes. To prevent appreciable protein adsorption of the stock solutions onto the plastic vials, the vials are soaked with a more concentrated protein solution and then lightly rinsed before the actual stock solution is added to the vial. The fibrin and fibrinogen is mixed and 50 μ L is added to the glass capillary. The small end of the capillary is sealed with heat over a Bunsen burner. The large end of the capillary is filled with a quick cure epoxy. A small amount of epoxy is also applied to the heat sealed end to ensure that a full seal is attained. The samples are allowed to gel, and the epoxy is cured for a minimum of two hours. The capillaries are tested for vacuum seal in a vacuum dessicator or a vacuum oven prior to being loaded into the SAXSess.

Curriculum Vitae
Kathleen M. Weigandt, PhD

Education

<i>University of Washington, Seattle, WA</i>	
PhD in Chemical Engineering	2012
Dissertation: Structure-Function Relationships of Self-Assembled Fibrillar Gels	
Advisor: Professor Danilo Pozzo	
MS in Chemical Engineering	2009
<i>University of Idaho, Moscow, ID</i>	
MS in Chemical Engineering	2007
Thesis: Preliminary Study of Microflow Potentiometry with a Silica Nanospring Electrode	
Advisor: Prof. D. Eric Aston	
<i>Oregon State University, Corvallis, OR</i>	2005
HBS in Chemical Engineering	

Professional Experience

University of Washington, Department of Chemical Engineering, Seattle, WA

Graduate Research

- Characterized the bulk structure and rheology of fully hydrated fibrin gels
- Corroborated well known models for strain hardening in fibrin gels by direct structural characterization under strain
- Developed relationships between structural and mechanical properties of conjugated polymer and small molecule organogels
- Mentored six undergraduate students on independent research projects

Teaching Assistant

- Classes: Interfacial Science and Colloids Laboratory and Graduate Transport
- Substitute lecturer on eight occasions
- Developed and implemented laboratory modules
- Evaluated homework, laboratory reports, and oral presentations

University of Idaho, Department of Chemical Engineering, Moscow, ID

Graduate Research

- Part of an interdisciplinary team that developed microfluidic sensors using silica nanosprings
- Developed protocol for assembling the microfluidic devices
- Characterized the flow field and made preliminary potentiometric measurements

Teaching Assistant

- Class: Separations
- Evaluated student assignments

Dimera Incorporated Internship

- Carried out experiments related to the molecular biology of cells obtained from arterial endothelial cells from primate hearts.

Graphic Packaging International Internship

- Worked with operators, lab technicians and engineers to create a new specifications database for the technical department to facilitate online access and increase efficiency.

Hewlett Packard Internship

- Designed, carried out, and analyzed experiments as part of a team effort to solve quality issues associated with a potential new product.

Awards and Honors

International Rotation IGERT Fellowship from UW Center for Nanotechnology (UW)
UIF Graduate Research Fellowship (UW)
Presidential Scholarship (OSU)
AEA Technology Scholarship (OSU)

Publications and Presentations

Journal Articles, refereed

1. Newbloom, G.M.*, **K.M. Weigandt***, and D.C. Pozzo. Electrical, Mechanical and Structural Characterization of Self-Assembly in Poly(3-hexylthiophene) Organogel Networks. *Macromolecules* **45** (8): 3452–3462 (2012)
2. **Weigandt, K.M.**, L. Porcar and D.C. Pozzo. *In situ* neutron scattering study of structural transitions in fibrin networks under shear deformation. *Soft Matter* **7** (21): 9992-10000 (2011)
3. Richards, J.J., **K.M. Weigandt**, and D.C. Pozzo. Aqueous dispersions of colloidal poly(3-hexylthiophene) gel particles with high internal porosity. *Journal of Colloid and Interface Science*. **364** (2): 341-350 (2011)
4. **Weigandt, K.M.**, L. Porcar and D.C. Pozzo. Structure of high density fibrin networks probed with neutron scattering and rheology. *Soft Matter*, **5** (21): 4321-4330 (2009)

Manuscripts in Preparation

5. Newbloom, G.M.*, **K.M. Weigandt***, and D.C. Pozzo. Structure and Property Development of Poly(3-hexylthiophene) Organogels Probed with Combined Rheology, Conductivity and Small Angle Neutron Scattering (Submitted)
6. **Weigandt, K.M.**, N. White, D. Chung, E. Ellingson, Y. Wang, X. Fu, D.C. Pozzo. Alterations in Fibrin Clot Structure and Mechanics Attributed to Specific Oxidation of Methionine Residues in Fibrinogen (Submitted)
7. White, N., **K.M. Weigandt**, D.C. Pozzo, J. Newton, K. Ward, D. Chung. Dysfibrinogen and Traumatic Shock (in preparation)

Book Chapters

Weigandt, K. M. and D.C. Pozzo. Protein Gel Rheology. Editors: J.M. Ruso & A. Piñero. *Proteins in Solution*. (Submitted)

Presentations

1. **Weigandt, K.M.**, L. Porcar and D.C. Pozzo “Structural and rheological investigation of fully hydrated fibrin gels: An in-situ neutron scattering study of structural transitions under shear deformation” 2011, Society of Rheology Conference (Poster)
2. **Weigandt, K.M.** G. Newbloom and D.C. Pozzo “Structural and Rheological Characterization of Poly(3-hexylthiophene) Organogels” 2011, NORM (Presentation)
3. **Weigandt, K.M.**, L. Porcar and D.C. Pozzo “Structural and rheological characterization of fully hydrated fibrin” 2011, NORM, (Poster)
4. **Weigandt, K.M.**, L. Porcar and D.C. Pozzo “*In Situ* Structural and rheological investigation of fully hydrated fibrin gels formed in D₂O buffers” 2010, Neutron Scattering for the Study of Soft Matter Tutorial Session, American Conference on Neutron Scattering (Presentation)
5. **Weigandt, K.M.**, L. Porcar and D.C. Pozzo “Structure of high density fibrin networks probed with neutron scattering and rheology” 2009, UW Chemical Engineering Graduate Student Symposium (Presentation)
6. **Weigandt, K.M.**, L. Porcar and D.C. Pozzo “*In Situ* Structural and rheological investigation of fully hydrated fibrin gels formed in D₂O buffers” 2009, International Conference on Neutron Scattering (Presentation)